8-9-2019

Characterizing the effects of build interruptions on the microstructure and mechanical properties of powder bed fusion processed Al-Si-10Mg

Ryan Mitchell Stokes

Characterizing the effects of build interruptions on the microstructure and mechanical properties of powder bed fusion processed Al-Si-10Mg

By

Ryan Mitchell Stokes

A Master's Thesis
Submitted to the Faculty of
Mississippi State University
in Partial Fulfillment of the Requirements
for the Degree of Master of Science
in Mechanical Engineering
in the Department of Mechanical Engineering

Mississippi State, Mississippi

August 2019

Characterizing the effects of build interruptions on microstructure and mechanical properties of powder bed fusion processed Al-Si-10Mg

By

Ryan Mitchell Stokes

Approved:

_____

Matthew W. Priddy
(Major Professor)

_____

Linkan Bian
(Committee Member)

_____

Haley R. Doude
(Committee Member)

_____

Yucheng Liu
(Graduate Coordinator)

_____

Jason M. Keith
Dean
Bagley College of Engineering

Name: Ryan Mitchell Stokes

Date of Degree: August 9, 2019

Institution: Mississippi State University

Major Field: Mechanical Engineering

Major Professor: Matthew W. Priddy

Title of Study: Characterizing the effects of build interruptions on microstructure and mechanical properties of powder bed fusion processed Al-Si-10Mg

Pages in Study: 111

Candidate for Degree of Master of Science

This work seeks to characterize the impact of build interruptions to additively manufactured Al-Si-10-Mg produced by the powder bed fusion (PBF) process. Additive manufacturing represents a significant investment in overhead, machine, and material making an interruption to the process a potential waste of money and time. Interruptions in the form of power outages, lack of powdered feedstock, and/or shielding gas will cause the machine to operate in an unintended manner, potentially even stopping the build process. The process of manufacturing will influence the microstructure, which determine the material's properties and performance. An interrupted PBF process could exhibit unique microstructural features and reduced mechanical properties that distinguish the resulting material from a continuous PBF process. Experiments were performed to simulate a production interruption with varying time periods of interruption and air exposure. The zone of interruption was characterized using optical micrographs, EDS, and hardness measurements to determine any effects of the interruption.

DEDICATION

I would like to dedicate this work to my parents, John and Cathy Stokes for whom I owe much gratitude and love. They have supported and provided for my education my entire life, something I can never fully repay. Without them I would not be where I am today.

I would also like to thank my aunt and uncle, Butch and Mary Stokes for providing me with a place to stay during my time in Starkville. They have been extremely welcoming and encouraging during my time here at MSU.

ACKNOWLEDGEMENTS

Research was sponsored by the Army Research Laboratory and was accomplished under Cooperative Agreement Number W911NF-15-2-0025. The views and conclusions contained in this document are those of the authors and should not be interpreted as representing the official policies, either expressed or implied, of the Army Research Laboratory or the U.S. Government. The U.S. Government is authorized to reproduce and distribute reprints for Government purposes notwithstanding any copyright notation herein.

I would like to thank the Army Research Laboratory for the funding that allowed for the completion of this work. I would also like to thank the Center for Advanced Vehicular Systems for the use of the equipment on which the experiments and analysis were carried out.

I would like to thank Dr. Priddy, Dr. Bian, and Dr. Doude for offering me a GRA position to study additive manufacturing. This provided me with an opportunity to receive a graduate degree in mechanical engineering in a manner I had previously not thought possible. I am grateful for their guidance throughout my time at MSU.

I would like to thank Joseph Young and Courtney Morgan for their efforts in training me in the AM lab and helping answer all my questions. I would also like to thank Matt Dantin and Will Furr for their encouragement and friendship during my time at MSU.

TABLE OF CONTENTS

LIST OF TABLES

LIST OF FIGURES

CHAPTER I

INTRODUCTION

1.1 Introduction of Additive Manufacturing

Additive manufacturing (AM) is a term used to describe several layer-by-layer production methods that create three dimensional components [1][2]. AM processes are different from traditional manufacturing methods that remove material to create components. Instead, components can be built directly from computer aided design (CAD) files with no prior tooling necessary [3]. Components produced by AM have shown comparable mechanical properties to cast and wrought materials making AM a viable option for use in critical design applications [4]. Design flexibility, short production time, ability to construct complicated geometries, and limited material waste are what have made AM an appealing method of production [5]. These are of particular interest in the aerospace, defense, medical, and automotive sectors [6]. AM has been applied to a variety of materials such as plastic, ceramics, composites, and metals [7].

Metal AM has more similarities with welding than casting as both welding and AM have a moving heat source and formation of a fusion zone [8]. Metal AM production has seen huge growth in recent years with many manufacturers creating their own machines, each with unique features and implementation of the layer-by-layer construction method [9]. AM is an attractive alternative for high priced lightweight alloys like titanium and nickel alloys [10]. The ability to recycle powder combined with minimal material usage is an appeal of AM and particular interest for high priced alloys [11]. Two popular and proven AM technologies that utilize metal are

Direct Laser Deposition (DLD) and Powder Bed Fusion (PBF) [12]. These processes use powder metals as feedstock and a high energy laser source to melt material. CO_2 or Nd:YAG lasers are common choices for use in these machines [13]. Both lasers are continuous wavelength (CW) which ensure uniform power delivery during emission. Both lasers can operate in the infrared wavelength (Nd:YAG is always 1064 nm) however, the Nd:YAG can emit higher powers than the CO_2 laser since it can be operated in a Q-switched (pulsed) or CW mode [14][15]. The Nd:YAG laser operates using a doped neodymiunm-doped yttrium aluminum garnet crystal to achieve lasing emission, while the CO_2 laser utilizes carbon dioxide gas.

DLD utilizes a blown powder approach, injecting powder into the laser beam path. Blowing the powder into the laser can allow for off axis, angled, (combination of x-y-z) powder application, making the ability to repair parts a unique feature to the DLD process [16]. Most other AM metal machines are limited to strict x-y-z movement. The blown powder approach can also take advantage of different metals simultaneously to create functionally graded materials, something that has not yet been accomplished in other metal AM machines. Functionally graded materials are also difficult to produce with traditional methods [17] [18]. In a Laser Engineered Net Shaping (LENS) DLD machine, the build platform moves in the x-y axis, while the laser beam is actuated in the z axis by movement of the focal lens. DLD does have some disadvantages such as greater material vaporization as well as morphology changes that can occur since all powder used must pass near the energy source [19]. Recyclability of powder can become an issue with morphology changes [20]. DLD also uses a long hollow column to house the focal lens for the laser as well as the powder dispenser. This column protrudes into the build chamber, which can cause issues as it is wide enough to run into other components already built

on the substrate. The bulkiness can make it difficult to fit a large number and variety of components on the substrate.

PBF machines use fine layers of powder spread upon a substrate to accomplish construction [21]. After melting specific portions of powder, the build platform is adjusted downward one-layer height, and the next powder layer is spread, by a wiper blade, onto the previously deposited ones. This process repeats until the component has been built. PBF offers the greatest geometric flexibility compared to other AM processes relying on part specific supports and surrounding powder to aid in construction of difficult overhangs [8]. PBF can also produce very wall structures due to the small laser spot size making it an excellent choice to produce lattice structures. Compared to DLD, there is no powder feed device that hangs in the build chamber making it much easier to fit multiple components onto the build substrate. PBF cannot accomplish functionally graded material or allow for repair like DLD. However, PBF offers the best CAD to completion of any metal AM process [22]. All AM processes typically require post treatment to obtain the best mechanical properties. This can include stress relief heat treatments, hot isostatic pressing (HIP), as well as machining [23] [24].

While AM offers advantages over traditional manufacturing methods, there are still some issues that must be resolved before widespread adoption by industries. This includes internal defects, complicated thermal stresses induced by: thermal gradients, rapid solidification, and subsequent reheating inherent in the layer-by-layer nature of AM[22] [25] [26]. Future work is needed to fix these remaining issues to allow AM greater adoption in industries.

1.1.1 Process Parameters and Microstructure

Process parameters are developed by the machine manufactures for specific materials to ensure adequate melting occurs. Researchers have conducted experiments to examine the effect different process parameters have on final component quality such as density [29]. Buchbinder et al. examined the effect of laser scan power and scan speed to look at density of aluminum in the PBF process [30]. The number of process parameters and their combinations allow AM flexibility in processing a variety of materials but can also make it difficult to identify suitable parameters [31]. The combination of laser power (P) and scan speed (v) determines the energy density (η) which is given by equation 1.1 [32].

$$\eta = \frac{P}{v}; \qquad \text{Equation 1.1}$$

The energy density and laser spot size influence the melt pool that travels along in the direction of the laser scan. The melt pool can be broken into three separate regions: the depression, transition, and tail end creating a heat affected zone in the wake of the track [33]. The melted material freezes at a very fast cooling rate, on the order of, 10^5- 10^6 K/s, leaving an observable solidification track [34]. The Renishaw PBF machine used in this study employs a scan strategy comprised of a hatch in-fill and border for each layer. These scan strategies overlap several solidification tracks to optimize material fusion and density. Scan strategies are selected by the user, optimized and applied by the software based on the specific layer's geometries.

Table 1.1 Common process parameters in AM.

Parameter	Value	Unit
Laser Power (P)	350 [27]	Watts (W)
Scan Speed (v)	2000	mm/s
Layer Height	30 [28]	µm
Hatch Spacing	0.08	mm
Scan Strategy	Stripe*	
Hatch Rotation	67	degrees

This table contains some example process parameters that are used in AM processes. The parameter denoted with an asterisk is specific to the machine used in this experiment.

The HAZ is quantified by two variables: the thermal gradient (G) and the solidification rate (R) [16] . The depth and shape of the melt pool will determine the magnitudes for G and R which affects the microstructure formation [35]. Viscosity of the melt influences the melt pool which affect the thermal gradients. Viscosity is dependent on the energy density with increased densities producing lower viscosity molten metal which spreads out better and improves bonding [35]. The thermal gradient and average temperature in the HAZ can be controlled by adjusting the width of the melt pool [18].

G and R can be calculated using two equations given in equations 1.2 and 1.3, respectively [19][36]. Equation 1.2 is the gradient of the temperature in the HAZ where T is the temperature while G represents the gradient. Equation 1.3 represents the solidification rate represented by R and given by one over the thermal gradient and the solidification cooling rate, derivative of temperature over time.

$$G = |\nabla T|; \qquad \text{Equation 1.2}$$

$$R = \frac{1}{G}\frac{\partial T}{\partial t}; \qquad \text{Equation 1.3}$$

A study conducted by Bontha et al. with Ti6Al4V predicted the formation of columnar, equiaxed, or mixed grains by plotting G vs. R on a solidification map. By tailoring the laser power, the effect on solidification rate and thermal gradient can be realized allowing for the possibility for microstructure to be altered during deposition simply by adjusting the laser power [36]. Using 2-D Rosenthal simulations Bontha et al. showed that increasing laser power with constant scan speed shifted the predicted microstructure from fully columnar down towards the mixed region of the solidification map [36] [37] . This calculated trend kept with observations seen by Wu et al [38]. Bontha et al. repeated this experiment for a constant laser power with increasing laser scan speeds and the same result was achieved. An increase in energy density, either increasing power or decreasing scan speed, showed a trend in shifting from columnar grains to mixed equiaxed grains [36]. A similar study was done on powder bed fusion AlSi10Mg and found increasing laser power vs. a constant scan speed, slightly increased the cooling rate. When the power was held constant and the scan speed increased, the cooling rate increased significantly [39]. This keeps with the results found in the study by Bontha et al.

Rapid cooling in AM, 10^5- 10^6 K/s, produces characteristic microstructural features. Sizes of grains, lamellae, or second phase particles decrease under these rapid cooling condition differing from cast microstructures [40]. These high cooling rates at the edge of the melt pool result in fine microstructures due to the rapid solidification of the melt to solid [41][42]. The cooling rate can be influenced by several conditions such as better thermal conduction from previous layers as well as convection [18]. The thermal history of components is governed by process parameters which control the melt pool characteristics, HAZ, microstructure, residual stresses and porosity [12].

1.1.2 Powder

The quality of any feedstock will largely dictate the performance of the finished part. The manufacturing process cannot be fully realized if sub-par material is used. AM processes rely on powdered metal for construction of components, and it is critical to select powder consistent in morphology, chemistry, and microstructure [43]. Powder used in AM is typically on the order of microns in diameter and can be made from several metal alloys like stainless steel, titanium, and aluminum [34] [44]. The methods of powder production can vary, with each process providing various quality powder at different price points. Plasma atomized, gas atomized, plasma rotating electrode process (PREP) are just a few methods of powder production [45].

Smaller powder results in a finer surface finish, which also implies a smaller build layer. For PBF, spherical powder with size distribution of 15-45 microns has been reported to provide the better ultimate strength and better surface finish [46]. A distribution of size ranges can improve packing density minimizing the presence of gaps between powder [47]. Spherical powder with limited satellites (surface anomalies) exhibits lower interparticle friction as well as increased particle mobility making it easier to spread with the wiper blade [43]. Reuse of powder can change the aspect ratio of the powder causing degraded mechanical properties [20]. The small size distribution allows for increased packing density as well as ensuring the incident laser beam hits multiple powder particles [28]. For example, if a powder particle is 150 microns in diameter a laser beam spot size of 70 microns could potentially only be incident on one single powder particle. Smaller particles ensure appropriate fusion occurs as the beam can be incident on more than one powder particle at a time.

Powder morphology refers to the powders; size, shape, and surface roughness which impact flowability and spread-ability [43]. Sieving, microscopy, and laser diffraction are three

methods that are used to determine the powder morphology. Sieving is a quick and efficient way to measure powder size but does not give any information on powder shape. Microscopy can provide details about the size and shape but can be dependent on what type of imaging system is used [43].

Powder chemistry is the elemental composition of the powder and cannot be determined from surface chemistry as the surface and bulk are rarely the same [43]. An oxide layer on the surface of the powder particle would yield a different chemistry than the bulk if just the surface was analyzed. X-ray photoelectron spectroscopy provides a surface element analysis useful in determining oxide states of powders. Electron Dispersive X-ray spectroscopy can provide internal chemical composition of powders if they are mounted and polished. Picking the appropriate characterization technique to determine bulk chemistry will impact the results [48]. Current material alloys have been developed for existing manufacturing processes making some less than ideal for use in AM. This shows the need for new chemistry development suited for AM as a gap in literature.

Powder microstructure describes grain sizes, phases, and the grain boundaries of the powder. The microstructure of the powder will determine the mechanical properties of as built components [43]. Porosity influences the crystal structure which is often studied alongside microstructure. Porosity is often attributed to process parameters, but porosity can exist in powder before it is even used. Traditional characterization techniques can be used but adjustments have been made given the small size and morphology of AM powder [49]. X-ray diffraction is a technique used to identify crystal structure by measuring the intensity of the constructive interference that occurs. The d-spacing of crystal can be determined and this value is unique for all seven crystallographic systems [43] [50]. It was noted in one study that powder

manufacture had an impact on the final phases of the powder. Gas atomized 17-4PH powder was compared between nitrogen and argon produce powder and different phases were found for each one. The nitrogen produced powder contained primarily austenitic microstructure while the argon powder contained mostly martensite [51]. Future work focused on the development of unique aluminum alloys suited for AM is underway [52]. This research coupled with knowledge gained from the implementation of AM process parameters could provide a boost to the AM community and see added benefit to the industry.

1.1.3 Porosity

Porosity is the lack of material in a given volume and is induced by the process of additive manufacture. This is commonly referred to as a void and can take many different forms in AM such as interlayer and intralayer porosity. Interlayer porosity occurs across several deposited layers and is attributed to lack of fusion or inclusions such as oxides [53]. Intralayer porosity is characterized by spherical voids typically produced from entrapped gases [54]. Voids in a material are typically detrimental as they reduce density and can cause stress concentrations which reduce fatigue performance [55] . Lower density is associated with lower mechanical properties due to increased likelihood of failure as these internal defects can grow and coalesce to from larger voids. Porosity is a common defect observed in AM affecting nearly every material. Aluminum is affected since this material forms aluminum oxide, Al_2O_3, easily creating internal inclusions [56].

Interlayer porosity can be characterized by elongated irregular shaped pores. These pores typically occur along solidification tracks and represent a lack of fusion (LOF) that occurred between build layers [8] [57]. LOF pores can reduce ductility of components when loaded in tension parallel with build direction [58]. Typically, HIP treatments can help to reduce porosity

especially LOF ones [23]. Increased pressure combined with elevated temperatures contributes to increased material density and decreased porosity. LOF pores can be a result of improper hatch overlap where gaps between solidification tracks can exist. Most LOF observed will contain unmelted powder particles in them indicating no melting occurred in that region. LOF pores are a main cause of anisotropic yield strength in AM [59].

Intralayer porosity is defined by spherical voids that occur within a single deposited layer [60]. There are a few causes of spherical pores such as: vacancies from packing limitations of spherical powder, coalescence of gaseous pores in powder particles formed from production, gas entrapment from melt pool turbulence and entrainment, vaporization of material in the melt pool. Voids can also be filled with trapped gases that originate from the inert gases used in AM machines to maintain a proper build environment. These gases might not have time to escape from the rapid solidification of the molten material [61]. These pores typically involve trapped gases such as hydrogen, which can be introduced into the material via moisture. The most common cause of intralayer porosity is the improper packing of powder particles. There is a maximum closed packed density of spheres with identical diameters at 64% making gaps in powder unavoidable [47]. This can be combated by selecting powder with a varying size range to introduce powder particles with different diameters improving packing density.

1.2 Aluminum

Aluminum (99.99%) is produced by the Hoopes electrolytic process and first became available in 1920 [62] [63]. Aluminum production is divided into two markets, primary and secondary, where the primary is made from fresh ore and the secondary is made from recycled aluminum. The processing of the material for the secondary market only takes 5% of the energy

required for the primary processing [56]. Pure aluminum crystalizes in the face-centered cubic lattice and is stable from 4 Kelvin (K) to the melting point at 933.5 K. Pure aluminum is very weak and soft which is a reason aluminum alloys enjoy much more usage over pure aluminum [56].

Aluminum is very stable in oxidizing environments due to the continuous aluminum oxide that rapidly grows on the surface when exposed to water, oxygen or other corrosives. At room temperature and 100% humidity, the oxide film will grow twice as fast as in dry oxygen [62]. The limiting thickness of the aluminum oxide layer is approximately 2.5 to 3.0 nm. Molten aluminum reacts with hydrogen, carbon monoxide, carbon dioxide, as well as water vapor with hydrogen being very soluble in both solid and molten aluminum. Casting aluminum alloys is difficult due to surface oxides that can become entrained as well as hydrogen gas in the melt which can inflate bi-films to become porosity [56].

The equilibrium solubility of oxygen in aluminum is very small, less than one atom in approximately 10^{35} or 10^{40} atoms. Oxides in the aluminum melt do not precipitate by reaction from oxygen, making their formation not from chemistry, but from mechanical entrainment [56]. Entrainment is when the molten liquid folds in on itself and captures the oxide film on the surface of the melt within the material. In both casting and in AM, this entrainment effect can become an issue [56]. Due to the layer by layer nature of AM, any oxides formed can become entrained when the next layer of material is deposited.

Aluminum alloys are selected due to their good wear and corrosion resistance, low thermal expansion, and high strength [42] [62]. Aluminum-silicon alloys are the mainstream casting alloys for engineering applications. Al-Si is a binary system that forms simple eutectics at 580°C at 12.6 wt%. A eutectic alloy has melting and solidification points of the constituents

lower than the individual elements melting and solidification points [62]. Al-Si exhibits good weldability compared to other aluminum alloys due to its near eutectic composition of Al and Si. Alloys also exhibit a high fluidity as well as low shrinkage in casting-welding applications [64]. These two phenomena are what make this alloy suitable for the AM process, as low shrinkage means the material will not crack upon solidifying. Additions of Mg or Cu are common as they both form precipitates, Mg_2Si and $CuAl_2$, that harden the material.

Aluminum alloy AlSi10Mg (AA No. 360) is an aluminum alloy consisting of approximately 10% silicon and < 0.5% magnesium (weight%). Magnesium silicide, Mg_2Si, age hardens the alloy through the formation of metastable phases called Guinier-Preston zones, which provide additional obstructions to dislocations from enriched solute regions [65]. Solute clusters precede the formation of the Guinier-Preston and have a defining role on the kinetics of the precipitation process [66]. The interaction between solute clusters and dislocations has a hardening effect different from precipitation hardening [66]. The equilibrium phase of Mg_2Si precipitates are denoted as the beta (β) phase [66]. Magnesium makes the Al-Si binary system heat treatable, increasing strength without affecting corrosion resistance [62]. Magnesium also influences the microstructure particularly the morphology of silicon phases, brittle phases and can reduce fracture toughness in large Mg percentages [67]. Mg has an influence on the eutectic Si particles. In wt% below 0.5%, the only solidification reaction involving Mg-phases discernable on the cooling curve is the ternary eutectic forming Al-Si and Mg_2Si [67]. In addition to reducing fracture toughness, excessive magnesium over the amount required to form the precipitate will reduce the solid solubility of the compound. The presence of hard metallic Si particles gives the Al-Si alloy the character of an in-situ metal matrix composite (MMC) [56]. AlSi10Mg performs well in AM due to the Si content which is close to the eutectic composition

at 12.5% which reduces solidification cracking [52]. This solidification cracking is less likely due to the small solidification range at 30 °C.

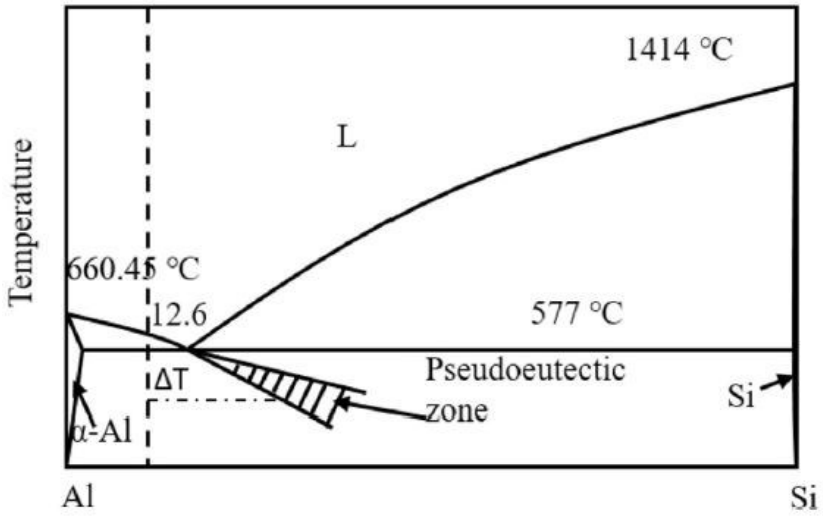

Figure 1.1 Phase diagram of Al-Si alloy.

Phase diagram of Al-Si alloy showing the pseudo-eutectic zone [68].

1.3 AM of Aluminum Alloys

Aluminum alloys have been investigated in several AM studies [9] [30][55]. These research projects have explored some novel methods of printing with aluminum such as the effect of high laser power on selective laser melting (SLM) of aluminum and droplet deposition of aluminum [9] [55]. Other research efforts have looked at AlSi10Mg investigating porosity reduction using process parameters, the formation of porosity and oxides as well as fatigue performance compared to traditional casting alloys [29] [69]. The mechanical properties of AM produced AlSi10Mg have been reported to perform similarly to cast samples of the same

material [30] [68] [70]. Tang et al. state the fatigue life of AM produced AlSi10Mg was similar to other AM studies of the same alloy but also discovered the internal defects were associated with large micron sized oxides likely formed from oxidation of vaporizing metal [55]. Pei et al. investigated the microstructure and solidification of AlSi10Mg finding the porosity of the material was affected by the hatch spacing [42]. They reported a fine microstructure consisting of supersaturated Al with Si-rich cellular boundaries [42]. Liu et al. reported a very similar microstructure observed as well [68].

Yu et al. investigated the effect of T6 heat treatments on AM AlSi10Mg finding the heat treatment had no effect on densification but did reduce hardness by 20% and spheroidized oxidation regions forming a dimple structure [71]. T6 heat treatment is a two part method of heat treatments for aluminum alloys consisting of a solid solution treatment at elevated temperatures for a limited period of time followed by an artificial aging at reduced temperatures for a longer period of time [62][71]. Aluminum alloys mechanical properties can be by combination of heat treatments, artificial aging, and cold working [62].

Most of the literature on AM production of aluminum mentions the formation of oxides similar to cast aluminum alloys [42] [55] [72]. Louvis et al. mention that it is unlikely to avoid oxide film formation and to utilize the SLM process to break up these oxides [72]. Oxide films are easily evaporated on the surface of the melt but oxides that are contained in the metal present more of a challenge. Marangoni convection forces help to break up other oxides in the bottom of the melt track but not oxides on the sides of the melt [72] [73]. This cannot be avoided as oxides will form on aluminum with even the smallest amount of oxygen present. Buchbinder et al. investigated the use of high laser powers to break up oxide formation finding success in using elevated laser powers to disrupt formed oxide films [30]. The formation of oxides and porosity in

PBF of aluminum present the two biggest issues with the manufacture of this material. Many researchers suggest drying powder before use to eliminate any moisture that might be present to reduce the possibility of moisture contributing to porosity [69]. Aversa et al. has investigated the development of new aluminum alloys that are specifically designed for PBF processes [52]. Rare earth and transition metals added to Al-Mg alloys, particularly scandium and zirconium have increased the performance by the formation of precipitates. Transition metals are can be cheaper to obtain and process making them a preferred candidate given their improvement to mechanical properties [52].

1.4 Motivation

There is a gap in the literature investigating the effects of process interruptions to the PBF process. This is of relevant concern as PBF processes continue to see more main stream integration into industries. Process interruptions to the PBF process could come in the form of power outages, lack of powdered feedstock, lack of inert gases, etc. AM represents an investment in machine, material, and operating costs making unwanted interruptions costly and potentially detrimental to component quality. If there is the potential to salvage an interrupted build, while still maintaining adequate mechanical properties, this would be of great interest to manufactures. The motivation of this work comes from an unpublished research paper investigating the effects of process interruptions to PBF AlSi10Mg [74]. This research group observed reduced mechanical properties and localized failure near the process interruption plane. This unpublished work is the only literature currently available that presents findings and discusses observations to the interrupted PBF process. Material scientist have established a relationship between process, structure, properties, and performance that discusses how each the process of material formation

influences the structure which directly determines the properties of the material and the subsequent performance of that material. AM processes produce components with refined microstructures due to the high cooling rates, which allow them to have increased mechanical properties. An interrupted PBF process could exhibit a modified microstructure from an uninterrupted PBF process given one is interrupted and the other is continuous.

1.5 Research Objective

The goal of this work is to further investigate the effect of build interruptions on microstructure and mechanical properties of PBF produced AlSi10Mg. Previous work exploring this topic identified reduced mechanical properties and localized failures corresponding to the interruption location. To investigate the proposed phenomenon, three separate timed interruptions were created, with and without air exposure, to observe what effect different interruptions have on finished properties. The previous work that investigated process interruptions only conducted one interruption. This work expands on that by conducting seven builds, six interrupted and one control build.

These interruption periods are: five minutes, complete cool (12 hours), and 24 hours. Each of these interruption periods was repeated to investigate the effects of air exposure and no air exposure during the interruption. The hypothesis for this investigation is that specimens produced in an interrupted build process will exhibit reduced mechanical properties and localized failure vs. uninterrupted specimens. The plan for determining the effect of interruptions is outlined in the next chapter. X-ray Ct data, micrographs, Vickers microhardness, and tensile data was collected to data related to porosity, microstructure, and mechanical properties of the specimens.

CHAPTER II

EXPERIMENTAL PROCEDURES AND ANALYSIS METHODS

2.1 Machine and Material

The PBF machine used was a Renishaw AM400. This machine employs a 400W, 1065nm wavelength Nd:YAG laser with a 70-micron focal spot size and is based on a vacuum casting machine which allows for improved build environment control. The vacuum is used to reduce the amount of argon gas required to sufficiently purge the build chamber to appropriate oxygen levels [75]. Process parameters for the machine were held constant for each experiment and are given in the Table 2.1. These parameters developed by Renishaw are standard parameters for AlSi10Mg.

Table 2.1 Process parameters used in this investigation.

Parameters	Value	Unit
Laser Power (P)	275	Watts (W)
Scan Speed (v)	2000	mm/s
Layer Height	30	µm
Scan Strategy	Stripe	
Hatch Rotation	67°	degrees
Preheated Platform	170°	Celsius

Process parameters were held constant for all experiment groups.

AlSi10Mg plasma atomized powder was obtain from LPW Technology. This powder is spherical in nature and has a size distribution of 15-45 microns. The elemental breakdown of the

powder supplied is given in the Table 2.2. The powder was not dried before each use. This powder was reused with each experiment for a total of seven uses.

Table 2.2 Aluminum silicon magnesium powder composition.

Symbol	Element	Result (wt%)
Al	Aluminum	BAL
Si	Silicon	9.90
Mg	Magnesium	0.35
Fe	Iron	0.11
O	Oxygen	0.04

Material data sheet provided by LPW powder showing the elemental composition of the powder. There are trace elements of iron, the most common impurity in aluminum. This also shows the presence of oxygen in powder. Powder was between 15-45 microns in diameter.

2.2 Experimental Design

There were seven builds in total for this study, six interrupted builds with one control. The full experimental design with completion order is given in Table 2.3. Note the 5 min with air experiment was completed before the 5 min without air to account for the time required to purge the machine of the air present in the chamber. Approximately one hour was required to purge the machine and resume building. Three time periods were chosen as they represent likely interruption scenarios that could occur in a production environment.

Table 2.3 Experiment order and details

Experiment Number	Interruption Build	Air Exposure	Heater Turned Off
1	Control	No	No
2	Complete cool	No	Yes
3	24 hours	No	No
5	5 minutes	Yes	No
6	5 minutes	No	No
7	Complete cool	Yes	Yes
8	24 hours	Yes	No

Experiment number corresponds to order build was carried out. Air exposure and heater apply to conditions during the experiment.

The 5 minute interruption paused the build for 5 minutes for both air exposure and non-air exposure; however, as stated earlier, this interruption was approximately an hour as this was the time required to make the build chamber inert again. The complete cool interruption required turning off the heated elevator and letting it cool from 170°C to 40°C, taking approximately 12 hours to cool. The 24 hour interrupted build involved pausing the machining and leaving the heated build platform on. A 5-minute interruption could be the time required to refill the hopper with powder, make a small adjustment to the machine, or possibly re-inert the build

environment. The complete cool scenario simulates a power outage, as the heated build platform was turned off and the machine was left idle for hours. If the power were shut off and then turned back on, the machine will stop and require manual intervention. The 24-hour interruption could simulate a machine left to run over a weekend period that stopped from an error but continued to maintain the heater and build chamber settings.

Each experiment consisted of building 24 specimens in total, 12 tensile specimen and 12 cylindrical specimens from the AlSi10Mg powder. The dimensions for each specimen are given in Figure 2.4. The cylindrical specimens were machined after completion into the dimensions of the tensile specimens. The approximate location of interruption on the specimens is denoted by the blue line and is ~40 mm from the bottom of the specimens. The location was chosen to place the interruption plane in the gage section of specimens, while keeping it from being in the center of the gage section. This was done in an attempt to isolate the interruption break locations from typical tensile failures. The location of each specimen on the build plate is given in Figure 2.2.

Each build was prepared the same way with measurement and installation of the substrate, setting appropriate clearance of the wiper blade and checking the spread of powder to ensure an even distribution of powder over the substrate. The build platform was heated to 170 °C according to the Renishaw manual for AlSi10Mg. Each build was interrupted at the same layer number, layer 1500. This placed the interruption at ~40mm. This was calculated using the total number of layers, including the layers for supports, and the layer height, 30 microns. The total number of layers was 3166. The supports took 166 layers at a height of 5mm leaving 3000 layers for the specimen, for a height of 90 mm. Pausing at layer 1500 put the total build height at 45mm which accounts for the 5mm support height, making the height on the specimen at 40mm.

This location can be observed in Figure 2.3 with the blue horizontal line denoting the location of interruption.

The air exposure for the experiments was accomplished by replacing the argon tank with ultra-high purity air obtained from nexAir. The chamber door was not opened during the interruptions. This was done for safety, and the machine prevents the door from opening when the elevator is heated is above 70 °C. The compressed air chosen had very low moisture content to limit moisture in the machine and build environment. The compressed air contained approximately 20-22% oxygen as this is the level of oxygen in atmospheric air [76] . The machine was purged with the compressed air and the level of oxygen in the machine was monitored using the built-in oxygen sensors. One sensor monitors the levels in the top of the build chamber and the other sensor monitors the oxygen level at the bottom of the chamber. To gauge how much air needed to be allowed into the machine, readings were taken from the oxygen sensors when the machine was not active and when ample air was in the build chamber. Approximately 17% oxygen was measured in our unpurged system.

When restarting the machine for the complete cool and 24hr experiments it was necessary to adjust the elevator upwards. This was due to thermal contraction of the substrate and specimens during the interruption. Adjusting the elevator was necessary to ensure the powder spread was similar to previously deposited layer thicknesses. This took some time, mainly to prevent damage to the wiper blade and specimens. The elevator was adjusted in increments and the wiper blade was moved to spread powder over the specimens. This was repeated until there was a thin coat of powder over the specimens at which point the machine was restarted.

The layout of the specimens on the build plate is given in Figures 2.1, 2.2. Twenty four specimens were built in total and a letter/number scheme was adopted to differentiate where the

specimens were located on the substrate. This is given as: C1-12 and D1-12, with C representing the cylindrical specimens and D representing the dog bone specimens. The number represents the location within the group.

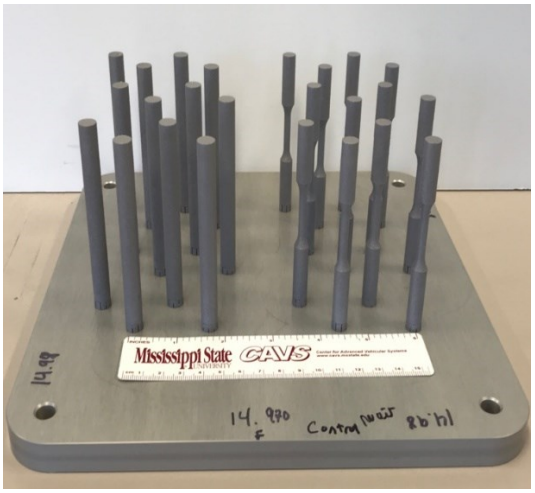

Figure 2.1 Completed control build showing layout of the specimens.

Control experiment on build plate showing the arrangement of specimens, the build plate is orientated as it would be in the machine. Wiper blade spread powder from the rear to the front of the plate.

Figure 2.2 Completed build with number scheme used.

Complete cool with air interrupted build displaying number scheme. Number order repeats in same manner for dog bone specimens on right side.

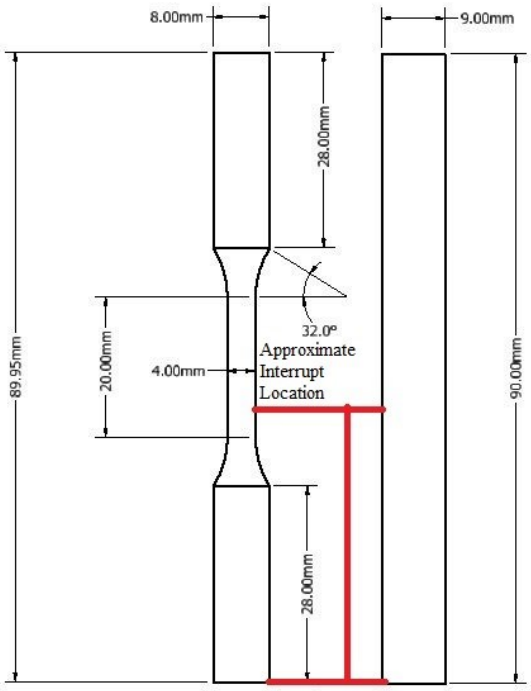

Figure 2.3 Drawings of the dimensions used for specimens given in mm.

Dog bone and cylinder dimensions that were built in the machine. The machining was done to match the cylinders to the dimensions of the as built. The red line denotes approximate location of interruption ~40 mm.

2.3 Experimental Methods

This section outlines the various methods and equipment analysis was conducted on. All analysis was conducted at the Center for Advanced Vehicular Systems at Mississippi State University, unless stated otherwise. Each method of analysis used has literature supporting the purpose of these methods chosen. Tests were carried out on selected samples, meaning not every sample underwent every test. This would be impossible as some characterization requires destruction of the samples. Characterization techniques are important since they help quantify specific aspects about the material and mechanical properties of the interrupted PBF process.

Data collection on several samples is crucial since this helps to confirm or disprove certain results that might be observed. For example, in tension tests, collecting one data point is insufficient, and the user must collect multiple data points per experimental group to calculate an appropriate average of mechanical properties as well as to identify variability in the data. Each experimental method is defined individually, with machine descriptions and settings given as well as explained. This is justified with literature supporting the analysis as well as the settings for each machine.

2.4 X-Ray CT/ Volume Graphics

X-ray computed tomography is a nondestructive method of imaging specimens that allows for examination of internal features and defects. This is a popular technique for AM components as it is nondestructive and can be a fast and efficient way to qualify components for service [77]. Since AM components are plagued by porosity, this method provides the best nondestructive way to quantify and observe internal defects. Hammond et al. utilized X-ray CT to observe internal porosity in their AM produce AlSi10Mg specimens [74]. Tradowsky et al. also used micro CT to examine internal defects and the effect of post processing on internal structure of AlSi10Mg [78].

The machine used was a Nikon XT H225 X-Ray. This machine utilizes a rotating target which emits X-xays from the source, extending outward in a cone from the source. The machine captures two images of the specimen per degree of rotation through the full 360°. These .tif images are then reconstructed by Nikon software to compile a 3D view comprised of voxels. A voxel is like a pixel but instead exist in a 3D environment. The voxel is what helps encode specific information regarding the material and the background. This reconstructed file is

manipulated with Volume Graphics software. This software allows for surface determinations to made of the material comparing the isometric values of the material and background to identify the presence of internal voids. An isometric value is a rating of brightness used to designate the levels of light and darkness. This program offers capabilities to quantify data captured through the X-ray scan. For this research two modules offered by Volume Graphics were utilized; the coordinate measurement module and the porosity module [79]. The coordinate measurement module establishes a coordinate system using selected surfaces of the object, necessary to establish the locations of defects. The porosity module uses an algorithm to determine the presence of voids based on material and background definitions. For this research project two samples per experimental group were scanned, cylinder specimen #8 and dog bone specimen #5. This allowed for a comparison to be made between experimental groups and from the two different geometries, cylindrical and dog bone.

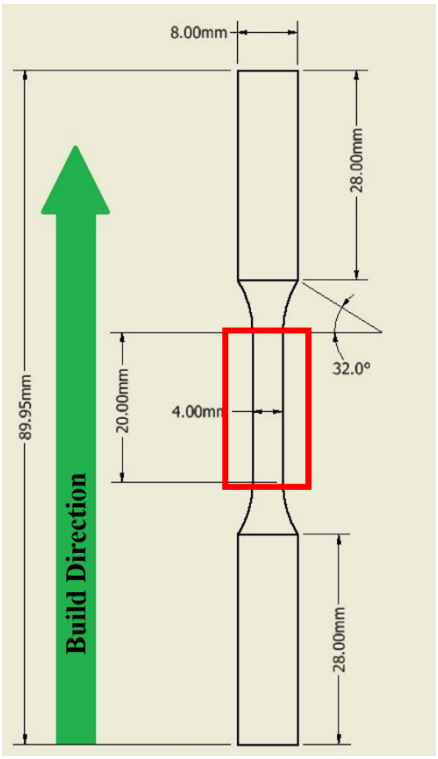

Figure 2.4 Location of cut metallographic samples.

Location of cut metallographic samples. The green arrow denotes the build direction. Samples were cut longitudinally to observe the interruption plane. The red box denotes location of cuts at approximately 35 mm and 55 mm.

2.5 Mounting, Polishing, Optical Microscope

The optical microscope is a powerful instrument that allows for visual observation, accomplished through magnification, of material surfaces. To characterize the internal solidification tracks, porosity, and microstructure it is necessary to cut and mount specimens. Optical microscopy is a common characterization technique for metallography since it is easily accessible. In addition to mounting and polishing it is sometimes necessary to etch the specimens for better observation of the metal. The microscope has a limited depth of field and resolution making it difficult to observe some features at higher magnification. The level of magnification is determined by the optics of the system. Yu et al. used optical microscopy to observe

solidification tracks and microstructure of T6 heat treated AlSi10Mg AM specimens [71]. Kobryn et al. used optical microscopy to characterize microstructure and texture of Ti-6Al-4V to different process parameters [37].

Two specimens were taken from each experimental group, cylinder #4 and dog bone #1. Specimens were cut using a Struers MiniTom diamond saw which allows for a small cut and minimal material removal. The specimens were taken from the gage section parallel to the build direction (longitudinal/z-axis) and as denoted in Figure 2.4. These cuts were made at the 35mm and 55mm mark on the specimens. This was done so that material above and below the plane of interruption could be observed. Specimens were cold mounted in epoxy resign from Struers and was done so that samples could be polished and still be observed within the clear mount. Specimens were mounted along the build of similar nature, i.e. 24 hour air and 24 hour cylinders were mounted together, while 24 hour air dog bone and 24 hour dog bones were mounted together. This was also done as the gage sections diameter for cylinder and dog bones was different. Specimens were polished on a Struers Tegra Pol-11 according to the recipe provided from Struers and this is given in the appendix. Each mount of samples was polished to half way, the full diameters, 8 mm and 4 mm for cylinders and dog bones respectively. Once polishing was completed samples were etched using Keller's reagent for 5-7 seconds total. Keller's reagent is a popular etchant for titanium and aluminum and has been used in several studies looking at microstructure of AlSi10Mg [68] [72][74] . The recipe for Keller's reagent is given in the appendix table A.2.

Once etching was completed optical microscope images were taken using a Zeiss Axiovert 200, which has up to 100x magnification, and offers several filters to help observe microstructural features. The filters on the microscope include polarized light, a dark field and

the DIC option allowing for light to be cast in certain direction onto the sample essentially making some features appear 3D. Optical microscope images make it easy to observe bulk material, defects and pores. Marks were made on the mount to denote the location of interruption to allow for quick observation of this area. Several photos were taken along the entire gage section at differing magnifications for each specimen.

2.6 Scanning Electron Microscope (SEM), Energy Dispersive Spectroscopy (EDS), Electron Backscatter Diffraction (EBSD)

Scanning electron microscopy (SEM) is a characterization technique that allows for detailed images to be taken at extremely high magnification. The SEM has a very large field of view making it possible to take high magnification images while continuing to keep the rest of the material in focus. This is extremely useful to allow multiple images to be taken showing the exact location of a defect or a fracture surface. Specimens are typically mounted, and sputter coated with a conductive material, like silver, as the SEM operates using electrons. This is even done if the material is conductive to improve the quality of the image. The SEM is widely utilized by researchers to examine microstructure, defects, and fracture surfaces. The SEM can also allow the use of other tools like energy dispersive spectroscopy or electron backscatter diffraction. Carter et al. utilized the SEM technique to observe the microstructure as well as the influence of scan strategy on PBF produced nickel superalloys [80]. Murr et al. used an SEM to examine Ti-6Al-4V microstructure manufactured by electron beam melting, another form of AM [81]. Hammond et al. used an SEM to characterize the fracture surface of the interrupted PBF AlSi10Mg [74].

A Zeiss Supra 40 was used to collect fracture surface images. This provided high resolution images of fracture surfaces allowing observation of features that help to determine the fracture origins or causes.

Energy dispersive spectroscopy (EDS) is a chemical analysis method that is used in conjunction with SEM equipment. Using the EDS with the SEM lets users select an area of interest to scan and create a spectral or elemental map of the sample. This is useful for determining what material is present in a specimen. EDS can be used on most materials making its application universal. Fousova et al. utilized EDS to examine the precipitates in AlSi10Mg at elevated temperatures showing that these precipitates were comprised of pure Si [82]. Jia et al. used EDS to determine the chemical composition of PBF Inconel 718 powder before usage [32]. EDS can be used to examine powder and is a way to confirm the material report typically supplied with the powder. EDS works by exciting electrons in the material through X-rays or electrons, measuring the energies given off by the ejected electron. Since these energies are elemental specific, the element can be determined from this [83].

An EDAX EDS was utilized to examine interrupted specimens for the presence of oxygen. Spectral scans and element maps were taken to examine bulk material as well as inclusions located near the interruption plane. Specimens were hot mounted and polished in the same fashion as the optical micrograph specimens. They were not etched to prevent interference with the chemical composition scans. The specimens scanned were cylinder #2 and dog bone #7. Cylinder #2 had been machined into the same dimensions as the dog-bone at this point.

Electron backscatter diffraction (EBSD) is a technique used to quantify microstructures by identifying crystal shapes, grain sizes, grain boundaries, grain misorientations and phases. Specimens must be mounted and turned at an angle of 70 degrees from the detector to

appropriate operate. Maps are created using Kikuchi bands which correspond to the diffraction patterns of different crystal lattices. This technique creates a color-coded map to identify the orientation of the grains according to Miller Indices [84] [85]. EBSD can help observe how various methods of manufacture and heat treatments can influence microstructure formation and or change the microstructure. Wang et al. used EBSD to examine the grain orientation and average size of 304L stainless steel made by AM direct energy deposition [86]. Yadroitsev et al. used EBSD to examine single solidification tracks of 316 stainless steel and the effect of energy input on morphology and microstructure [87]. Liu et al. ran EBSD scans on PBF AlSi10Mg to determine how various laser powers influenced the formation of microstructure [68].

The EBSD system used was an EDAX TSL. EBSD maps were taken from the interruption zone to determine if unique microstructure was created due to the interruption. EBSD scans of a control were done to establish microstructure of uninterrupted AlSi10Mg.

2.7 Vicker Microhardness

Vickers microhardness is an indent technique that uses a Vickers tip, a diamond shaped tip to indent on a material with a pre-determined load. The resulting indent is measured at the corners using an optical camera and a Vickers hardness value is established based on the size of the indent. The softer a material is the larger the indent and the harder a material is the smaller the indent. Vickers hardness is an alternative to Brinell hardness and does not require the size of the indenter to be known [88]. The Vickers hardness determined is also independent of the applied load so long as it is above 200gf. Vickers hardness is done on a mounted and polished sample several times to create an average hardness of the material. This method is useful as it can help establish a materials hardness which correlates to a material's tensile strength. A

Vickers test is a lot quicker to accomplish and doesn't require a tensile specimen making it a possible alternative to derive that mechanical property. However, in most cases this is just used to verify the tensile strength obtained in tension tests. Vickers hardness can also be done to examine the effect of heat treatments on hardness. Yadollahi et al. used Vickers hardness to compare the hardness of single built specimens to multi-built specimens, finding multi-built specimens had a higher Vickers hardness [89]. Hammond et al. took Vickers hardness measurements on the interrupted PBF AlSi10Mg finding a reduced hardness near the interruption plane. This was attributed to a difference in microstructure [74].

Specimens were hot mounted and polished in the same fashion as before and then indented on using a Leco Vickers microhardness tester LM-300AT using the 200gf load. This was done on specimens from each experiment group for the same identifiers: cylinder #2 and dog bone #7. Twenty one indents evenly spaced at .508mm (0.020in) were taken along the longitudinal plane, build direction. It will be noted that cylinder #2 had been machined into a dog bone of similar dimensions. This was done to identify if the machining had affected the hardness of the specimens.

2.8 Tension Tests

Tension tests are a method to calculate a material's elastic modulus, yield strength, and ultimate strength. A specimen is inserted into two grips, one on either end, and pulled apart in either a load control or strain-controlled test. Tension tests are preferred for two reasons. The test can be monitored by a strain gage easier and tension loads are more detrimental to materials than compressive loads. Tension tests must follow the ASTM E8 standards which sets specifications for flat or round specimen dimensions, based on the gage length and diameter, as well as the test

devices used [90]. Mechanical properties of a material are crucial when determining a material to use in an engineering application. A standard ensures rules are followed and that reported results can be trusted by engineers. However, powder metal materials are exempt from the specimen dimension standards set forth as an effort to keep pressing of materials to a specified area and density [90]. The specimens constructed in this study meet the fatigue standard for fatigue tests, this was done as the fatigue samples can be smaller and this helps to conserve material usage as well as fitting more samples per build plate. Hammond et al. ran tension tests on interrupted PBF AlSi10Mg to determine mechanical properties of interrupted and control specimens [74]. Wang et al. performed tension tests on 304L stainless steel made by AM direct energy deposition [86].

Tension tests were performed on an Instron 5869 with a 20kN load cell. Strain was monitored with a 10mm Instron extensometer with a 50% movement in either direction. Test were strain controlled at a rate of 0.001/s. Load and strain were captured by the computer and stress was calculated automatically based on the diameter of the specimen input into the computer. Each specimen was measured in the gage section three times to get an average diameter. The data was taken and plotted in Microsoft Excel to plot the stress vs. strain. The 0.2% offset method was used to obtain yield strength as well as the elastic modulus. The ultimate strength was taken from the stress at fracture. The samples tested from each experimental group for mechanical properties are as follows: cylinder #3,5,6 and dog bone #9,10,11.

CHAPTER III

RESULTS AND DISCUSSION

3.1 Results

Data was collected from specimens as outlined in the experimental methods section in the previous chapter. Results presented in this section will touch on a few key images and data with the remaining images inserted in the appendix. This is to provide a consistent flow and to keep key points presented in the results uncluttered. Each experiment was executed as outlined in the experimental design section and no major errors occurring to the specimens when building. During the restart procedure for the complete cool and 24 hour builds, the layers of powder spread were inconsistent for approximately 15 layers, ~0.450mm. Interrupted specimens for the complete cool and 24 hour experiments had a visible line on their surface at the location of interruption. This was not observed on the control or 5 min specimens. It is possible interruptions of a certain length will exhibit a similar surface characteristic similar to that observed in the complete cool and 24 hour builds. It is likely that any component that is interrupted in this fashion will exhibit a surface characteristic similar to the ones observed. The results are presented in the order they were taken.

X-ray Ct data taken indicated the presence of porosity spread throughout the specimens. There was no clear trend from this data if the porosity increased in specimens that were interrupted vs. those that were not. An image from the Volume Graphics studio for a control dog bone is given in Figure 3.1. The presence of porosity is evident in the control specimens. This is

consistent with literature on AM AlSi10Mg. The size distribution of pores in the porosity module indicated the presence of micropores, microns in diameter, consistent with some literature published on aluminum alloys [70] [78].

Figure 3.1 Control dog bone #5 with porosity and volume defect scale bars.

Control dog bone #5 showing porosity % and internal defect volume (mm^3). The right scale bar is 0.00 as this can not be changed to a smaller unit. Figure 3.3 shows the size distribution of the internal voids related to the right scale bar.

It is hypothesized that micropores can originate from hydrogen as well from high energy α-particle radiation that causes small atom clusters in the melt to vaporize [91]. The porosity analysis also confirmed the presence of larger voids including hot spots of porosity, areas of greater concentrations of voids. These tended to cluster near the surface of the material. Voids are color coded according to size as can be observed in the size distribution plot. It should be noted the right scale bar in the X-ray image shows the scale reading 0.00 the entire way through, but this does not correspond to the data presented in the size distribution plot that shows the

voids having an identified volume. The scale bar can not be adjusted to include more significant digits, nor can the scale be changed to a different unit.

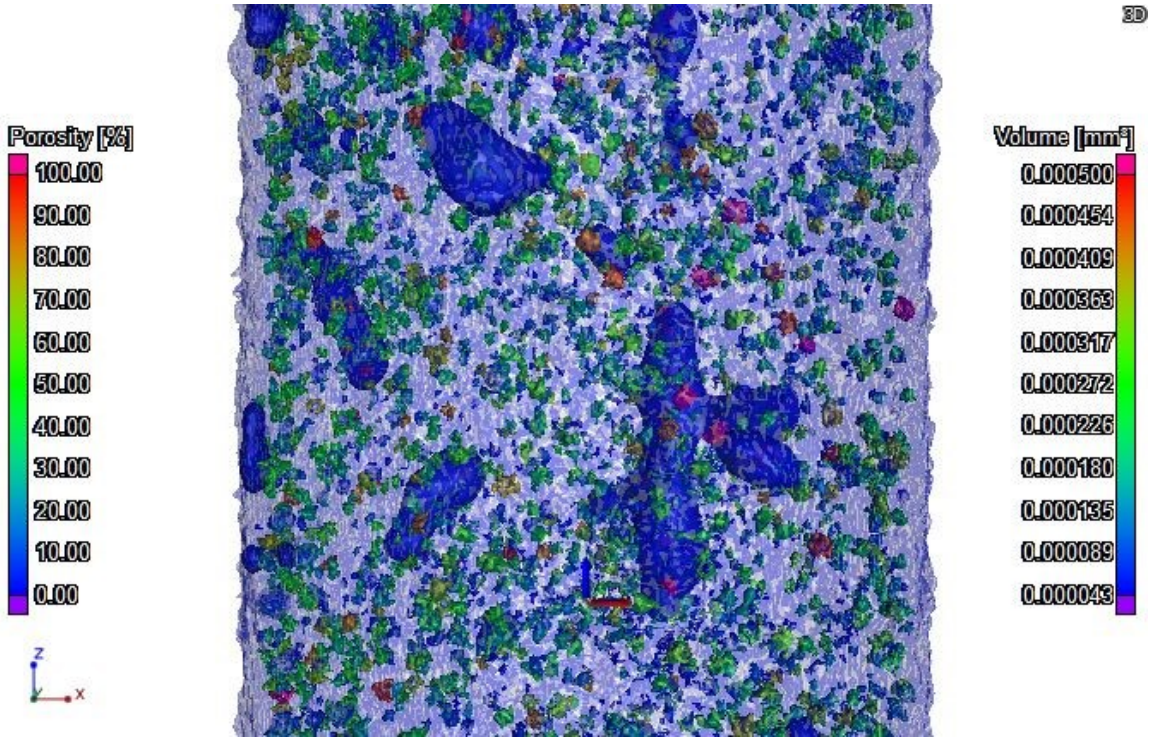

Figure 3.2 Control dog bone with porosity and volume defect scale bars zoomed to 40mm location.

Porosity image of control dog bone #5 zoomed in at 40 mm. Thew scale bars represent porosity and defect volume(mm^3). The entire specimen has a blue tint which corresponds to the porosity %, left scale bar. Individual pores are colored according to the defect volume, right scale bar.

The presence of spherical pores and lack of fusion pores was confirmed in micrographs taken from optical microscope images. Spherical pores dominated the micrographs in all samples spread throughout the entire specimen. Lack of fusion pores were observed in the region of interruption likely from the interruption and restart procedure where inconsistent layers of powder were applied. Within the lack of fusion pores partially melted powder particles could be observed. Oxygen is not soluble in aluminum and oxides are contained in lack of fusion pores

located at the pore boundaries [55]. From micrographs it seemed that the presence of spherical porosity increased slightly with each successive powder usage. This could occur from humidity in the lab environment that found its way onto the powder during handling and sieving creating gas porosity when melted.

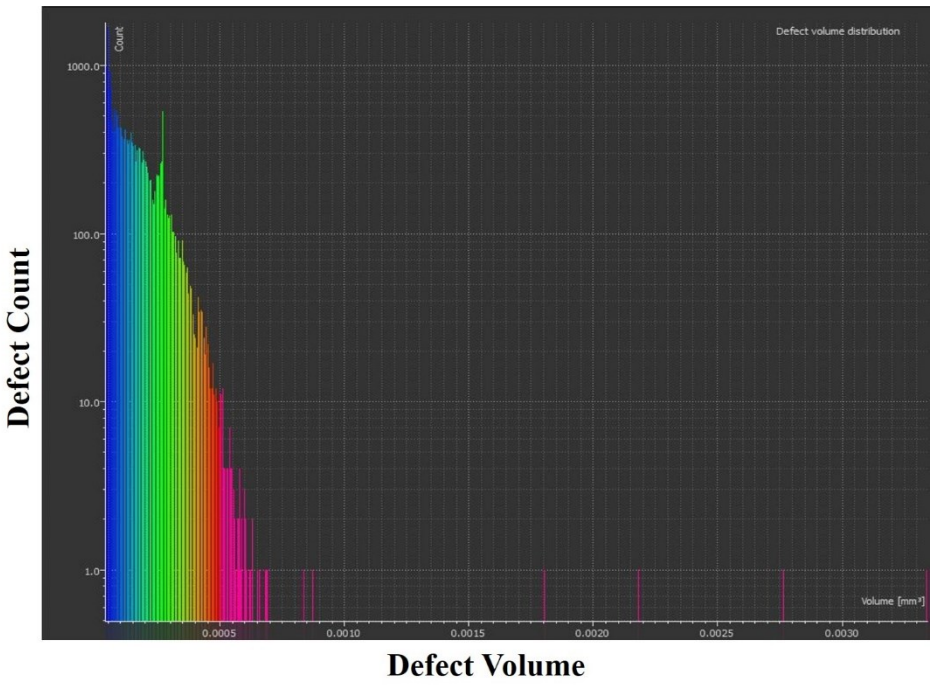

Figure 3.3 Defect count vs. defect volume size for control dog bone #5.

This image shows the size distribution of internal defects for control dog bone #5. This size distribution shows the presence of micropores. 10^2 mm^3 volume or less defines a micropore.

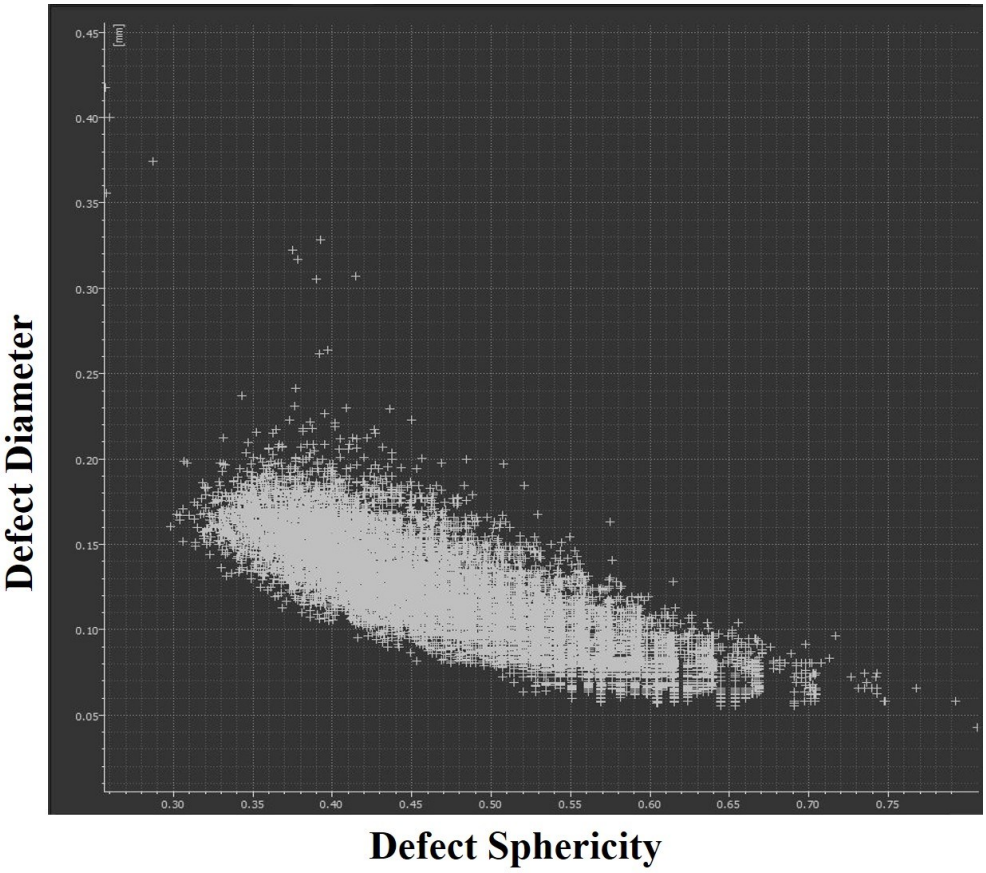

Figure 3.4 Defect diameter vs. sphericity of defect for control dog bone #5.

Plot showing the size of defect diameter (mm) vs. the sphericity of the defect for control dog bone #5. One represents a perfect sphere and zero a highly elongated pore.

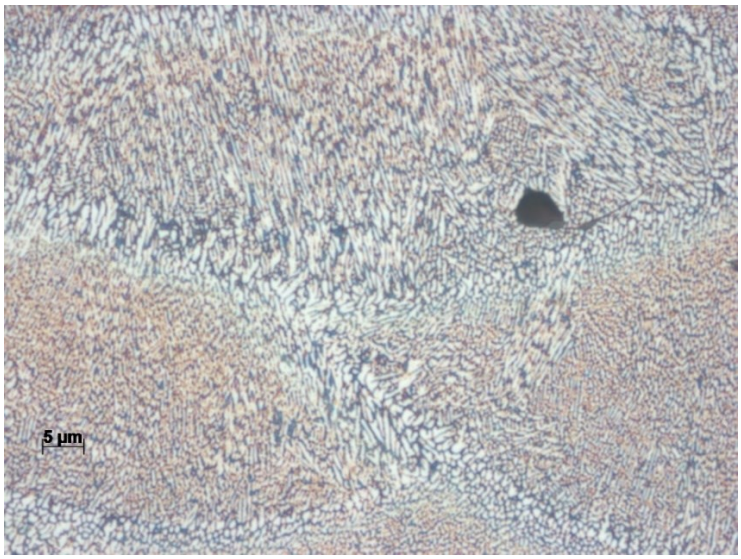

Figure 3.5 Microstructure as observed in control sample

Observed microstructure in control cylinder showing the fine, coarse, and heat affected zone. Control sample micrograph at 100x, 2.5x optovar zoom

Micrographs showed clear solidification tracks that can be observed coming into and out of the page, denoted by semi ellipse. There are solidification tracks that run horizontally but these are obscured by the other tracks. Using high magnification, 100x, the microstructure observed kept with previously reported literature [70] [74]. The microstructures can be divided into three separate regions; fine, coarse, and heat affected zone (HAZ). In the first region, fine aluminum cellular dendrites could be observed extending from edge of the coarse zone towards the middle region of the solidification track. Coarse zones could be observed along the edge of the solidification track with shorter but wider microstructure.

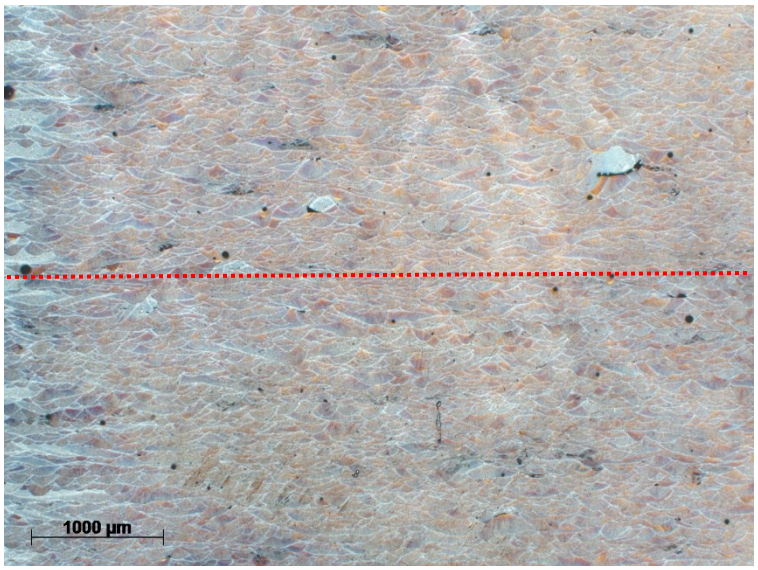

Figure 3.6 24 hour air cylinder. at 2.5x showing presence of spherical and LOF porosity

24 hour air cylinder at 2.5x magnification. Spherical porosity can be observed in this image. Image also shows the discoloration between the bottom and top portion of the sample. Interruption location denoted by dotted red line.

This zone consisted of α-aluminum equiaxed microstructure. There is no observable directionality to this zone. The length of equiaxed microstructure is much shorter than the fine zone, while the width of these grains is much larger. The HAZ microstructure consists of fibrous Si networks. The microstructure observed was consistent across all micrographs with no distinguishable difference to the microstructure in the interruption plane observed in optical microscope images.

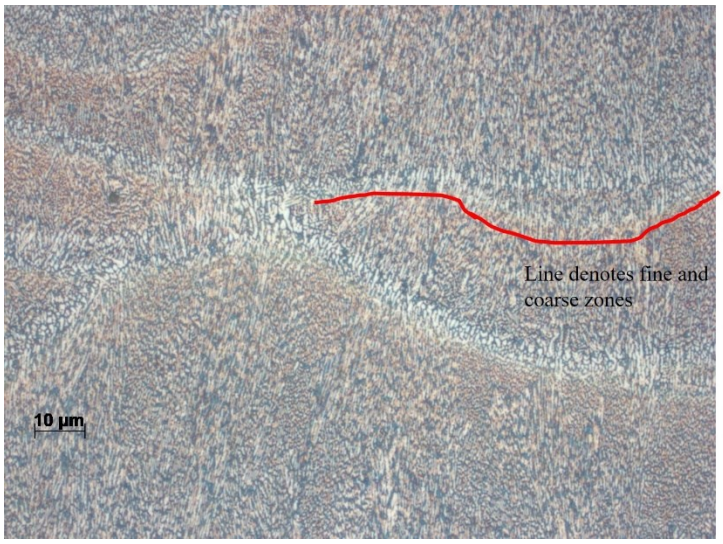

Figure 3.7 Microstructure as observed in 24 hour air cylinder interruption plane at 100x

Observed microstructure in 24 hour air exposure cylinder #4 showing the fine and coarse zones. The red line outlines the differences in the two zones. 100x

One unique feature that was observed on all 24 hour specimens was the presence of a clear line of discoloration. This discoloration matched the interruption plane across all 24 hour specimens viewed with the optical microscope. This discoloration is attributed to the fact the samples were artificially age hardened while the interruption occurred. Aluminum is commonly heat treated to obtain desirable mechanical properties through a combination of solution heat treatments, cold working, quenching/cooling and artificial aging. One common heat treatment for this alloy is the T6 heat treatment [62]. This heat treatment consists of a solution heat treatment at an elevated temperature (approximately 75% of melt) for a short period of time, approximately 3 hours. The sample is cooled, and then artificial aging occurs by treating the material at a lower temperature (approximately 25% of melt) for an extended period, 6-10 hours [78]. The 24 hour samples were artificially aged when interrupted as the build platform was held at 170°C for 24 hours. This satisfies the temperature and time requirements for artificial age hardening to occur.

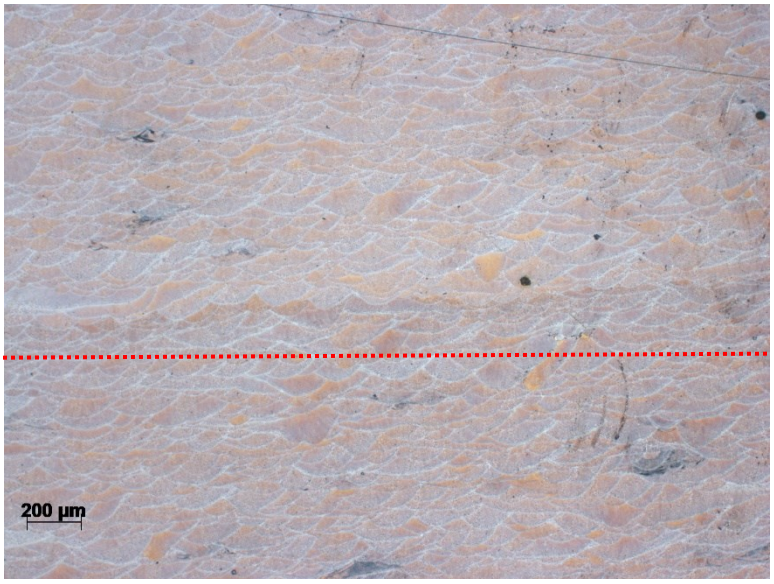

Figure 3.8 24 hour dog bone interruption plane

24 hour dog bone #1 observed at 5x magnification. The discoloration can also be observed. The interruption location is denoted by a dotted red line.

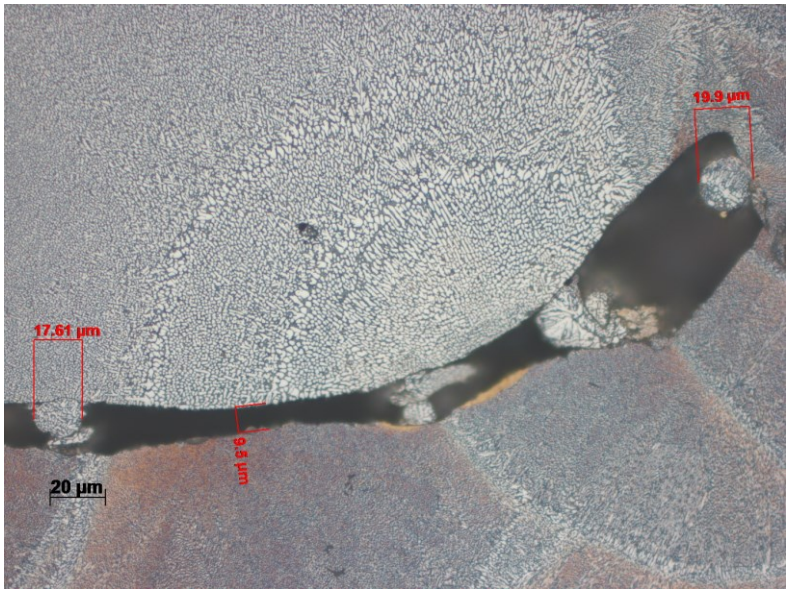

Figure 3.9 24 hour air cylinder lack of fusion pore

24 hour air cylinder #4 above interruption planes showing lack of fusion void with unmelted powder particles at 50x zoom.

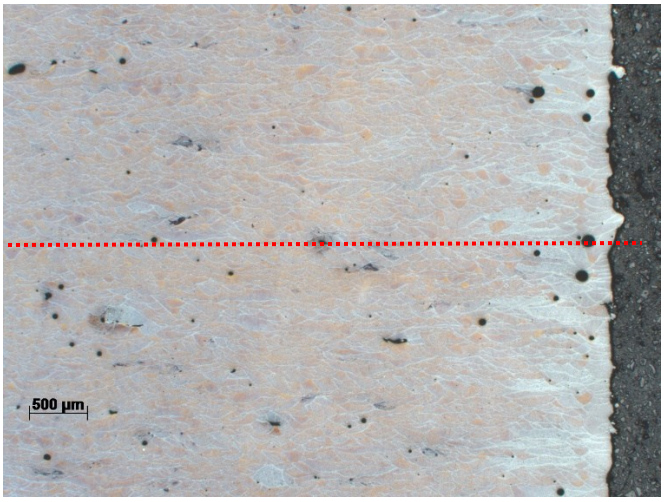

Figure 3.10 Complete cool cylinder showing large spherical pores

Complete cool cylinder #4 showing large spherical pores towards surface at 2.5x zoom. The interruption location is denoted by the red bar.

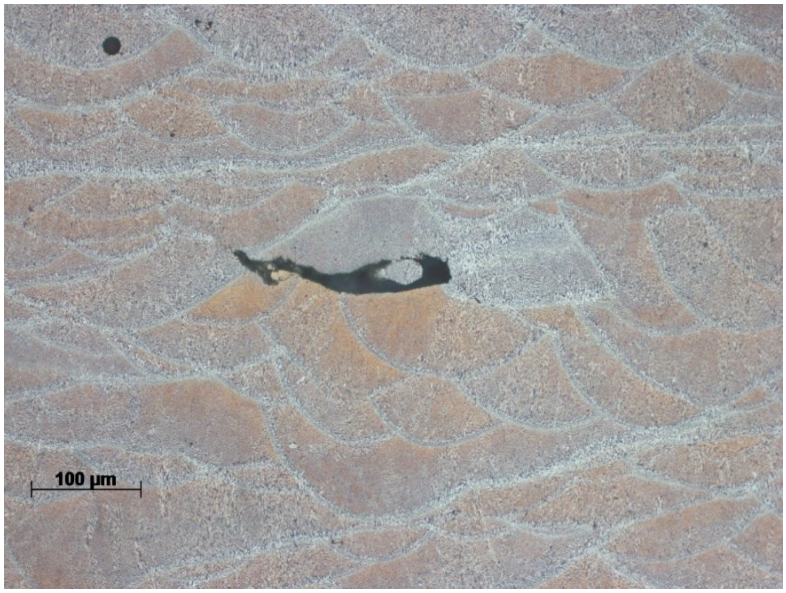

Figure 3.11 Complete cool air cylinder exposure showing a lack of fusion pore

Complete cool cylinder #4 showing lack of fusion pore with partially melted powder particle at 20x zoom.

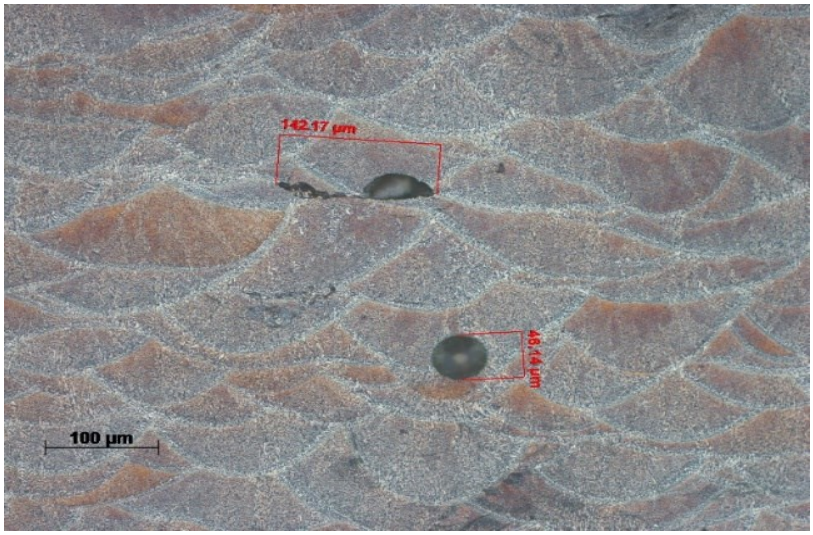

Figure 3.12 24 hour air cylinder showing size of spherical pores

24 hour air cylinder #4 showing a spherical defect and semi-circular defect in interruption zone. Both defects are bordered by the solidification tracks. Red lines denote size of pores in microns.

EDS maps and spectrums taken from specimens showed the presence of oxygen in all specimens. The highest concentrations of oxygen occurred in lack of fusion pores where oxides are known to be found [53] [55]. The oxides observed in air exposed specimens did not show increased wt% of oxygen versus oxides observed in non air exposed. EDS scans of bulk material were taken showing very minimal presence of oxygen at less than 0.4%. This oxygen presence could be from the polished specimens forming an oxide layer as aluminum naturally does. EDS maps showed the presence of oxygen on the surface of powder particles in LOF pores. The oxide formation could have occurred on the powder particle prior to melting or could have formed after polishing was complete.

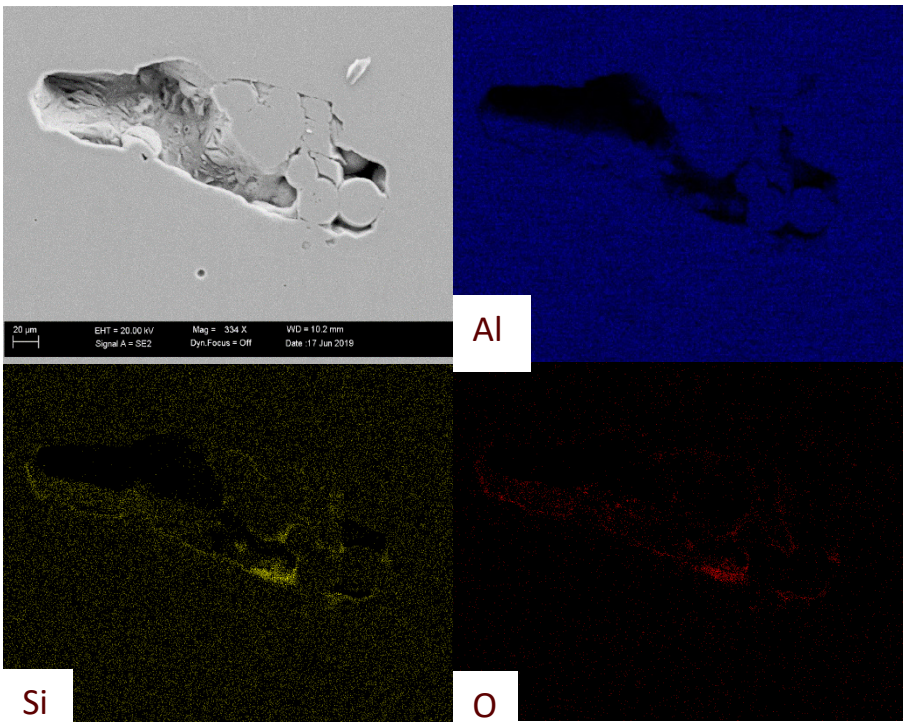

Figure 3.13 EDS of cool air exposure.

EDS map of complete cool air exposure showing Al, Si, O. This map shows the presence of oxygen in the partially melted powder inclusion.

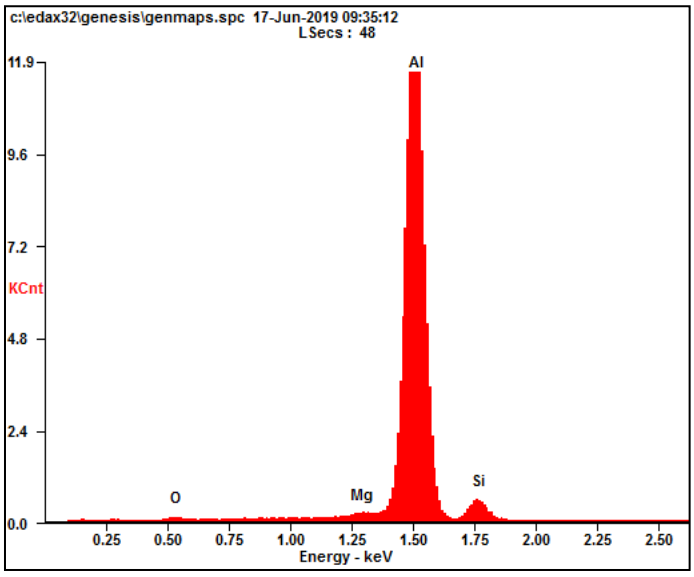

Figure 3.14 Spectral lines of complete cool air from Figure 3.13.

Spectral lines for EDS map in Figure 3.13.

Table 3.1 Table of element wt% of the spectral line in Figure 3.14.

Element	Wt%	At%
O	01.50	02.51
Mg	00.84	00.93
Al	89.46	88.75
Si	08.19	07.81
Matrix	Correction	ZAF

This table shows elemental wt% for the spectral line in Figure 3.14 and EDS map in 3.13 for complete cool air.

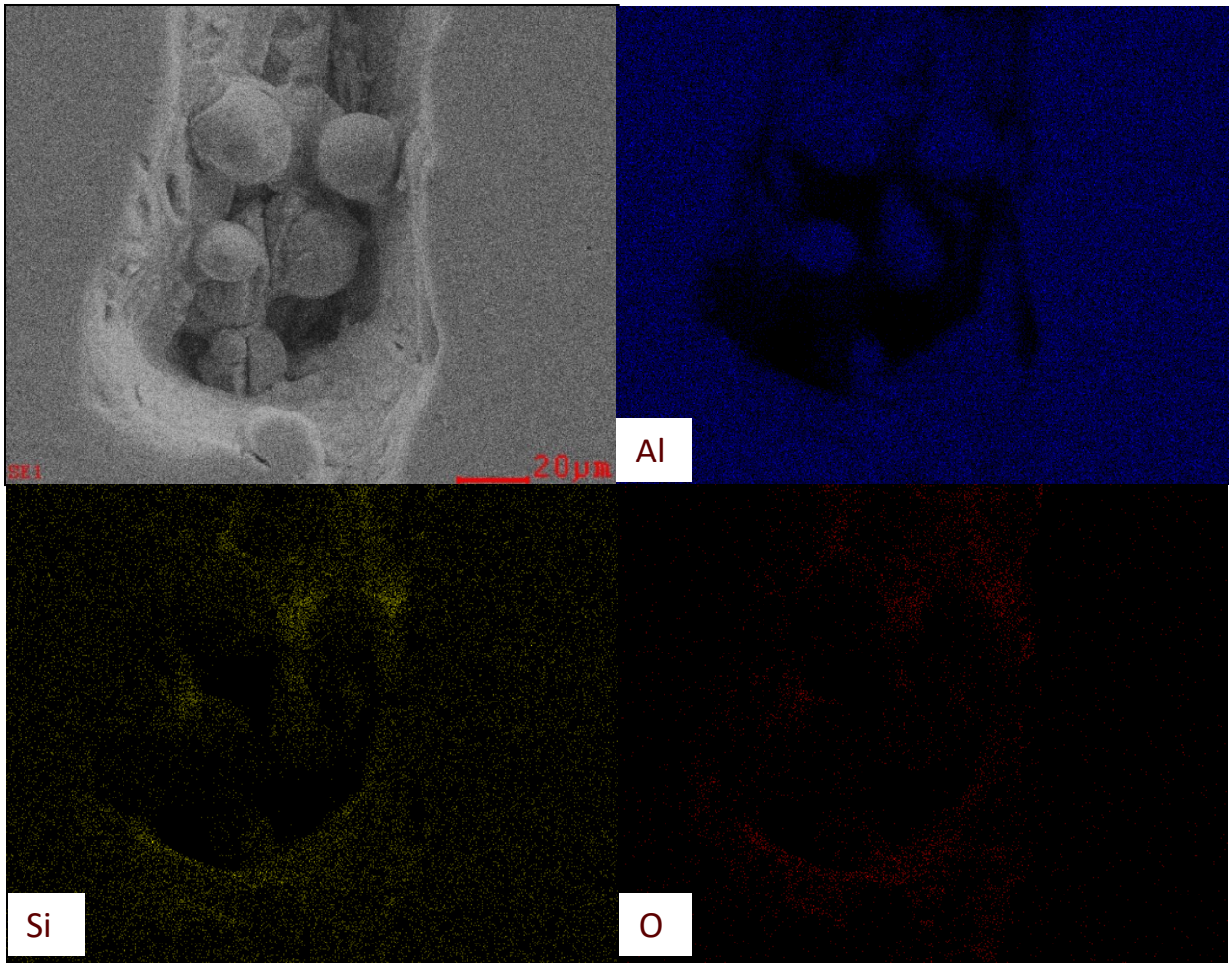

Figure 3.15 EDS map of 5 minute air exposure

EDS map of 5 minute air exposure showing Al, Si, O. The presence of oxygen was observed amongst partially melted powder along border of inclusion.

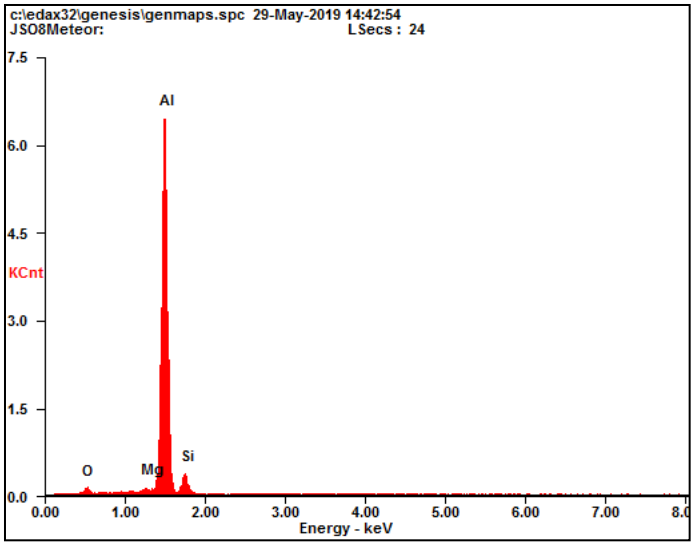

Figure 3.16 Spectral lines of 5 minute air from Figure 3.15

Spectral lines of 5 minute air from Figure 3.15

Table 3.2 Table of elemental wt% of spectral line in Figure 3.16.

Element	Wt%	At%
O	04.34	07.14
Mg	00.64	00.69
Al	84.47	82.30
Si	10.55	09.87
Matrix	Correction	ZAF

Table showing elemental wt% of spectral line in Figure 3.16 and EDS map in Figure 3.15 for 5 minute air.

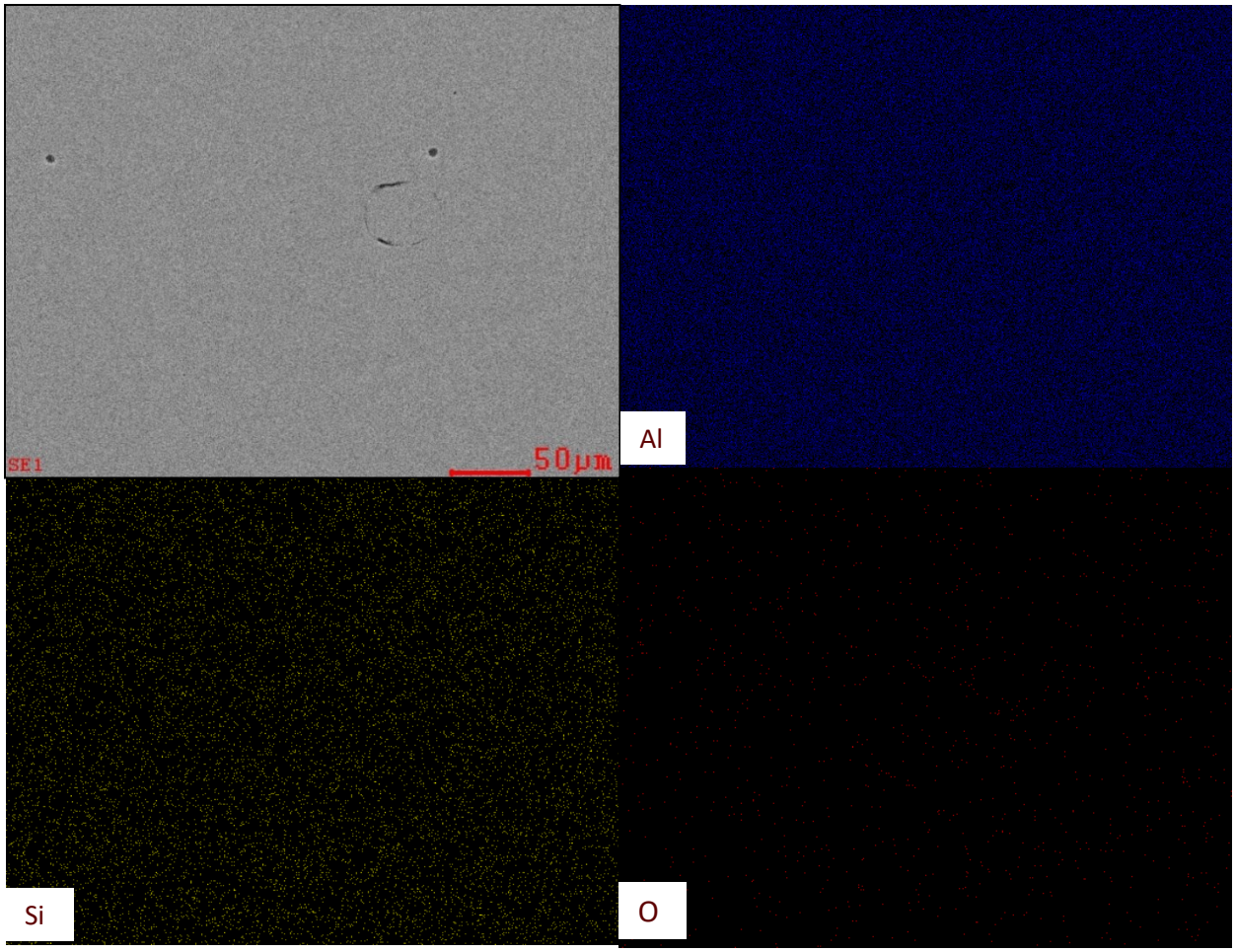

Figure 3.17 EDS map of complete cool no air

EDS map of complete cool no air exposure showing Al, Si, O. Shows low presence of oxygen on the surface. Any oxygen that is detected could be the result of oxidation that occurred after polishing.

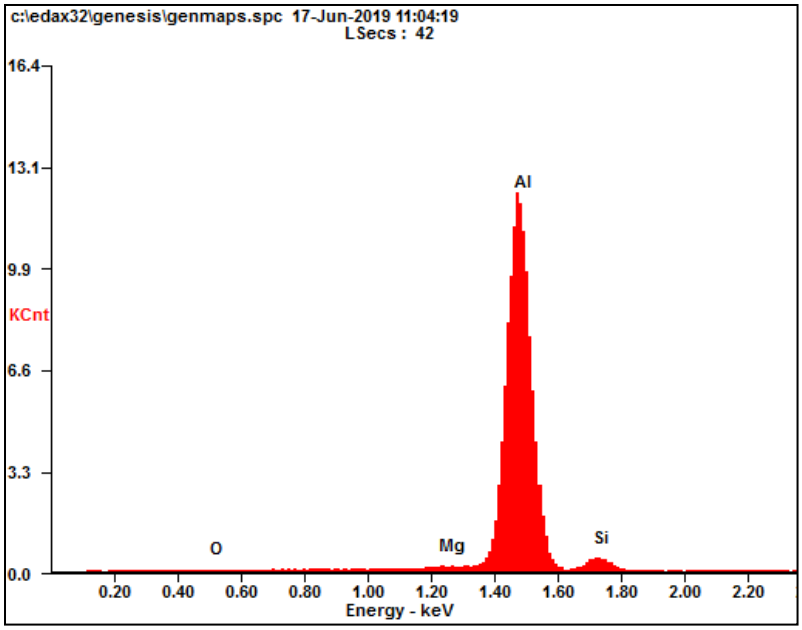

Figure 3.18 Spectral line for complete cool no air in Figure 3.17.

Spectral line for complete cool no air EDS map in Figure 3.17.

Table 3.3 Table of elemental wt% of spectral line in Figure 3.18.

Element	Wt%	At%
OK	00.44	00.75
MgK	00.76	00.84
AlK	91.21	91.13
SiK	07.59	07.28
Matrix	Correction	ZAF

Complete cool no air exposure wt% of spectral line in Figure 3.18 and EDS map in Figure 3.17.

Vickers microhardness data collected showed consistent hardness from all specimens. Lower HV measurements can be observed in some samples attributed to indenting on top of or around pores with in the material. The presence of porosity would soften the material creating a larger indent and decreasing the HV measurement. The 24 hour specimens exhibited the highest hardness, which can be attributed to the artificial aging that those specimens underwent when interrupted. Artificially aging is also known as precipitation hardening and increases the tensile strength of the material however, this does decrease the toughness and ductility of the material [62]. In this case, the Mg_2Si precipitates are strengthened. The increase in strength from precipitate hardening is what caused the 24 hour samples to have the highest Vickers hardness.

Figure 3.19 Vickers Microhardness measurements.

Vickers microhardness for control, 24hr, and complete cool specimens. 24hr specimens have higher hardness due to artificial aging during the interruption

Stress strain data obtained from the tension tests indicated no clear impact of build interruptions on mechanical properties. Elastic modulus, yield strengths, and ultimate strengths for all data points were consistent with each other and performed better than Renishaw reported values. The control group exhibited the highest ultimate strength but also had the lowest yield strength. The 24 hour experiments did have adequate yield and ultimate strength, but these values were not significantly greater than any of the other experiments. The percent elongation to failure for as built samples performed consistent with literature however the machined samples exhibited a reduction in these values. This is counterintuitive to what was expected as machined samples tend to perform better than as built samples due to the elimination of surface defects, better surface finish, and the introduction of compressive stress. It is hypothesized the machining

of the samples caused the reduction in the elongation to failure. Visually the gage section looked concentric with the grip sections, but this is hard to confirm with just observation from the naked eye.

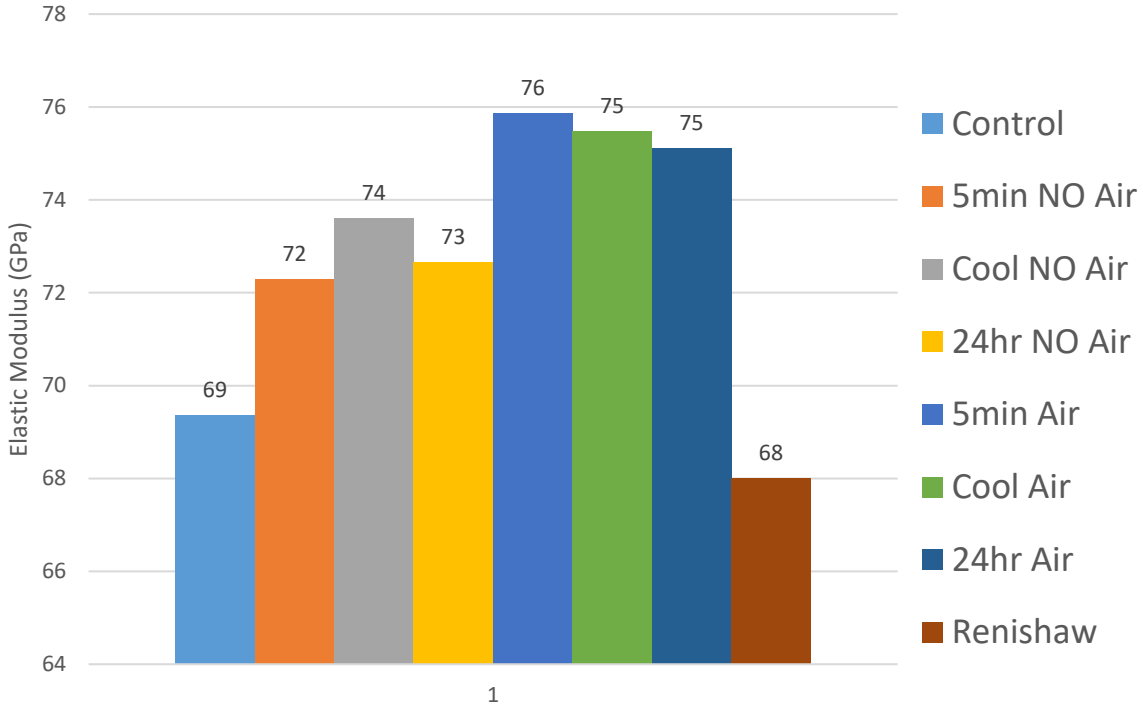

Figure 3.20 Elastic modulus for all experimental groups.

Elastic modulus average from all specimens in each experimental group, plotted against Renishaw reported values.

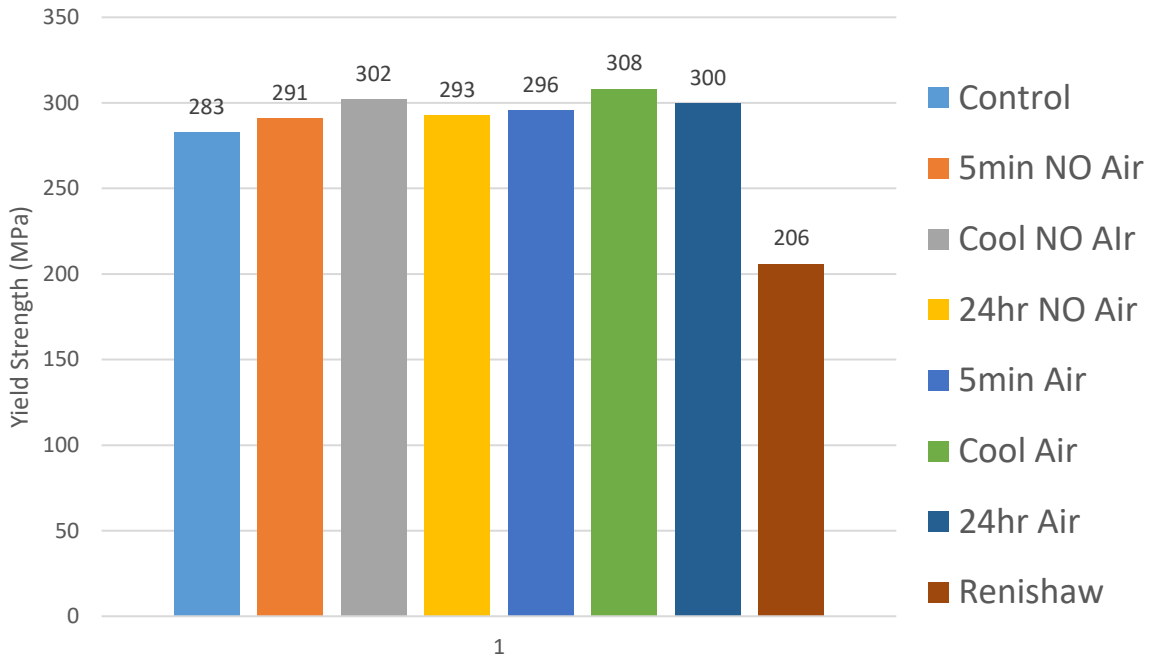

Figure 3.21 Yield strength for all experimental groups.

Yield strength average from all specimens in each experimental group, plotted against Renishaw reported values.

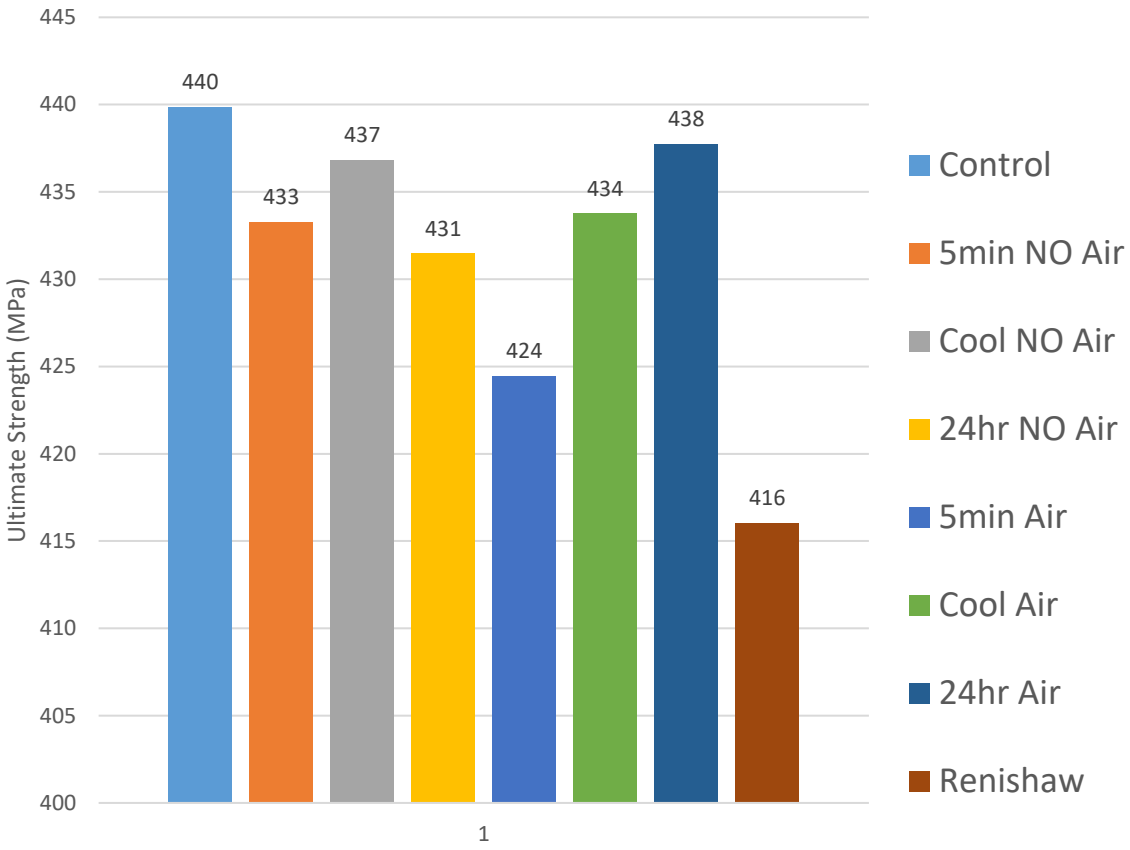

Figure 3.22 Ultimate strength for all experimental groups.

Ultimate strength average from all specimens in each experimental group, plotted against Renishaw reported values.

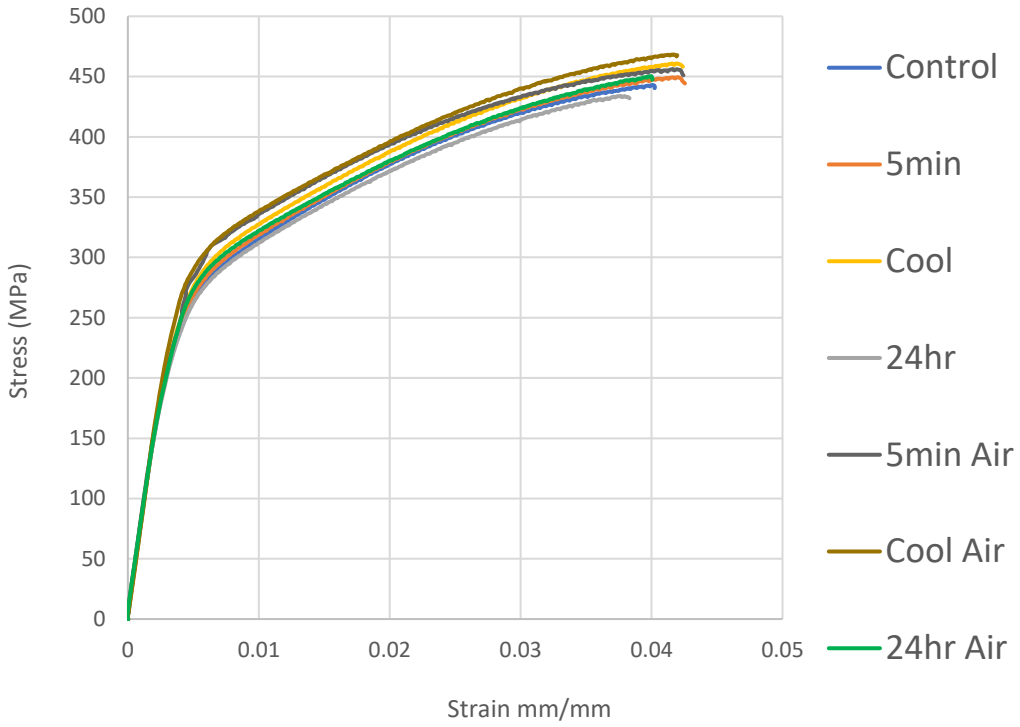

Figure 3.23 Engineering stress-strain curve for select dog bone specimens.

Engineering stress strain for all #9 dog bone specimens from all experiment groups.

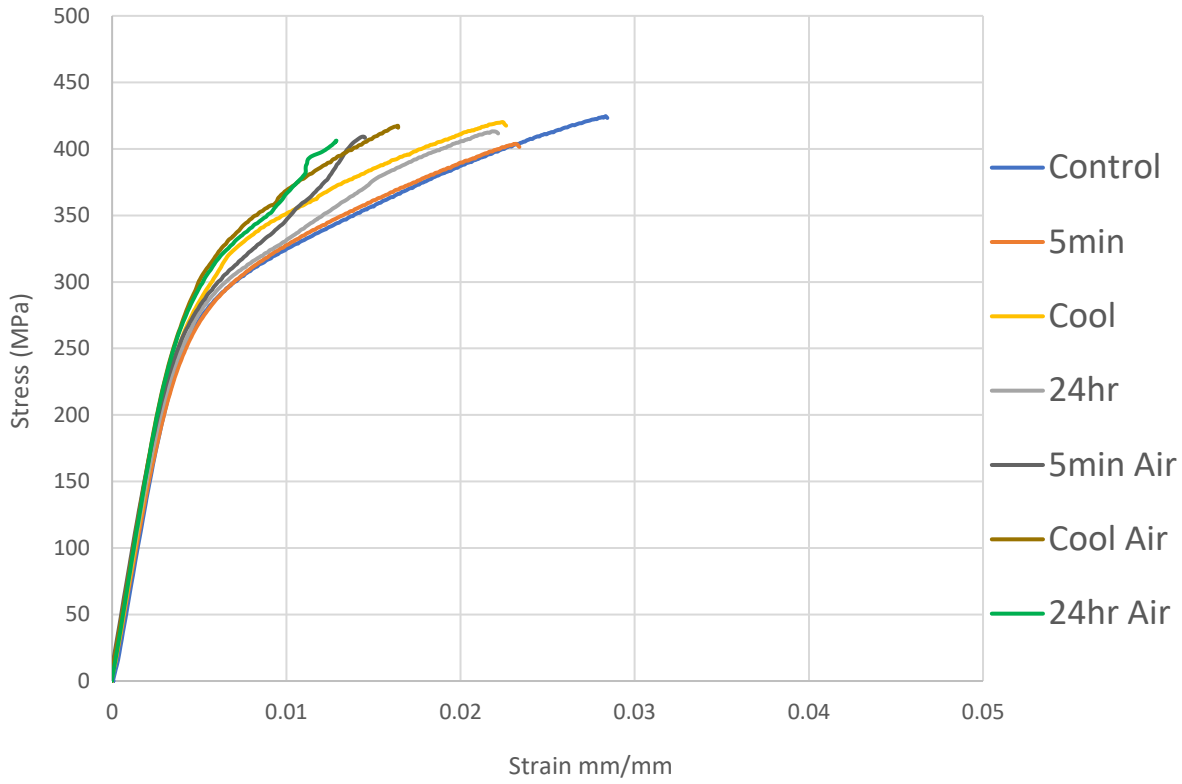

Figure 3.24 Engineering stress- strain curves for select machined specimens.

Engineering stress strain for all #6 machined specimens from all experiment groups. The machined control sample had the longest % elongation vs. the other samples. Machined specimens showed reduced % elongation at failure compared to as build dog bones.

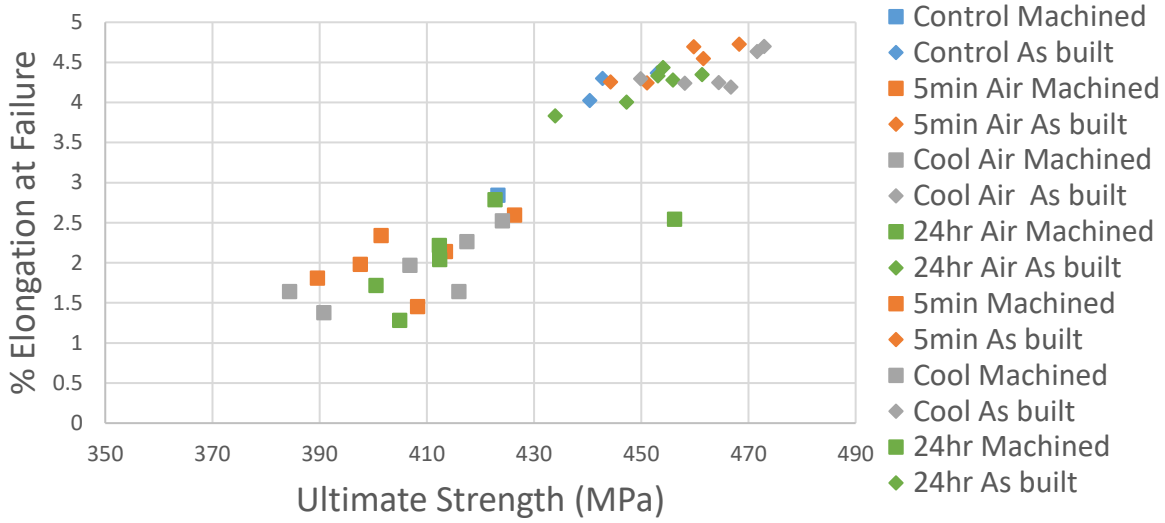

Figure 3.25 Percentage elongation at failure for all experiment groups.

Color groups are the same based on time period of interruption. Square symbols denote the machined specimens and diamond symbols denote the as built specimens.

Fractures from the interrupted builds were not localized to the interruption zone. Only 6/24 (25%) of the specimens fractured for all 5 minute and complete cool experiments. The lack of failures can be attributed to a few things. The oxides formed during the air exposures were broken up upon restarting due to the laser beam distributing. This phenomenon has been observed by Buchbinder et al. as well as Louvis et al [72][30]. This makes the presence of oxides not as detrimental to failure compared to the large presence of porosity. The presence of porosity throughout the specimens dominated the fractures due to voids located near the surface of the material likely contributing to failure. The 24 hour experiments experienced the greatest number of fractures in the interruption with 6/12 (50%) of the specimens fracturing at the location of interruption. This failure rate can be attributed to three phenomena: the increased brittleness from the artificial aging region to newly deposited material that occurred, the presence of oxides, and the lack of fusion voids in this region.

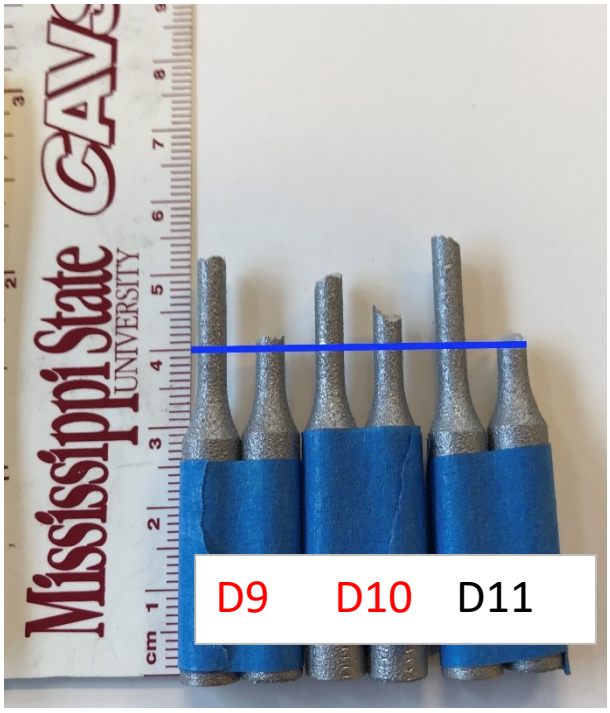

Figure 3.26 24 hour air dog bone macroscopic fracture pictures.

Fracture image showing location of fracture for 24 hour air dog bones. Blue line indicates the interruption location. Red text denote what specimens were chosen for fractography.

To investigate different fracture surfaces, fracture specimens were chosen to observe surfaces near and away from the interruption zone. All fracture surfaces away from the interruption zone exhibited fibrous appearances indicative of a ductile fracture. There was no indication of cup and cone failure associated with ductile fractures, but this alloy does not exhibit significant necking. Most of the samples that fractured away from the interruption plane broke at a 45-degree angle. The control dog bone #11 fractured above the interruption zone and upon examination spherical voids near the exterior surface were found, a possibly cause of failure.

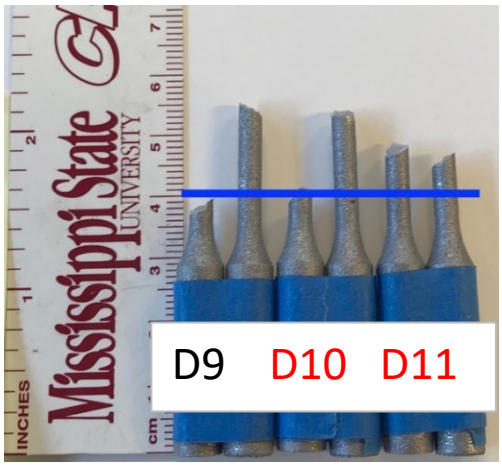

Figure 3.27 Control dog bone macroscopic fracture image.

Fracture image showing location of fracture for control dog bones. Blue line indicates the interruption location. Red text denote what specimens were chosen for fractography.

Complete cool air cylinder #6 was also examined with several large void's observable near the edge of the cylinder. Both fracture surfaces, control dog bone #11 and complete cool air cylinder #6, were located away from the interruption plane.

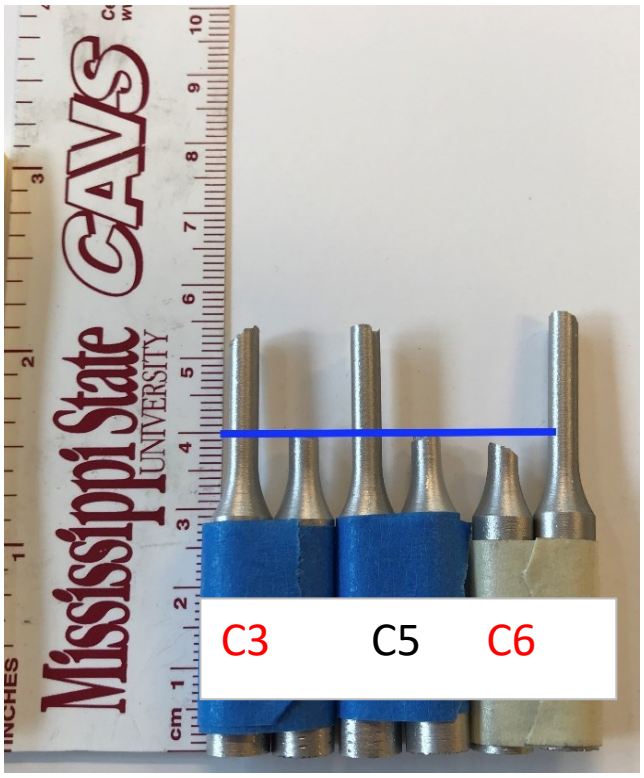

Figure 3.28 Macroscopic fracture image of 24 hour air cylinders.

Fracture image showing location of fracture for 24 hour air cylinders. Blue line indicates the interruption location. Red text denote what fracture surfaces were chosen for fractography.

Fracture surfaces near the interruption plane included 24 hour air dog bone #9 and 24 hour cylinder #3. Both fracture surfaces maintained the fibrous appearance but exhibited a flatter appearance, less variation in overall fracture surface. This flat fracture surface resembles a brittle failure. The flat fracture appearance could be the result of the artificial aging combined with the lack of fusion re-melting that occurred. All fracture surfaces for the 24hr experiments exhibited the flat fracture appears, resembling a brittle fracture.

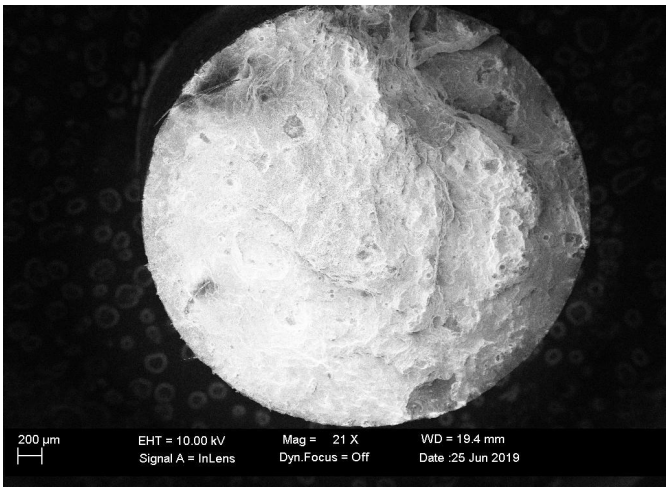

Figure 3.29 Control cylinder #3 fracture surface.

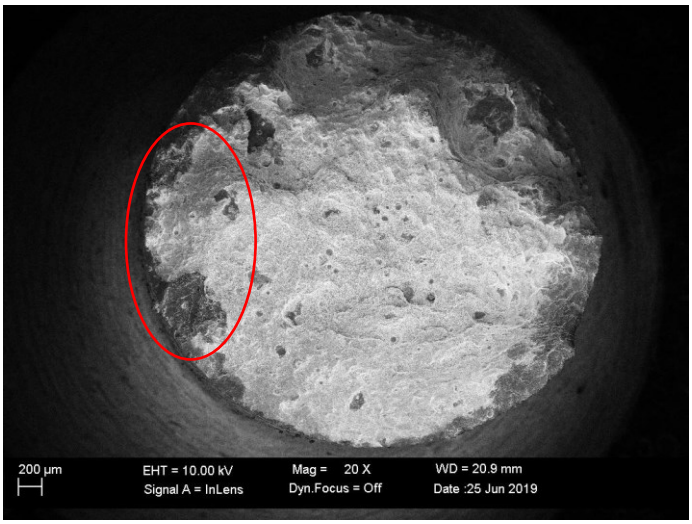

Figure 3.30 5 minute air cylinder #5 fracture surface

This specimen fractured in the approximate area of interruption likely due to large lack of fusion pores over the entire fracture surface. The red circle denotes the location of the next photo's focus.

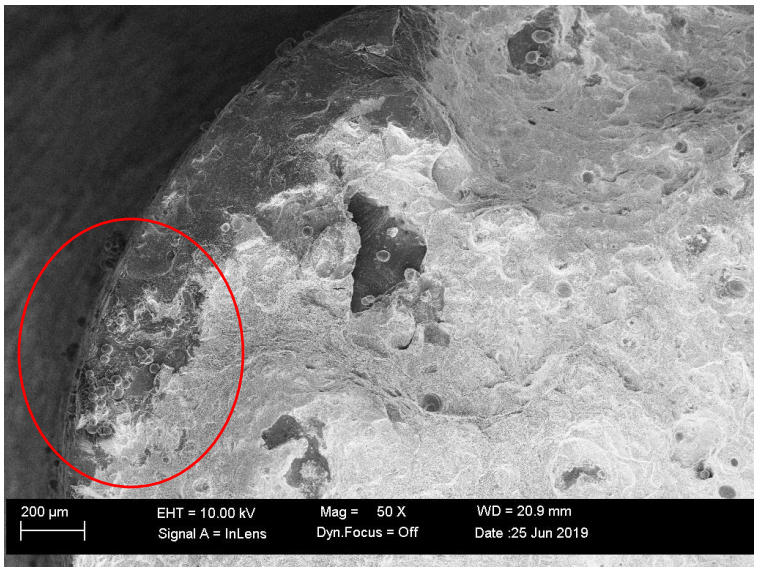

Figure 3.31 5 minute air cylinder #5 zoomed in fracture surface.

This image shows the presence of unmelted powder particles along the edge of the sample. Given this is a machined sample it is surprising to see the unmelted powder along the surface indicating partial melting occurred inside the sample.

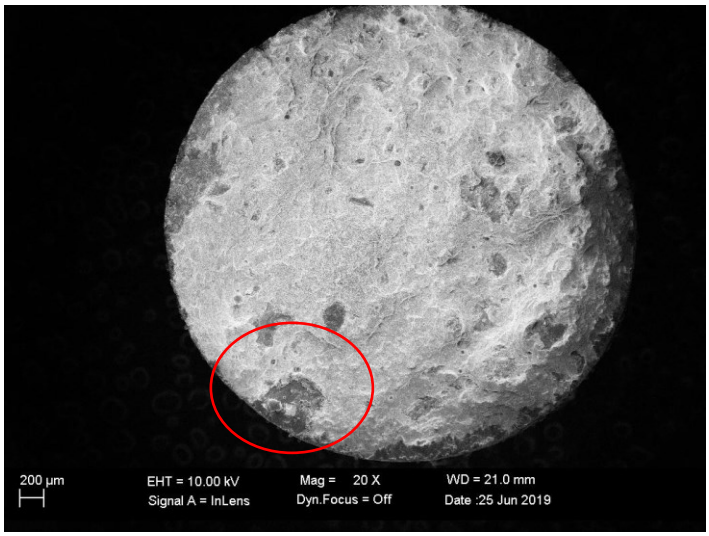

Figure 3.32 24 hour air cylinder #6 fracture surface

24 hour air cylinder #6 shows the presence of large voids in the inner portion of fracture surface. Also, the presence of a large piece of material missing on bottom portion circled in red.

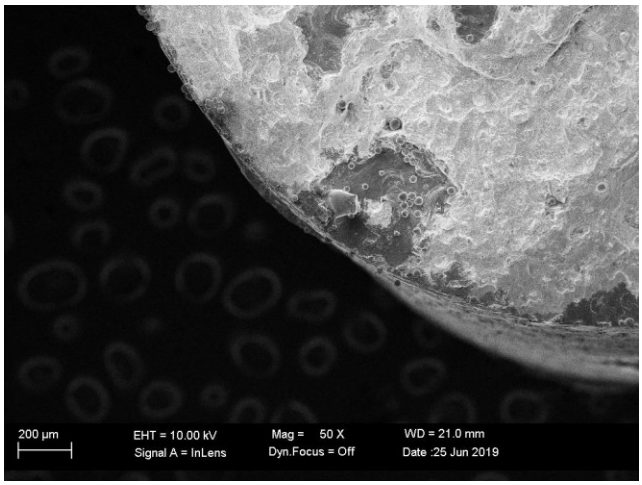

Figure 3.33 24 hour air cylinder #6 fracture surface zoomed to red circle

24 hour air cylinder #6 shows the presence of lack of fusion voids towards surface of specimen.

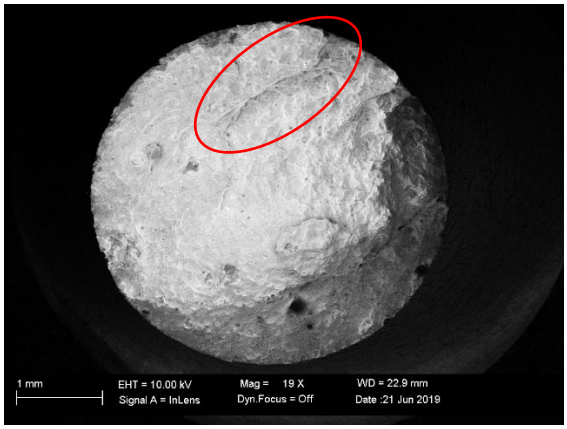

Figure 3.34 24 hour air cylinder #3

24 hour air cylinder #3, fractured at interruption location. Red circle indicates location of next picture.

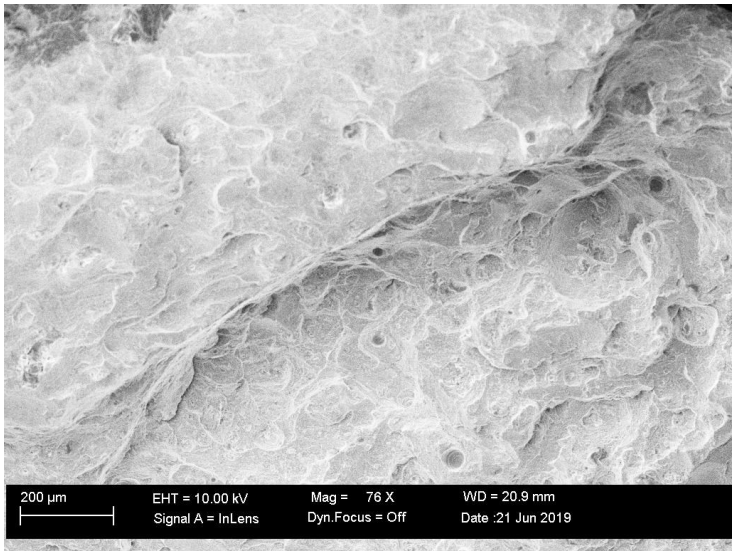

Figure 3.35 24 hour air cylinder #3 zoomed into red circle.

This is the result of two cracks that have come together and forced the fracture in this location.

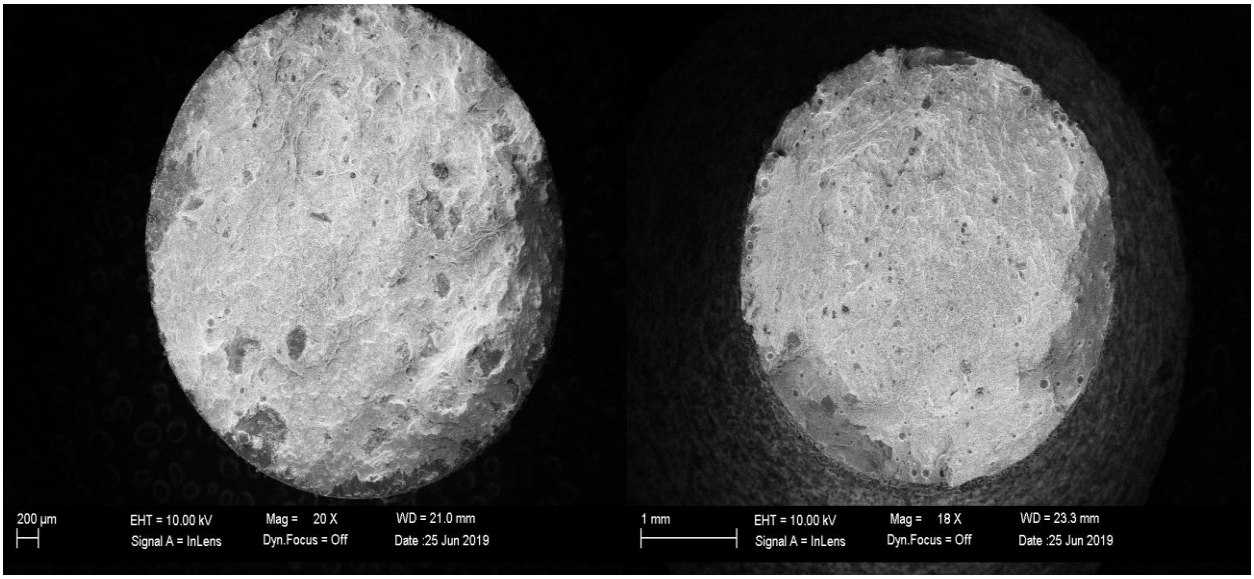

Figure 3.36 Fracture surface comparison between cylinder # 6 and dog bone #9 from 24 hour air.

The cylinder fractured above the interruption location. The dog bone fractured at the interruption location. The presence of large lack of fusion voids is more evident in the left picture, cylinder. The right side of the dog bone has greater presence of spherical voids located across the fracture surface.

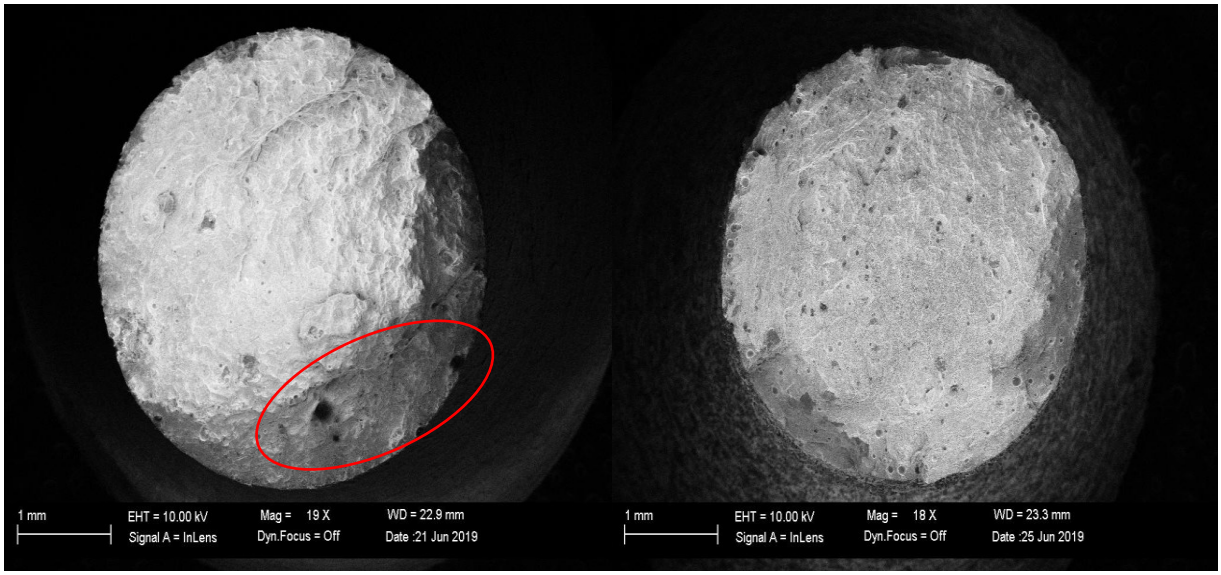

Figure 3.37 Fracture surface comparison between cylinder #3 and dog bone #9 from 24 hour air.

Both fractured at the location of interruption. Presence of very large pores circled in red on the cylinder, left image. The dog bone has the presence of many spherical voids across the fracture surface.

CHAPTER IV

CONCLUSION AND FUTURE WORK

4.1 Conclusion

The effect of build interruptions on PBF AlSi10Mg was investigated in this study. The interruptions were categorized into three time periods of interruptions: 5 minutes, complete cool (12hrs), and 24 hours each with no air and air exposure. X-ray CT, optical micrographs, EDS, EBSD, Vickers microhardness and tension tests were utilized to determine the impact build interruptions have on produced specimens.

- X-ray Ct results and optical micrographs confirmed the presence of porosity across all samples as well as the lack of fusion voids around the interruption zone. Porosity is a common problem with additive manufacturing and can be the result of trapped gases, as well as lack of fusion from insufficient melting. The insufficient melting can be induced from improper scan strategies. Porosity was observed in optical micrographs spread throughout the gage section. No increased porosity was associated with the interruption location.
- EDS results showed the presence of oxygen in lack of fusion voids, a place oxides are observed in literature. Presence of oxides has been observed in all reported literature for PBF AlSi10Mg. Oxides in aluminum form with minimal oxygen present. While the build chamber is inert, there is still trace elements of oxygen present that can form oxides. The air exposure during interruptions did increase

the percentage of oxygen detected in EDS scans, particularly in the interruption location.

- Mechanical properties from each test group performed better than Renishaw provided documentation and equal with other reported results on AlSi10Mg [78][74]. There was a significant decrease in the percentage elongation of failure in the machined specimens versus the as built specimens. This reduction in elongation also corresponded to reduced ultimate strength for all machined specimens. The reduction in elongation was surprising as machined samples typically perform better that as built due to compressive stress introduction from machining as well as defect removal since porosity tends to be clustered near the surface.
- Vickers hardness measurements showed consistent hardness across the tested samples with no decrease in hardness around the interruption location. The hardness of 24 hours showed an increase versus the control due to artificial aging occurring while interrupted. A result of the heated elevator being maintained at 170° C. This also corresponded to an increase in the ultimate strength of the 24 hour experiments.
- Specimens failed in various locations indicating the interruption plane did not dominate the failure location for the 5min and complete cool experiments. The 24hr experiments experienced 50% of specimens failing in the interruption location indicating this time period of interruption can dictate failure location. The interruption, introduction of oxides, and artificial age hardening all contributed to the failure of these samples in that location.

The results from the experiments did not fully support the hypothesis. Specimens from all experimental groups did not exhibit significant reduction in mechanical properties and performed well. However, the reduction in percentage elongation to failure for machined samples was surprising. The 24hr experimental cases experienced the greatest failures in the interruption location indicating this interruption is the most detrimental from the two other time interruptions. The exposure of air during interruptions did not significantly impact performance or contribute to failure location. This work identifies the need for proper restart procedures and the ability to detect interruptions to the PBF processes as soon as possible in order to minimize impact to specimens. This study presents evidence that interruptions to the PBF process do not significantly impact mechanical properties, however the interruption might dictate the location of failure. This study is important to industries that utilize PBF processes as it indicates interruptions are not detrimental on mechanical performance. However, the interruption could dictate the failure location which is something that could be of interest to some manufactures who design components to fail in specific locations for certain applications.

There are some limitations to this study concerning the machine and mechanical properties collected. The performance of these specimens could be dependent on the machine and process parameters used. Each PBF machine is constructed different and utilizes different implementation of process parameters that could affect the mechanical properties. There were no fatigue tests run on these samples and it is likely that interrupted specimens could exhibit a reduction in fatigue performance from the interruptions. The investigation of fatigue performance was not investigated in this work. Fatigue failure is a surface driven phenomenon but can also be affected by the presence of internal porosity. Studying the effect of interruptions

to fatigue performance would provide additional data into the mechanical characterization of the interrupted builds.

4.2 Future Work

Further investigation involves a stress relief heat treatment on remaining samples to determine the effect heat treatment (300°C in argon for 2 hours, air cool) has on interrupted PBF AlSi10Mg. Oxygen content analysis is to be conducted to determine the extent of oxygen content in the interruption plane. This is being conducted at the Army Research Lab in Maryland and will be completed once their Leco machine is operational again. Nano indentation will be performed to allow indenting on individual deposited layers as well as let indenting near oxides occur.

REFERENCES

[1] W. E. Frazier, "Metal additive manufacturing: A review," *J. Mater. Eng. Perform.*, vol. 23, no. 6, pp. 1917–1928, 2014.

[2] K. V. Wong and A. Hernandez, "A Review of Additive Manufacturing," *ISRN Mech. Eng.*, 2012.

[3] D. Ding, Z. Pan, D. Cuiuri, and H. Li, "Wire-feed additive manufacturing of metal components: technologies, developments and future interests," *Int. J. Adv. Manuf. Technol.*, vol. 81, no. 1–4, pp. 465–481, 2015.

[4] D. Herzog, V. Seyda, E. Wycisk, and C. Emmelmann, "Additive manufacturing of metals," *Acta Mater.*, vol. 117, pp. 371–392, 2016.

[5] W. Gao *et al.*, "The status, challenges, and future of additive manufacturing in engineering," *Comput. Des.*, vol. 69, pp. 65–89, 2015.

[6] K. I. Schwendner, R. Banerjee, P. C. Collins, C. A. Brice, and H. L. Fraser, "Direct laser deposition of alloys from elemental powder blends," *Scr. Mater.*, vol. 45, no. 10, pp. 1123–1129, 2001.

[7] W. J. Sames, F. A. List, S. Pannala, R. R. Dehoff, and S. S. Babu, "The metallurgy and processing science of metal additive manufacturing," *Int. Mater. Rev.*, pp. 1–46, 2016.

[8] T. DebRoy *et al.*, "Additive manufacturing of metallic components – Process, structure and properties," *Prog. Mater. Sci.*, vol. 92, pp. 112–224, 2018.

[9] W. Cao and Y. Miyamoto, "Freeform fabrication of aluminum parts by direct deposition of molten aluminum," *J. Mater. Process. Technol.*, 2006.

[10] E. R. Denlinger, J. C. Heigel, P. Michaleris, and T. A. Palmer, "Effect of inter-layer dwell time on distortion and residual stress in additive manufacturing of titanium and nickel alloys," *J. Mater. Process. Technol.*, vol. 215, pp. 123–131, 2015.

[11] J. A. Slotwinski, E. J. Garboczi, P. E. Stutzman, C. F. Ferraris, S. S. Watson, and M. A. Peltz, "Characterization of Metal Powders Used for Additive Manufacturing," *J. Res. Natl. Inst. Stand. Technol.*, vol. 119, p. 460, 2014.

[12] S. M. Thompson, L. Bian, N. Shamsaei, and A. Yadollahi, “An overview of Direct Laser Deposition for additive manufacturing ; Part I : Transport phenomena , modeling and diagnostics,” *Addit. Manuf.*, vol. 8, pp. 36–62, 2015.

[13] N. K. Tolochko, Y. V. Khlopkov, S. E. Mozzharov, M. B. Ignatiev, T. Laoui, and V. I. Titov, “Absorptance of powder materials suitable for laser sintering,” *Rapid Prototyp. J.*, vol. 6, no. 3, pp. 155–161, 2000.

[14] U. Österberg and W. Margulis, “Dye laser pumped by Nd:YAG laser pulses frequency doubled in a glass optical fiber,” *Opt. Lett.*, vol. 11, no. 8, p. 516, 1986.

[15] T. Y. Fan and R. L. Byer, “Modeling and CW Operation of a Quasi-Three-Level 946 nm Nd: YAG Laser,” *IEEE J. Quantum Electron.*, vol. 23, no. 5, pp. 605–612, 1987.

[16] N. Shamsaei, A. Yadollahi, L. Bian, and S. M. Thompson, “An overview of Direct Laser Deposition for additive manufacturing; Part II: Mechanical behavior, process parameter optimization and control,” *Addit. Manuf.*, vol. 8, pp. 12–35, 2015.

[17] D. C. Hofmann *et al.*, “Developing gradient metal alloys through radial deposition additive manufacturing,” *Sci. Rep.*, vol. 4, 2014.

[18] D. Hu and R. Kovacevic, “Sensing, modeling and control for laser-based additive manufacturing,” *Int. J. Mach. Tools Manuf.*, vol. 43, no. 1, pp. 51–60, 2003.

[19] G. J. Marshall, W. J. Young, S. M. Thompson, N. Shamsaei, S. R. Daniewicz, and S. Shao, “Understanding the Microstructure Formation of Ti-6Al-4V During Direct Laser Deposition via In-Situ Thermal Monitoring,” *Jom*, vol. 68, no. 3, pp. 778–790, 2016.

[20] A. Strondl, O. Lyckfeldt, H. Brodin, and U. Ackelid, “Characterization and Control of Powder Properties for Additive Manufacturing,” *Jom*, vol. 67, no. 3, pp. 549–554, 2015.

[21] J. Kruth, P. Mercelis, J. Van Vaerenbergh, L. Froyen, and M. Rombouts, “Binding mechanisms in selective laser sintering and selective laser melting,” *Rapid Prototyp. J.*, vol. 11, no. 1, pp. 26–36, 2005.

[22] S. Tripathy, C. Chin, T. London, U. Ankalkhope, and V. Oancea, “Process Modeling and Validation of Powder Bed Metal Additive Manufacturing,” *NAFEMS World Congr. 2017*, no. June, 2017.

[23] A. L. Filho, H. Atkinson, H. Jones, E. De Los Rios, and S. King, “Hot isostatic pressing of metal reinforced metal matrix composites,” *J. Mater. Sci.*, vol. 33, no. 23, pp. 5517–5533, 1998.

[24] A. Yadollahi, N. Shamsaei, S. M. Thompson, and D. W. Seely, "Effects of process time interval and heat treatment on the mechanical and microstructural properties of direct laser deposited 316L stainless steel," *Mater. Sci. Eng. A*, vol. 644, pp. 171–183, 2015.

[25] M. Strantza *et al.*, "Coupled experimental and computational study of residual stresses in additively manufactured Ti-6Al-4V components," *Mater. Lett.*, 2018.

[26] B. Cheng, S. Shrestha, and K. Chou, "Stress and deformation evaluations of scanning strategy effect in selective laser melting," *Addit. Manuf.*, vol. 12, pp. 240–251, 2016.

[27] C. Kamath, B. El-Dasher, G. F. Gallegos, W. E. King, and A. Sisto, "Density of additively-manufactured, 316L SS parts using laser powder-bed fusion at powers up to 400 W," *Int. J. Adv. Manuf. Technol.*, vol. 74, no. 1–4, pp. 65–78, 2014.

[28] A. B. Spierings, N. Herres, and G. Levy, "Influence of the particle size distribution on surface quality and mechanical properties in AM steel parts," *Rapid Prototyp. J.*, vol. 17, no. 3, pp. 195–202, 2011.

[29] M. Krishnan *et al.*, "On the effect of process parameters on properties of AlSi10Mg parts produced by DMLS," *Rapid Prototyp. J.*, vol. 20, no. 6, pp. 449–458, 2014.

[30] D. Buchbinder, H. Schleifenbaum, S. Heidrich, W. Meiners, and J. Bültmann, "High power Selective Laser Melting (HP SLM) of aluminum parts," *Phys. Procedia*, vol. 12, pp. 271–278, 2011.

[31] J. P. Kruth, X. Wang, T. Laoui, and L. Froyen, "Lasers and materials in selective laser sintering," *Assem. Autom.*, vol. 23, no. 4, pp. 357–371, 2003.

[32] Q. Jia and D. Gu, "Selective laser melting additive manufacturing of Inconel 718 superalloy parts: Densification, microstructure and properties," *J. Alloys Compd.*, vol. 585, pp. 713–721, 2014.

[33] S. A. Khairallah, A. T. Anderson, A. Rubenchik, and W. E. King, "Laser powder-bed fusion additive manufacturing: Physics of complex melt flow and formation mechanisms of pores, spatter, and denudation zones," *Acta Mater.*, vol. 108, pp. 36–45, 2016.

[34] B. Zheng, Y. Zhou, J. E. Smugeresky, J. M. Schoenung, and E. J. Lavernia, "Thermal behavior and microstructure evolution during laser deposition with laser-engineered net shaping: Part II. Experimental investigation and discussion," *Metall. Mater. Trans. A Phys. Metall. Mater. Sci.*, vol. 39, no. 9, pp. 2237–2245, 2008.

[35] Y. Li and D. Gu, "Parametric analysis of thermal behavior during selective laser melting additive manufacturing of aluminum alloy powder," *Mater. Des.*, vol. 63, pp. 856–867, 2014.

[36] S. Bontha, N. W. Klingbeil, P. A. Kobryn, and H. L. Fraser, “Thermal process maps for predicting solidification microstructure in laser fabrication of thin-wall structures,” *J. Mater. Process. Technol.*, vol. 178, no. 1–3, pp. 135–142, 2006.

[37] P. . Kobryn and S. . Semiatin, “Microstructure and texture evolution during solidification processing of Ti–6Al–4V,” *J. Mater. Process. Technol.*, vol. 135, no. 2–3, pp. 330–339, 2003.

[38] Q. Wu *et al.*, “Effect of molten pool size on microstructure and tensile properties of wire arc additive manufacturing of Ti-6Al-4V alloy,” *Materials (Basel).*, vol. 10, no. 7, pp. 1–11, 2017.

[39] Y. Wang, C. Kamath, T. Voisin, and Z. Li, “Rapid Prototyping Journal A processing diagram for high-density Ti-6Al-4V by selective laser melting Article information,” 2018.

[40] R. J. Hebert, “Viewpoint: metallurgical aspects of powder bed metal additive manufacturing,” *J. Mater. Sci.*, vol. 51, no. 3, pp. 1165–1175, 2016.

[41] B. A. Bimber, R. F. Hamilton, J. Keist, and T. A. Palmer, “Anisotropic microstructure and superelasticity of additive manufactured NiTi alloy bulk builds using laser directed energy deposition,” *Mater. Sci. Eng. A*, vol. 674, pp. 125–134, 2016.

[42] P. Wei *et al.*, “The AlSi10Mg samples produced by selective laser melting: single track, densification, microstructure and mechanical behavior,” *Appl. Surf. Sci.*, vol. 408, pp. 38–50, 2017.

[43] A. T. Sutton, C. S. Kriewall, M. C. Leu, and J. W. Newkirk, “Powders for Additive Manufacturing Processes: Characterization Techniques and Effects on Part Properties,” *Solid Free. Fabr. Proc.*, pp. 1004–1030, 2016.

[44] L. E. Murr *et al.*, “Characterization of titanium aluminide alloy components fabricated by additive manufacturing using electron beam melting,” *Acta Mater.*, 2010.

[45] J. Dawes, R. Bowerman, and R. Trepleton, “Introduction to the Additive Manufacturing Powder Metallurgy Supply Chain,” *Johnson Matthey Technol. Rev.*, vol. 59, no. 3, pp. 243–256, 2015.

[46] B. Liu, R. Wildman, C. Tuck, I. Ashcroft, and R. Hague, “Investigation the Effect of Particle Size Distribution on Processing Parameters Optimisation in Selective Laser Melting Process,” *Sff*, no. mm, pp. 227–238, 2011.

[47] G. D. Scott, “The density of random close packing of spheres,” *J. Phys. D. Appl. Phys.*, vol. 207, no. 6, pp. 835–866, 2002.

[48] P. K. Samal and J. W. Newkirk, *Powder Metallurgy, Metal Powder Characterization, Bulk Porperties of Powders*. 2015.

[49] T. F. Murphy, "Metallogrpahic testing of powders intended for use in additive manufacutring," *Int. J. Powder Metall.*, vol. 52, no. 1, pp. 25–35, 2016.

[50] A. L. Ryland, "X-Ray diffraction," *J. Chem. Educ.*, vol. 35, no. 2, pp. 80–83, 1958.

[51] T. Starr, K. Rafi, B. Stucker, and C. Scherzer, "Controlling phase composition in selective laser melted stainless steels," *Proc. Solid Free. Fabr. Symp.*, pp. 439–446, 2012.

[52] A. Aversa *et al.*, "New Aluminum Alloys Specifically Designed for Laser Powder Bed Fusion: A Review," *Materials (Basel).*, vol. 12, no. 7, p. 1007, 2019.

[53] M. Simonelli *et al.*, "A Study on the Laser Spatter and the Oxidation Reactions During Selective Laser Melting of 316L Stainless Steel, Al-Si10-Mg, and Ti-6Al-4V," *Metall. Mater. Trans. A Phys. Metall. Mater. Sci.*, vol. 46, no. 9, pp. 3842–3851, 2015.

[54] A. M. Rausch, V. E. Küng, C. Pobel, M. Markl, and C. Körner, "Predictive Simulation of Process Windows for Powder Bed Fusion Additive Manufacturing: Influence of the Powder Bulk Density," *Materials (Basel).*, vol. 10, no. 10, 2017.

[55] M. Tang and P. C. Pistorius, "Oxides, porosity and fatigue performance of AlSi10Mg parts produced by selective laser melting," *Int. J. Fatigue*, vol. 94, pp. 192–201, 2017.

[56] J. Campbell, *Complete Casting Handbook; Metal Casting Processes, Metallurgy, Techniques and Design*, First. Oxford, UK: Elsevier Ltd, 2011.

[57] V. A. Ferraresi, K. M. Figueiredo, and T. H. Ong, "Metal Transfer in the Aluminum Gas Metal Arc Welding," vol. XXV, no. 3.

[58] A. M. Beese and B. E. Carroll, "Review of Mechanical Properties of Ti-6Al-4V Made by Laser-Based Additive Manufacturing Using Powder Feedstock," *Jom*, vol. 68, no. 3, pp. 724–734, 2016.

[59] C. Qiu, C. Panwisawas, M. Ward, H. C. Basoalto, J. W. Brooks, and M. M. Attallah, "On the role of melt flow into the surface structure and porosity development during selective laser melting," *Acta Mater.*, vol. 96, pp. 72–79, 2015.

[60] M. N. Ahsan, A. J. Pinkerton, R. J. Moat, and J. Shackleton, "A comparative study of laser direct metal deposition characteristics using gas and plasma-atomized Ti-6Al-4V powders," *Mater. Sci. Eng. A*, vol. 528, no. 25–26, pp. 7648–7657, 2011.

[61] L. Wang, P. Pratt, S. Felicelli, H. Kadiri, and P. Wang, "Experimental Analysis of Porosity Formation in Laser-Assisted Powder Deposition Process," *TMS (The Miner. Met. Mater. Soc.*, vol. 1, no. January 2014, pp. 389–396, 2009.

[62] J. E. Hatch, *Properties and Physical Metallurgy*, 1st ed. 1984.

[63] F. C. Frary, "The Electrolytic Refining of Aluminum," *Trans. Am. Electrochem. Soc.*, vol. 47, pp. 275–286, 1922.

[64] X. Guo, G. Cheng, and W. Liu, "Report of the Workshop Predictive Theoretical, Computational, and Experimental Approaches for Additive Manufacturing (WAM 2016)," 2016.

[65] A. M. Si, K. C. H. Kumar, N. Chakraborti, H. Lukas, O. Bodak, and L. Rokhlin, *Aluminium – Magnesium – Silicon*. .

[66] S. P. Ringer and K. Hono, "Microstructural Evolution and Age Hardening in Aluminium Alloys," *Mater. Charact.*, vol. 44, no. 1–2, pp. 101–131, 2002.

[67] Q. G. Wang, "Solidification and precipitation behaviour of Al-Si-Mg casting alloys," *J. Mater. Sci.*, vol. 6, no. 36, pp. 739–750, 2001.

[68] X. Liu, C. Zhao, X. Zhou, Z. Shen, and W. Liu, "Microstructure of selective laser melted AlSi10Mg alloy," *Mater. Des.*, vol. 168, p. 107677, 2019.

[69] N. T. Aboulkhair, N. M. Everitt, I. Ashcroft, and C. Tuck, "Reducing porosity in AlSi10Mg parts processed by selective laser melting," *Addit. Manuf.*, vol. 1, pp. 77–86, 2014.

[70] E. Brandl, U. Heckenberger, V. Holzinger, and D. Buchbinder, "Additive manufactured AlSi10Mg samples using Selective Laser Melting (SLM): Microstructure, high cycle fatigue, and fracture behavior," *Mater. Des.*, vol. 34, pp. 159–169, 2012.

[71] X. Yu and L. Wang, "T6 heat-treated AlSi10Mg alloys additive-manufactured by selective laser melting," *Procedia Manuf.*, vol. 15, pp. 1701–1707, 2018.

[72] E. Louvis, P. Fox, and C. J. Sutcliffe, "Selective laser melting of aluminium components," *J. Mater. Process. Technol.*, vol. 211, no. 2, pp. 275–284, 2011.

[73] Y. P. Lei, H. Murakawa, Y. W. Shi, and X. Y. Li, "Numerical analysis of the competitive influence of Marangoni flow and evaporation on heat surface temperature and molten pool shape in laser surface remelting," *Comput. Mater. Sci.*, vol. 21, no. 3, pp. 276–290, 2001.

[74] "The Influence of a Process Interruption on Tensile Properties of AlSi10Mg Samples Produced by Selective Laser Melting," 2012.

[75] Renishaw, “AM 400 additive manufacturing system Flexible metal additive manufacturing (AM),” 2019.

[76] A. S. Ginzburg, A. A. Vinogradova, E. I. Fedorova, E. V. Nikitich, and A. V. Karpov, “Content of oxygen in the atmosphere over large cities and respiratory problems,” *Izv. Atmos. Ocean. Phys.*, vol. 50, no. 8, pp. 782–792, 2014.

[77] A. Thompson, I. Maskery, and R. K. Leach, “X-ray computed tomography for additive manufacturing: A review,” *Meas. Sci. Technol.*, vol. 27, no. 7, 2016.

[78] U. Tradowsky, J. White, R. M. Ward, N. Read, W. Reimers, and M. M. Attallah, “Selective laser melting of AlSi10Mg: Influence of post-processing on the microstructural and tensile properties development,” *Mater. Des.*, vol. 105, pp. 212–222, 2016.

[79] “myVGL 3.2 Reference Manual,” 2019.

[80] L. N. Carter, C. Martin, P. J. Withers, and M. M. Attallah, “The influence of the laser scan strategy on grain structure and cracking behaviour in SLM powder-bed fabricated nickel superalloy,” *J. Alloys Compd.*, vol. 615, pp. 338–347, 2014.

[81] L. E. Murr, “Metallurgy of additive manufacturing: Examples from electron beam melting,” *Addit. Manuf.*, vol. 5, pp. 40–53, 2015.

[82] M. Fousová, D. Dvorský, A. Michalcová, and D. Vojtěch, “Changes in the microstructure and mechanical properties of additively manufactured AlSi10Mg alloy after exposure to elevated temperatures,” *Mater. Charact.*, vol. 137, no. November 2017, pp. 119–126, 2018.

[83] R. Anderhalt and L. Swenson, “Applications for Automated Particle Analysis,” no. September, 2006.

[84] S. I. Wright, “3D Orientation Microscopy,” pp. 40–41, 2007.

[85] G. M. Dieter, *Mechanical Metallurgy*, Third. McGraw-Hill Inc., 1986.

[86] Z. Wang, T. A. Palmer, and A. M. Beese, “Effect of processing parameters on microstructure and tensile properties of austenitic stainless steel 304L made by directed energy deposition additive manufacturing,” *Acta Mater.*, vol. 110, pp. 226–235, 2016.

[87] I. Yadroitsev, P. Krakhmalev, I. Yadroitsava, S. Johansson, and I. Smurov, “Energy input effect on morphology and microstructure of selective laser melting single track from metallic powder,” *J. Mater. Process. Technol.*, vol. 213, no. 4, pp. 606–613, 2013.

[88] R. F. Smith and G. E. Sandland, “An Accurate Method of Determining the Hardness of Metals with Particular Reference to those of a High Degree of Hardness,” in *Proceedings of the institution of Mechanical Engineers*, 1922, pp. 623–641.

[89] A. Yadollahi and N. Shamsaei, “Additive manufacturing of fatigue resistant materials: Challenges and opportunities,” *Int. J. Fatigue*, vol. 98, pp. 14–31, 2017.

[90] A. International, “E8/E8M-16a Standard Test Methods for Tension Testing of Metallic Materials.” 2016.

[91] N. Coniglio and C. E. Cross, “Mechanisms for solidification crack initiation and growth in aluminum welding,” *Metall. Mater. Trans. A Phys. Metall. Mater. Sci.*, 2009.

APPENDIX A

SAMPLE PREPARATION STEPS

Table A.1 Struers polishing steps

Step #	Grit	RPM	Force (N)	Time (minutes)	Water
1	Gekko Disk, 320 silicon carbide	300	20	1	Yes
2	MD Largo DiaPro Allegro/Largo (9µ)	150	20	4	Yes
3	MD Mol Cloth DiaPro MD Mol (3µ)	150	20	5	No
4	MD Chem Cloth, 50ml OP-S & 25ml water	150	15	2	Yes, to side of cloth

All polishing is contra rotation, gently rinse samples with soapy cotton balls and water.

Table A.2 Keller's reagent recipe

Chemical	Amount (ml)
Water	95
HNO_3	2.5
HCl	1.5
HF	1.5

Add acid to water for safe dilution. Always wear: double nitrile glove, goggles, full face mask, long sleeves, and apron.

APPENDIX B

ADDITIONAL ANALYSIS IMAGES AND DATA

B.1 Optical Microscope images

Optical micrographs were taken at varying magnifications. The magnification is denoted in the figure description.

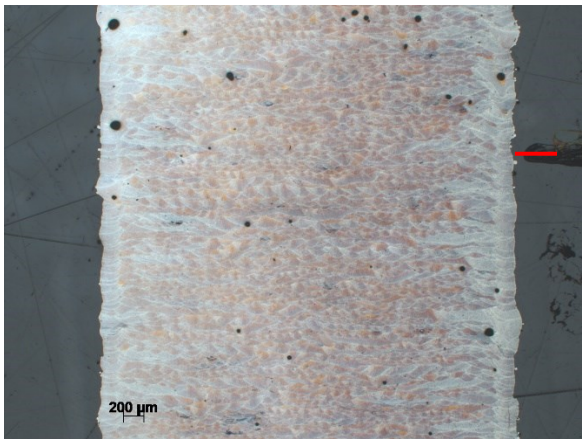

Figure B.1 5 minute dog bone

5 minute dog bone at 2.5x. Interruption location marked by red line.

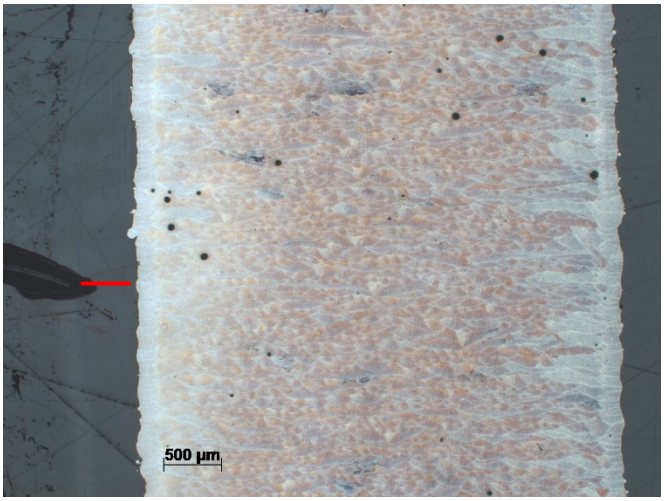

Figure B.2 5 minute air dog bone

5 minute dog bone at 2.5x. Interruption location marked by red line.

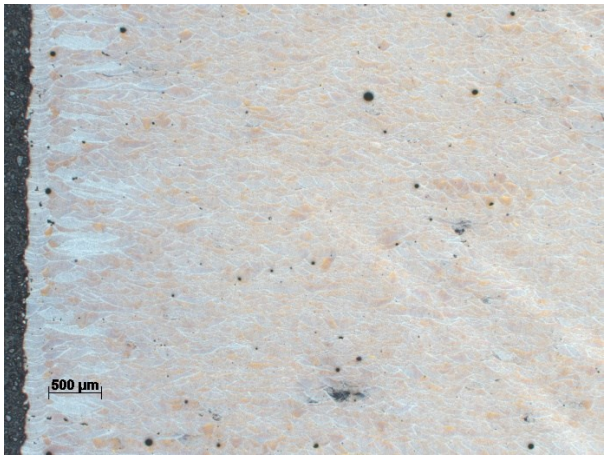

Figure B.3 Control cylinder

Control cylinder left side at 2.5x.

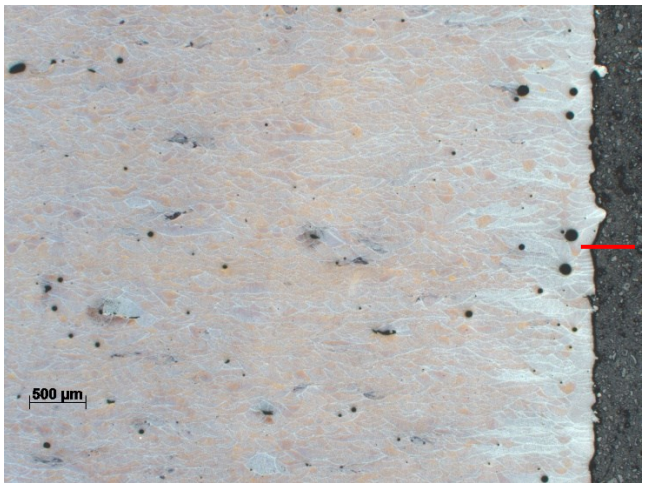

Figure B.4 Complete cool cylinder

Complete cool cylinder left side at 2.5x. Interruption plane marked by red line.

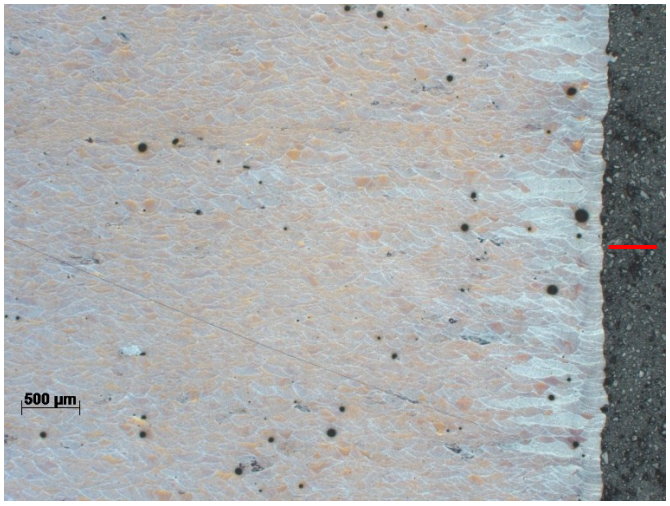

Figure B.5 Complete cool air cylinder

Complete cool air cylinder left side at 2.5x. Interruption plane marked by red line.

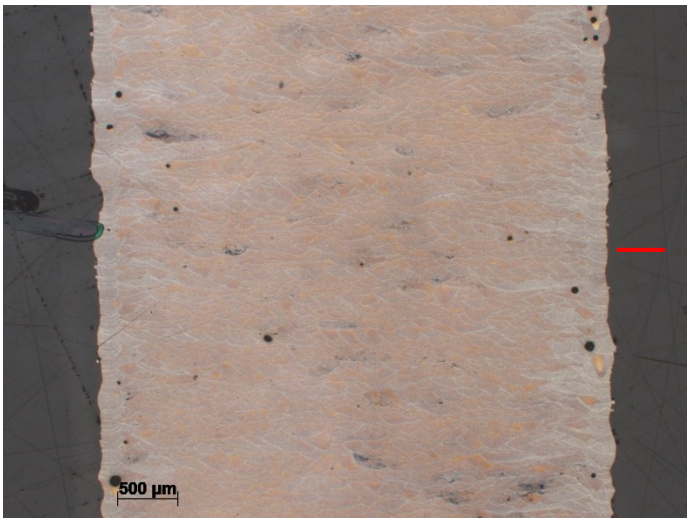

Figure B.6 24 hour air dog bone

24 hour air dog bone at 2.5x. Interruption plane marked by red line.

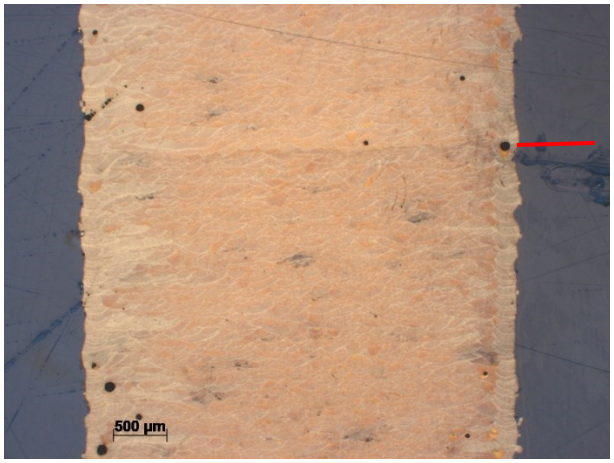

Figure B.7 24 hour cylinder

24 hour cylinder at 2.5x. Interruption plane marked by red line.

B.2 EDS images

All EDS images are arranged in the same layout. The elements are given by the box in the lower left hand corner.

Table B.1 Elemental wt% of EDS map in Figure B.8

Element	Wt%	At%
O	00.23	00.39
Mg	00.75	00.84
Al	91.48	91.53
Si	07.54	07.25
Matrix	Correction	ZAF

Elemental wt% of EDS map in Figure B.8

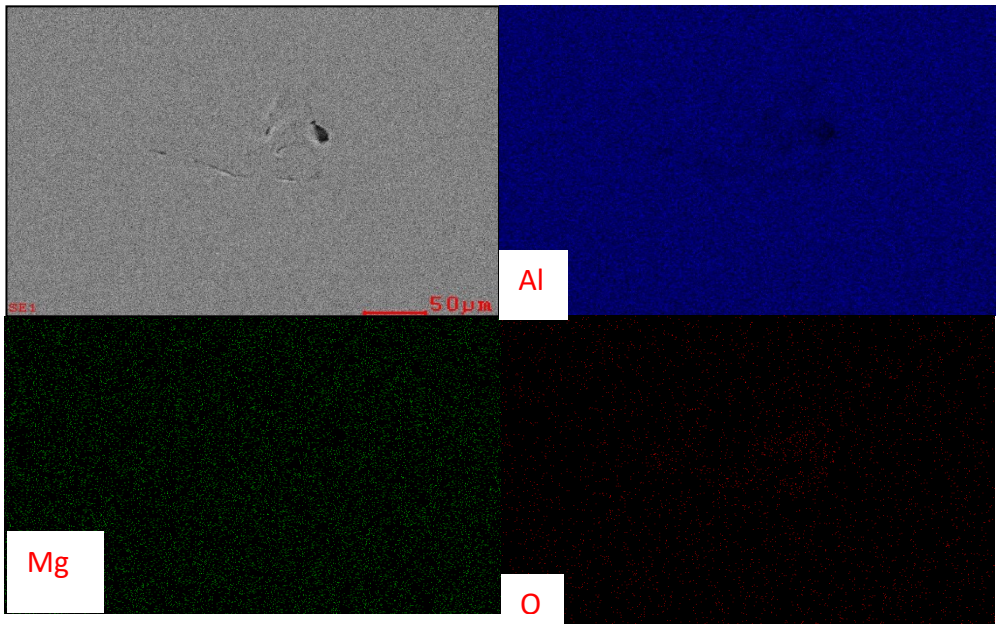

Figure B.8 EDS map of 24 hour air cylinder.

EDS map of 24 hour air cylinder.

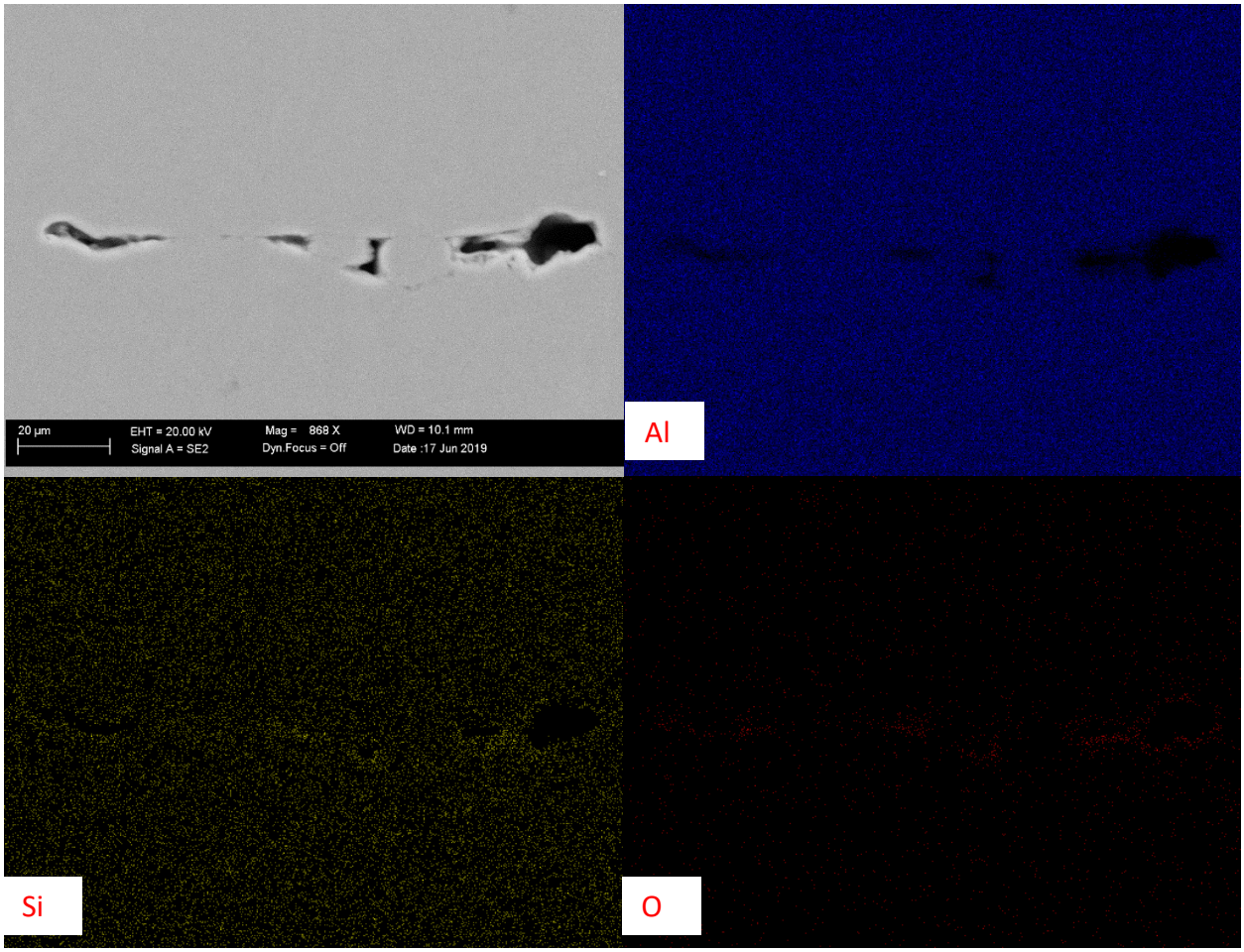

Figure B.9 EDS map of cool cylinder air inclusion.

EDS map of cool cylinder air inclusion.

Table B.2 Elemental wt% of 24 hour dog bone EDS map in Figure B.10

Element	Wt%	At%
O	04.84	07.93
Mg	00.47	00.50
Al	83.69	81.29
Si	11.00	10.27
Matrix	Correction	ZAF

Elemental wt% of 24 hour dog bone EDS map in Figure B.10

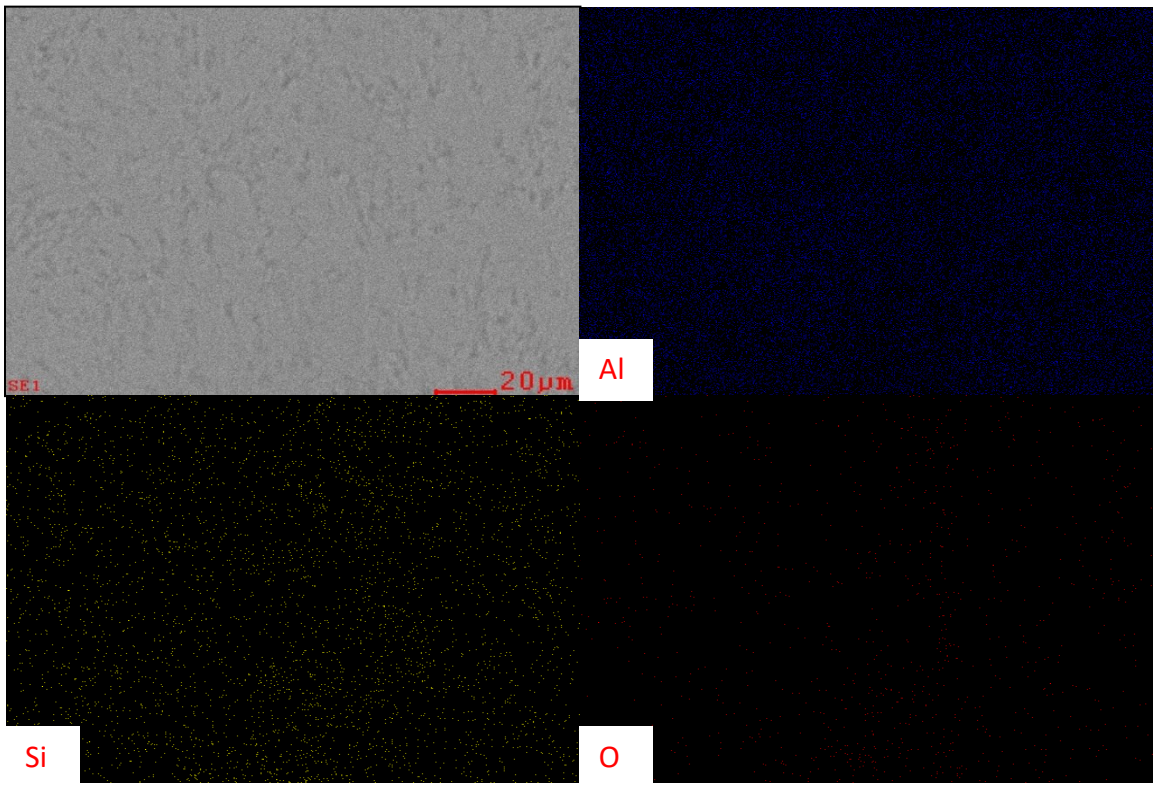

Figure B.10 EDS map of 24 hour dog bone material

EDS map of 24 hour dog bone bulk material.

B.3 Stress strain plots

All stress strain plots are grouped according to specimen number for each experiment. All stress strain plots are engineering stress strain curves. All experiment groups have consistent coloring between curves.

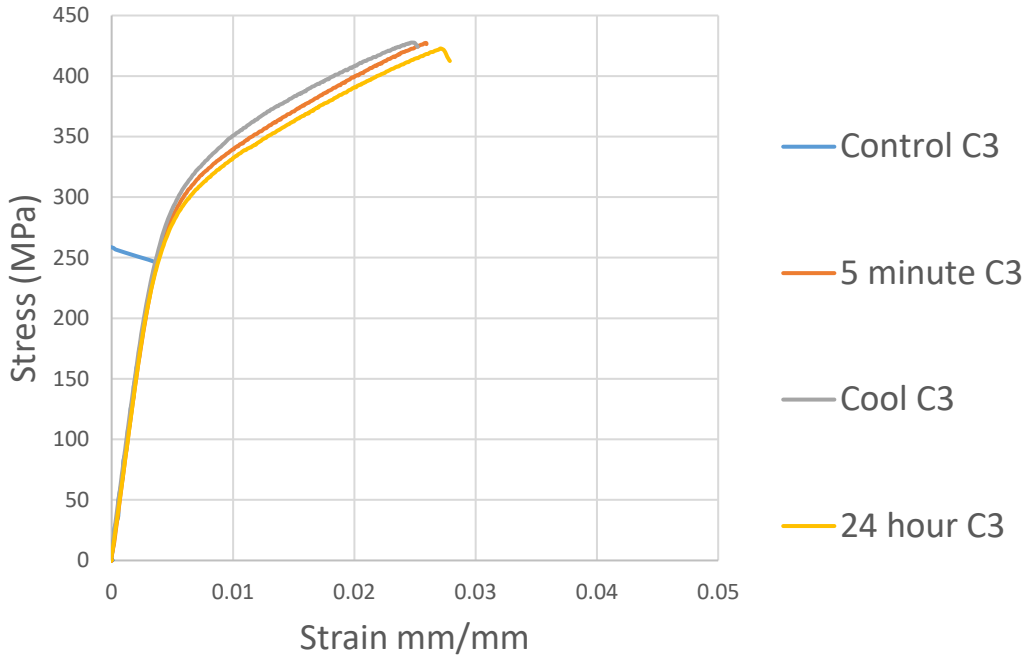

Figure B.11 Engineering stress-strain curve for cylinder #3 specimens.

Engineering stress-strain curve for cylinder #3 specimens. The control cylinder #3 is plotted even though the curve is bad. The wrong clips for the extensometer were used causing the extensometer to slip on the sample.

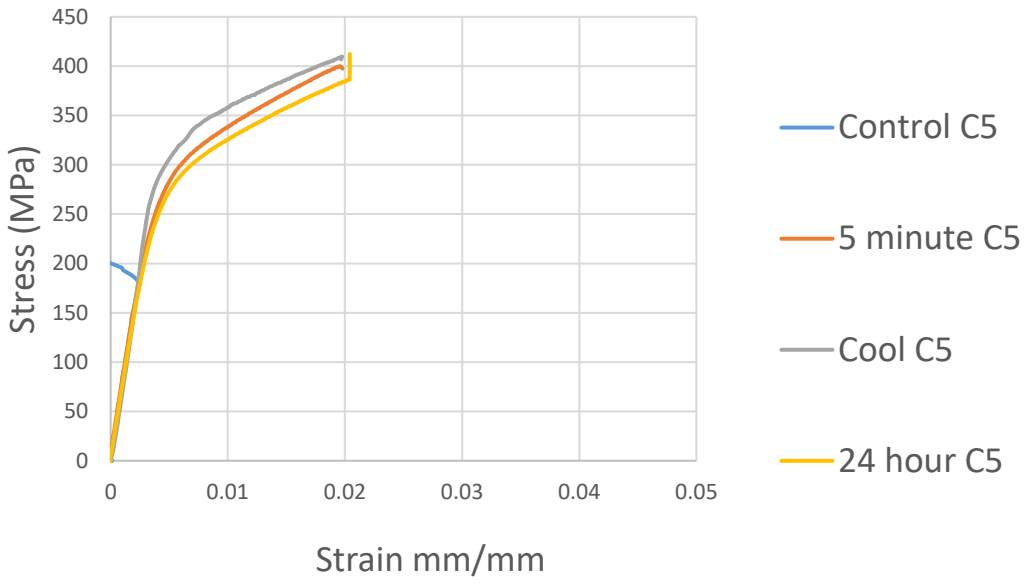

Figure B.12 Engineering stress-strain curve for cylinder #5 specimens.

Engineering stress-strain curve for cylinder #5 specimens. The control cylinder #5 is plotted even though the curve is bad. The wrong clips for the extensometer were used causing the extensometer to slip on the sample.

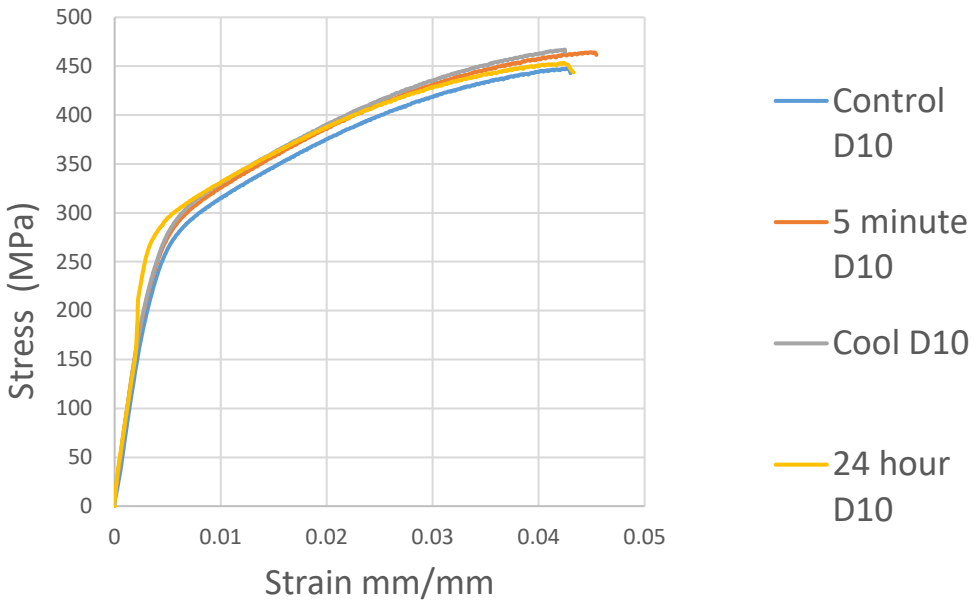

Figure B.13 Engineering stress strain curves for dog bone #10 specimens.

Engineering stress strain curves for dog bone #10 specimens.

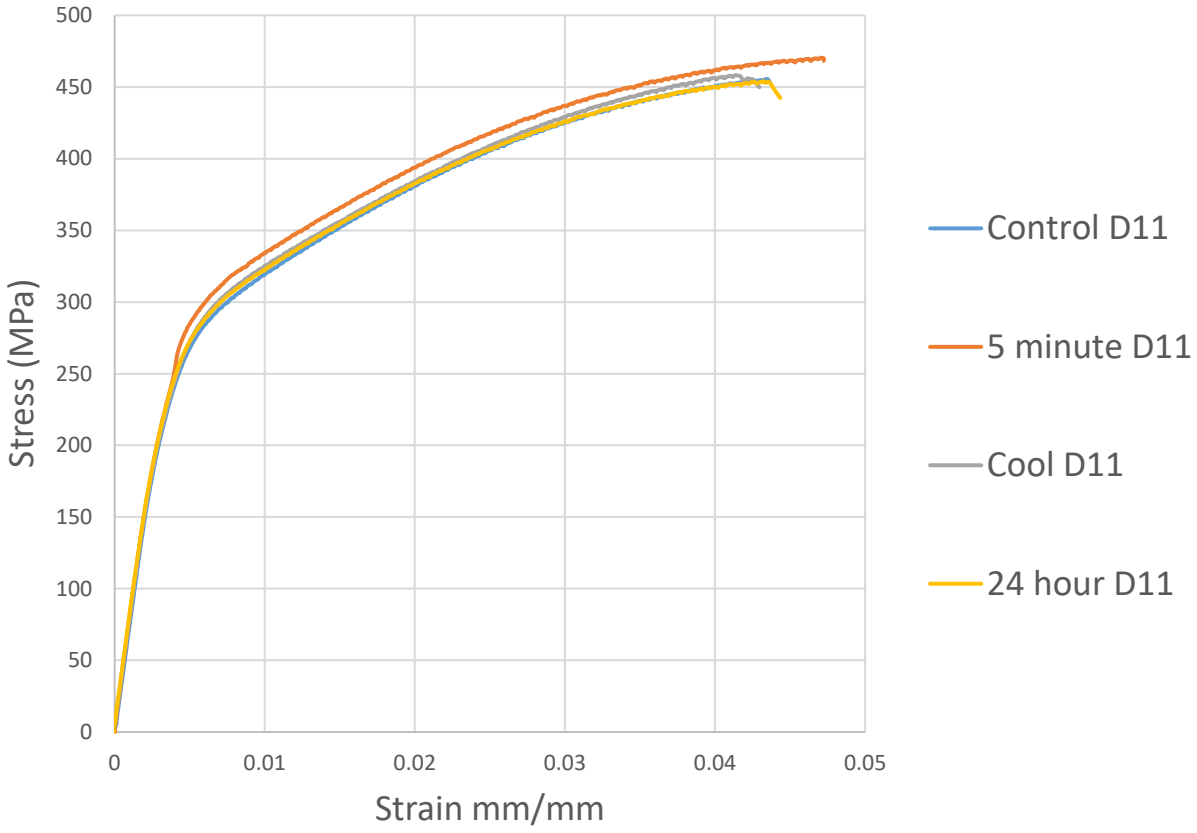

Figure B.14 Engineering stress strain curves for dog bone #11 specimens.

Engineering stress strain curves for dog bone #11 specimens.

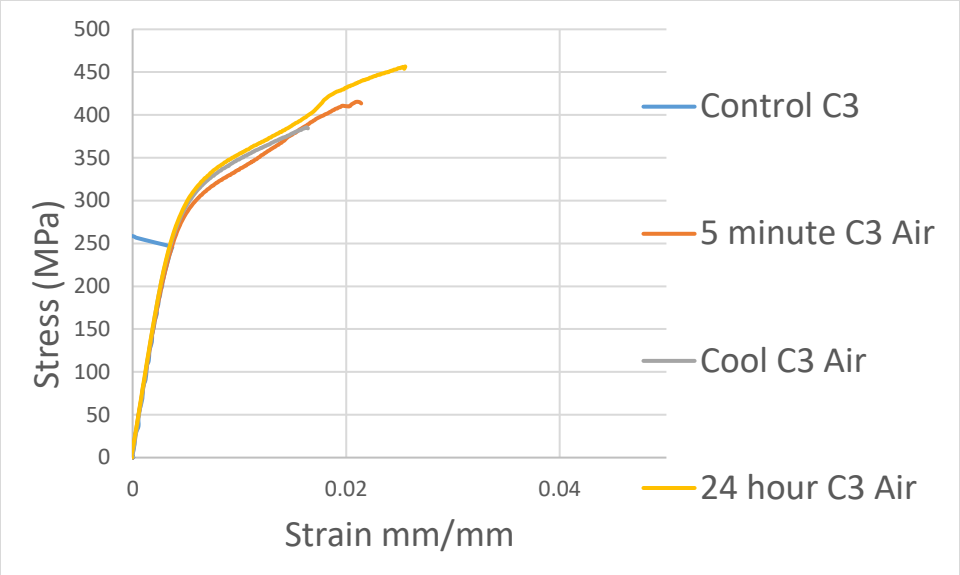

Figure B.15 Engineering stress strain curves for cylinder air #3 specimens.

Engineering stress strain curves for cylinder #3 specimens. The control cylinder #3 is plotted even though the curve is bad. The wrong clips for the extensometer were used causing the extensometer to slip on the sample.

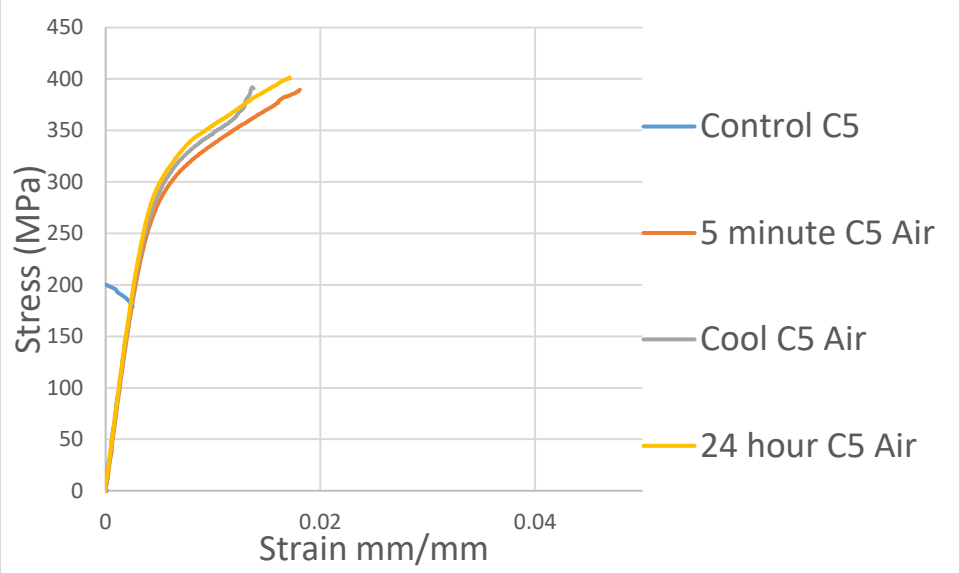

Figure B.16 Engineering stress strain curves for cylinder air #5 specimens.

Engineering stress strain curves for cylinder air #5 specimens. The control cylinder #5 is plotted even though the curve is bad. The wrong clips for the extensometer were used causing the extensometer to slip on the sample.

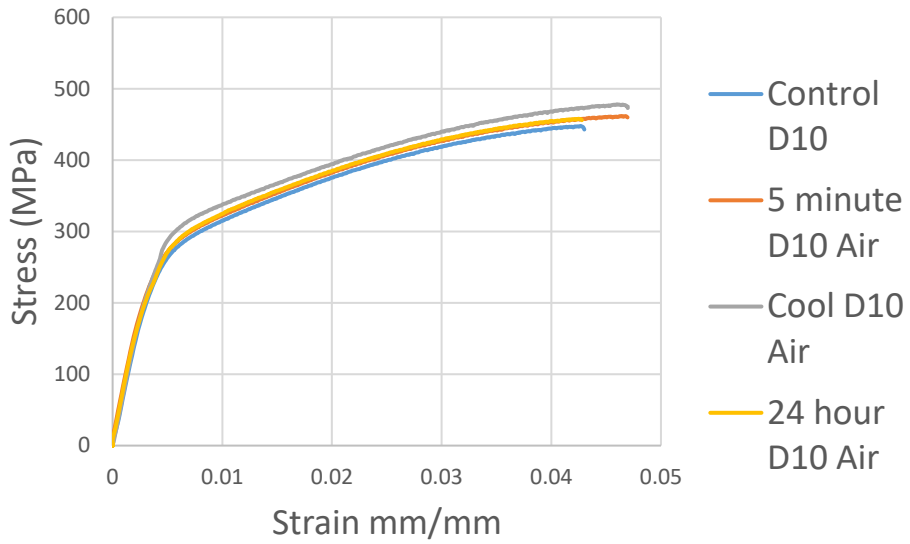

Figure B.17 Engineering stress strain curves for dog bone air #10 specimens.

Engineering stress strain curves for dog bone air #10 specimens.

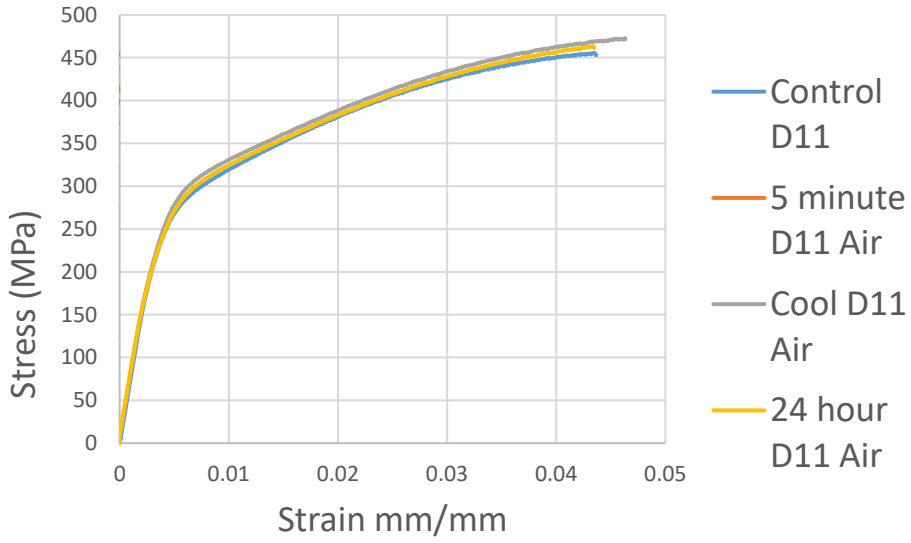

Figure B.18 Engineering stress strain curves for dog bone air #11 specimens.

Engineering stress strain curves for dog bone air #11 specimens. The 5 minute dog bone #11 curve is plotted but not visible as the test was run without an extensometer. The data alternates along the y-axis.

B.4 Macroscopic fracture images

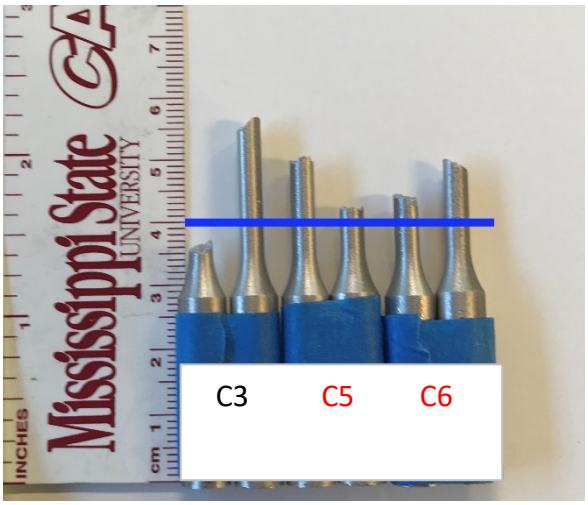

Figure B.19 Control machined specimens.

Control machined specimens with blue line indicating interruption location. All specimens are arranged with bottom portion on right side. Red text indicates specimens chosen for fractography.

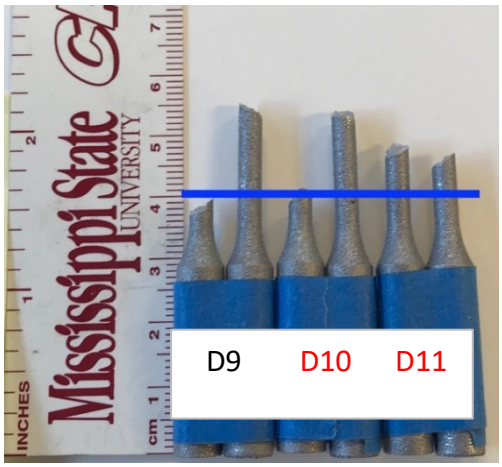

Figure B.20 Control dog bone specimens

Control dog bone specimens with blue line indicating interruption location. All specimens are arranged with bottom portion on right side. Red text indicates specimens chosen for fractography.

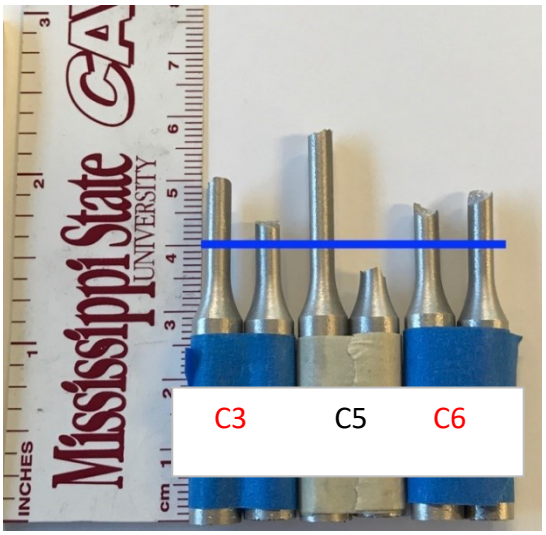

Figure B.21 Cool no air machined specimens

Cool no air machined specimens with blue line indicating interruption location. All specimens are arranged with bottom portion on right side. Red text indicates specimens chosen for fractography.

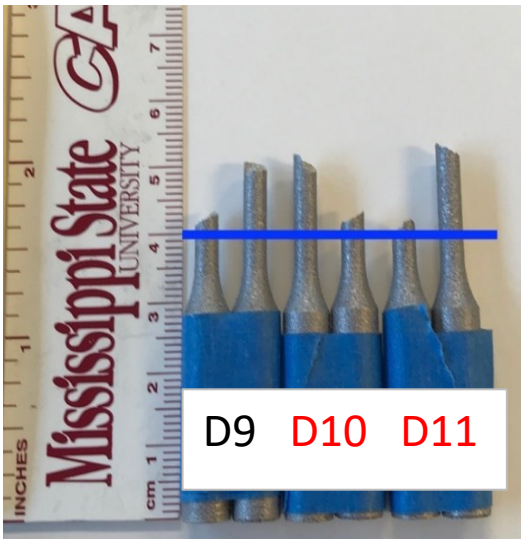

Figure B.22 Cool no air dog bone specimens

Cool no air dogbone specimens with blue line indicating interruption location. All specimens are arranged with bottom portion on right side. Red text indicates specimens chosen for fractography.

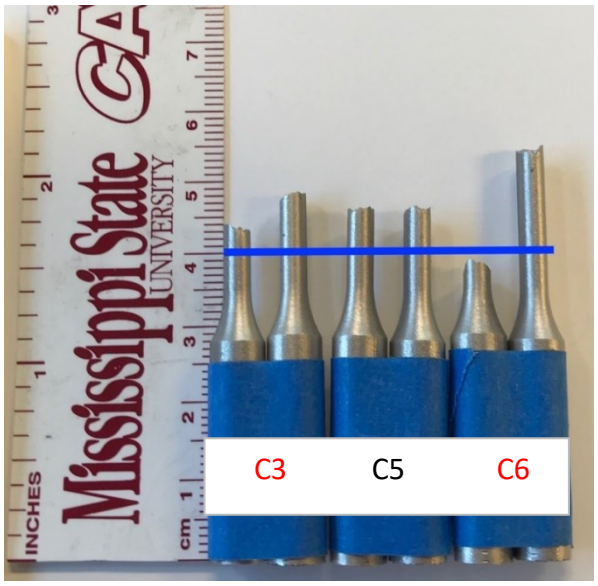

Figure B.23 Cool air machined specimens

Cool air machined specimens with blue line indicating interruption location. All specimens are arranged with bottom portion on right side. Red text indicates specimens chosen for fractography.

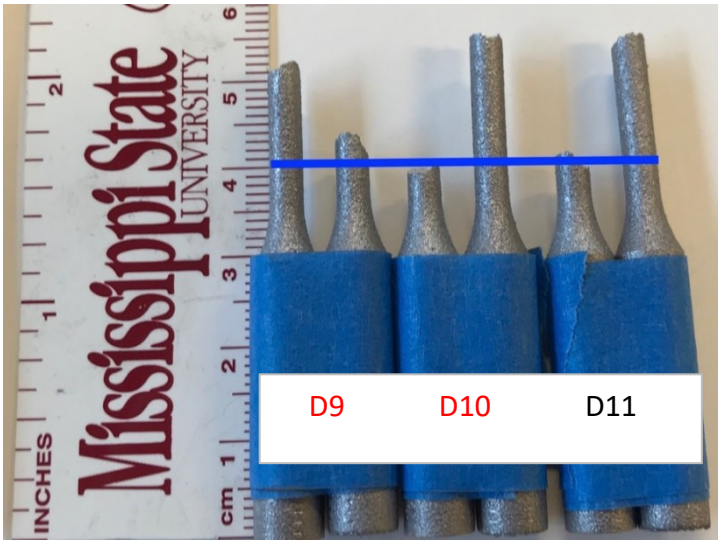

Figure B.24 Cool air dog bone specimens

Cool air dogbone specimens with blue line indicating interruption location. All specimens are arranged with bottom portion on right side. Red text indicates specimens chosen for fractography.

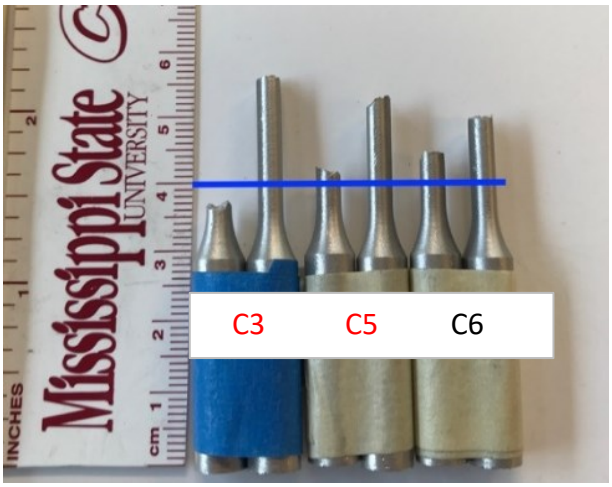

Figure B.25 5min no air machined specimens

5min no air machined specimens with blue line indicating interruption location. All specimens are arranged with bottom portion on right side. Red text indicates specimens chosen for fractography.

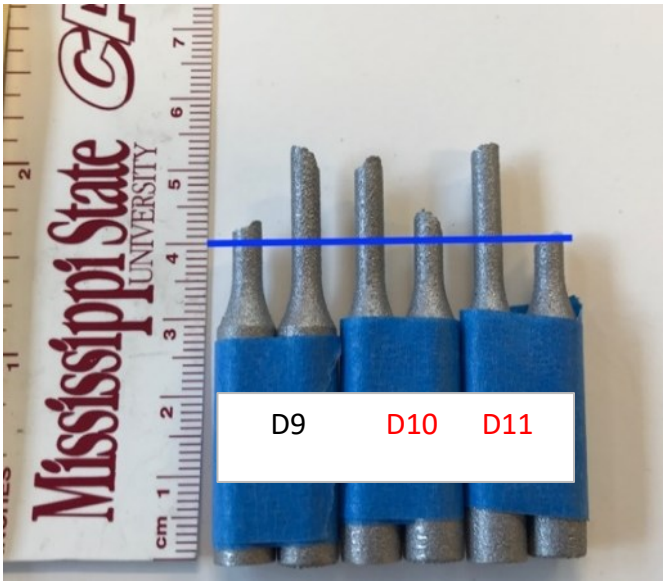

Figure B.26 5min no air dog bone specimens

5min no air dog bone specimens with blue line indicating interruption location. All specimens are arranged with bottom portion on right side. Red text indicates specimens chosen for fractography.

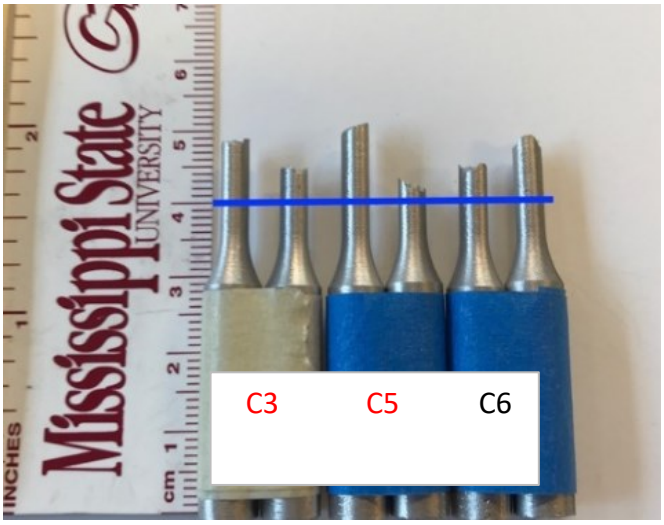

Figure B.27 5min air machined specimens

5min air machined specimens with blue line indicating interruption location. All specimens are arranged with bottom portion on right side. Red text indicates specimens chosen for fractography.

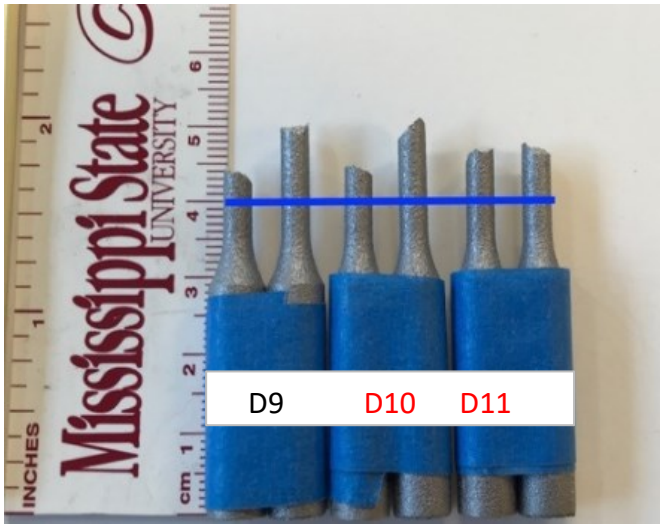

Figure B.28 5min air dog bone specimens

5min air dog bone specimens with blue line indicating interruption location. All specimens are arranged with bottom portion on right side. Red text indicates specimens chosen for fractography.

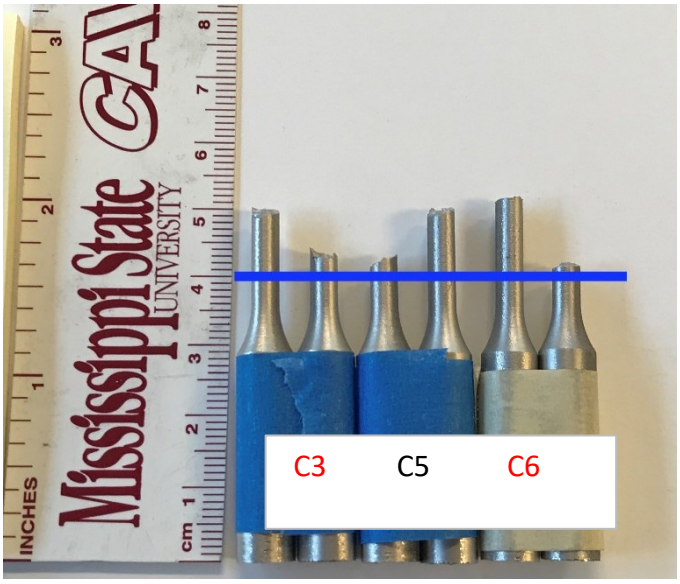

Figure B.29 24hr no air machined specimens

24hr no air machined specimens with blue line indicating interruption location. All specimens are arranged with bottom portion on right side. Red text indicates specimens chosen for fractography.

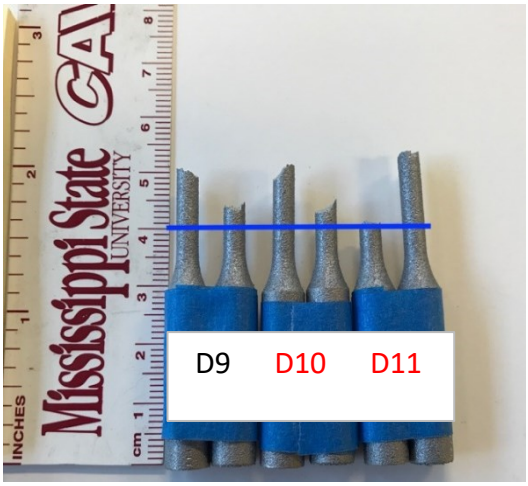

Figure B.30 24hr no air dog bone specimens

24hr no air dog bone specimens with blue line indicating interruption location. All specimens are arranged with bottom portion on right side. Red text indicates specimens chosen for fractography.

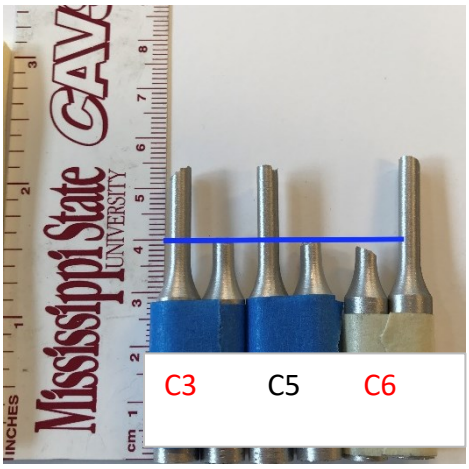

Figure B.31 24hr air machined specimens

24hr air machined specimens with blue line indicating interruption location. All specimens are arranged with bottom portion on right side. Red circle indicates specimens chosen for fractography.

Figure B.32 24hr air dog bone specimens

24hr air machined specimens with blue line indicating interruption location. All specimens are arranged with bottom portion on right side. Red circle indicates specimens chosen for fractography.

B.5 Microscopic fracture images

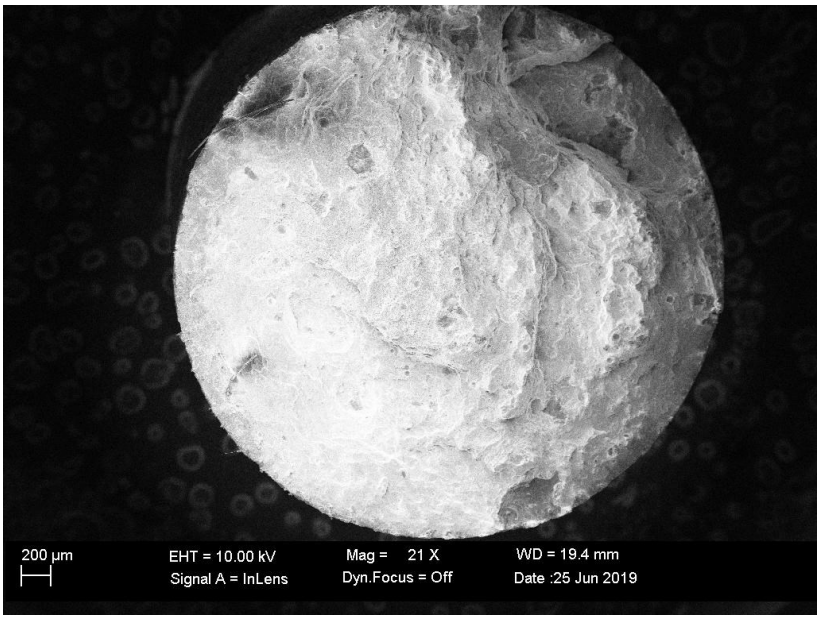

Figure B.33 Control cylinder #3 specimen

Control cylinder #5 specimen. Fracture surface is bottom half of specimen.

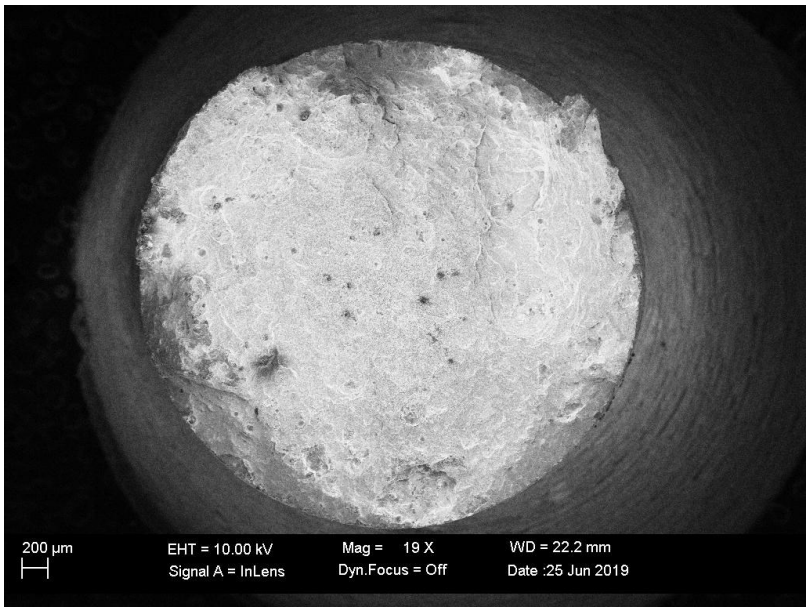

Figure B.34 Control cylinder #5 specimen

Control cylinder #3 specimen. Fracture surface is bottom half of specimen.

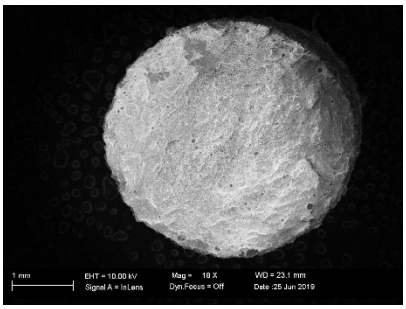

Figure B.35 Control dog bone #10 specimen

Control dog bone #10 specimen. Fracture surface is bottom half of specimen.

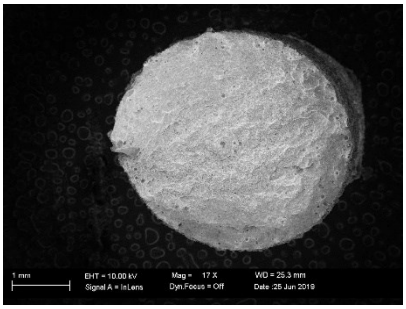

Figure B.36 Control dog bone #11 specimen

Control dog bone #11 specimen. Fracture surface is bottom half of specimen.

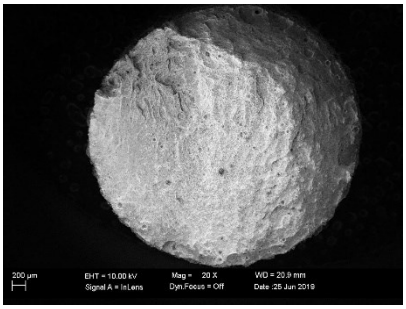

Figure B.37 5 minute no air cylinder #3 specimen

5 minute no air cylinder #3 specimen. Fracture surface is bottom half of specimen.

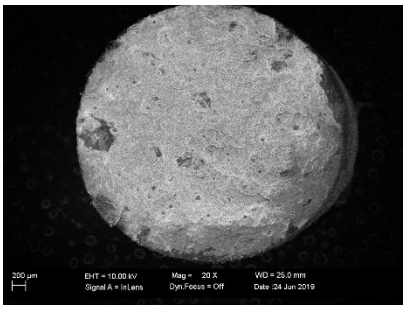

Figure B.38 5 minute no air cylinder #5 specimen

5 minute no air cylinder #5 specimen. Fracture surface is bottom half of specimen.

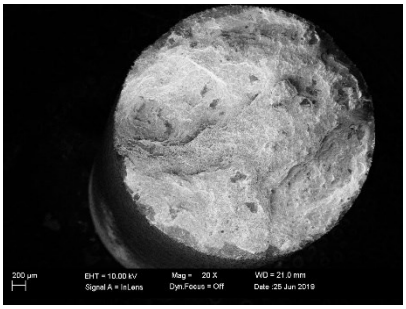

Figure B.39 5 minute no air dogbone #9 specimen.

5 minute no air dogbone #9 specimen. Fracture surface is bottom half of specimen.

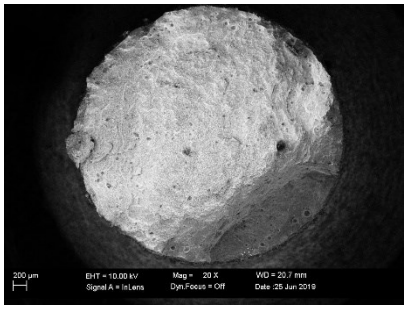

Figure B.40 5 minute no air dogbone #10 specimen

5 minute no air dogbone #10 specimen. Fracture surface is bottom half of specimen.

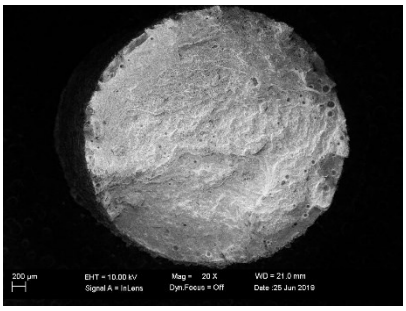

Figure B.41 5 minute air cylinder #3 specimen

5 minute air cylinder #3 specimen. Fracture surface is bottom half of specimen.

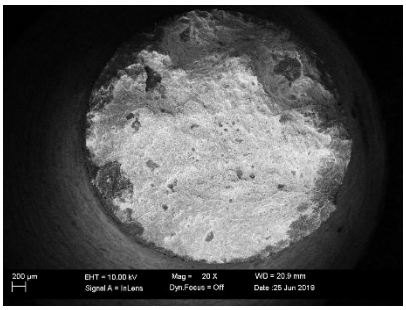

Figure B.42 5 minute air cylinder #5 specimen

5 minute air cylinder #5 specimen. Fracture surface is bottom half of specimen.

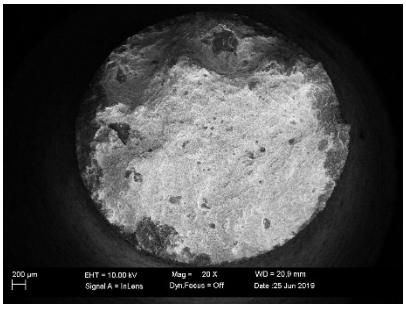

Figure B.43 5 minute air dogbone #9 specimen

5 minute air dogbone #9 specimen. Fracture surface is bottom half of specimen.

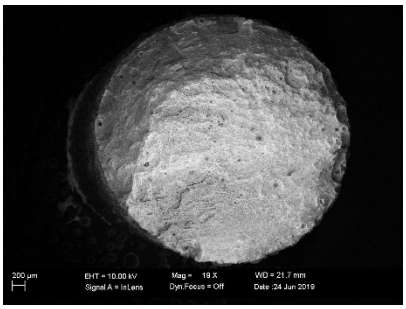

Figure B.44 5 minute air dogbone #10 specimen

5 minute air dogbone #10 specimen. Fracture surface is bottom half of specimen.

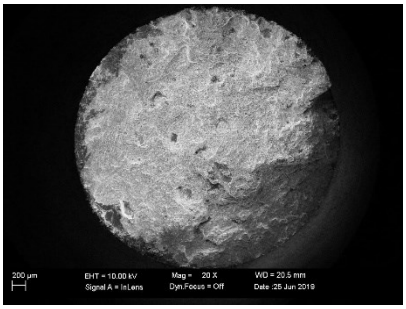

Figure B.45 Cool no air cylinder #3 specimen

Cool no air cylinder #3 specimen. Fracture surface is bottom half of specimen.

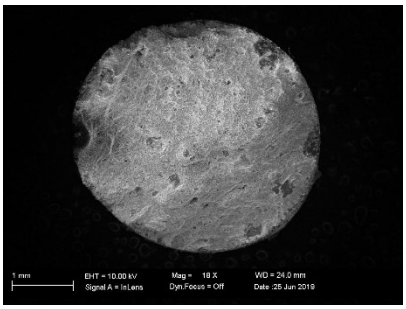

Figure B.46 Cool no air cylinder #6 specimen

Cool no air cylinder #6 specimen. Fracture surface is bottom half of specimen.

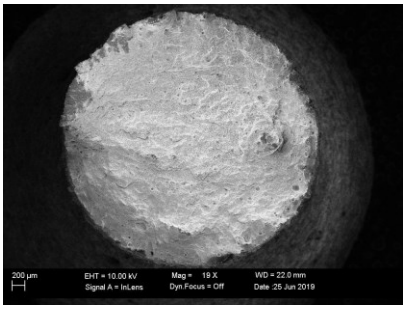

Figure B.47 Cool no air dog bone #10 specimen

Cool no air dog bone #10 specimen. Fracture surface is bottom half of specimen.

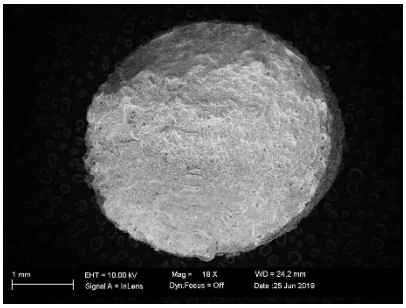

Figure B.48 Cool no air dog bone #11 specimen.

Cool no air dog bone #11 specimen. Fracture surface is bottom half of specimen

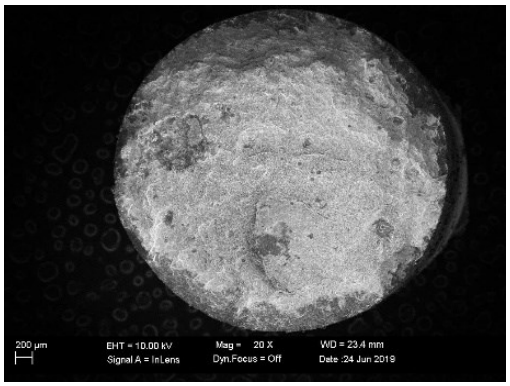

Figure B.49 Cool air cylinder #3 specimen

Cool air cylinder #3 specimen. Fracture surface is bottom half of specimen.

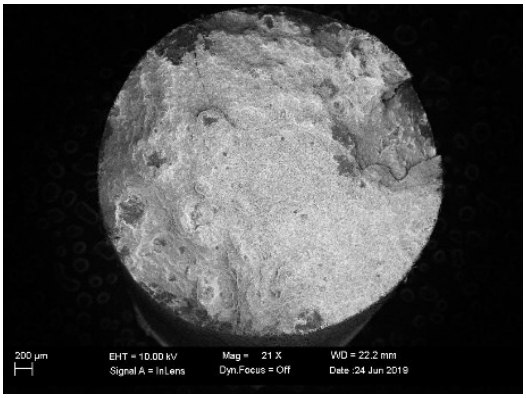

Figure B.50 Cool air cylinder #6 specimen

Cool air cylinder #6 specimen. Fracture surface is bottom half of specimen.

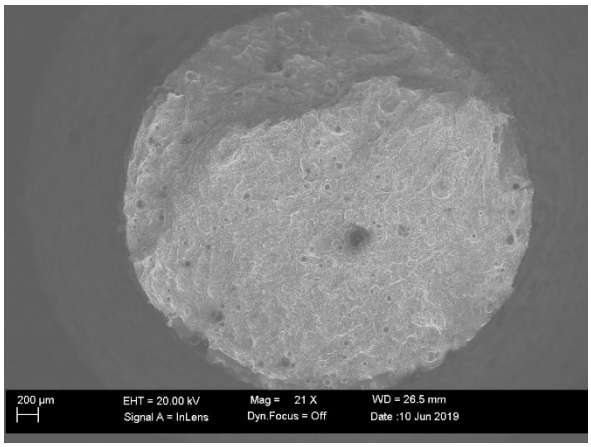

Figure B.51 Cool air dogbone #9 specimen

Cool air dogbone #9 specimen. Fracture surface is bottom half of specimen.

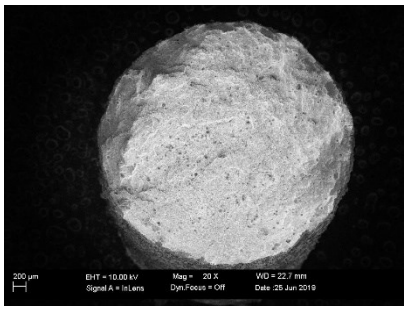

Figure B.52 Cool air dogbone #10 specimen

Cool air dogbone #10 specimen. Fracture surface is bottom half of specimen

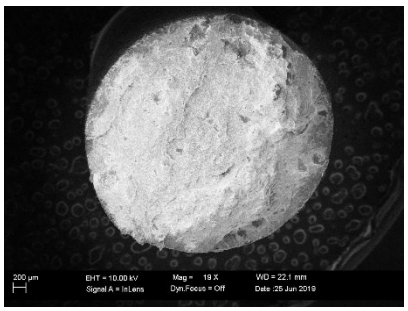

Figure B.53 24hr no air cylinder #5 specimen

24hr no air cylinder #5 specimen. Fracture surface is bottom half of specimen.

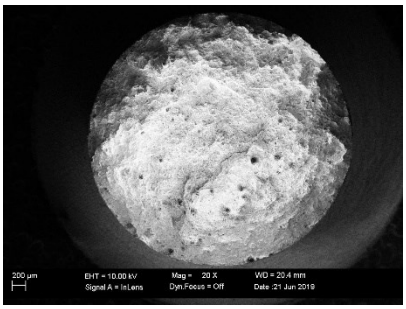

Figure B.54 24hr no air cylinder #6 specimen

24hr no air cylinder #6 specimen. Fracture surface is bottom half of specimen.

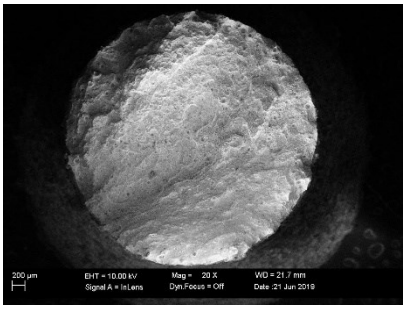

Figure B.55 24hr no air dog bone #10 specimen

24hr no air dog bone #10 specimen. Fracture surface is bottom half of specimen.

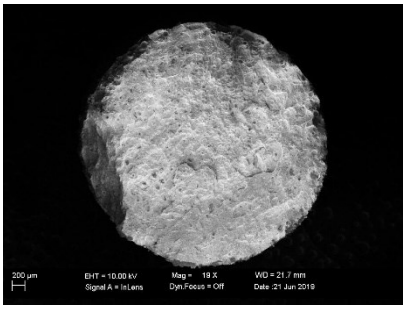

Figure B.56 24hr no air dog bone #11 specimen

24hr no air dog bone #11 specimen. Fracture surface is bottom half of specimen.

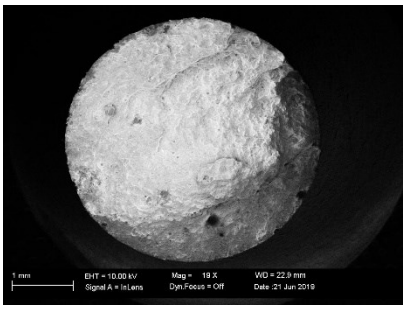

Figure B.57 24hr air cylinder #3 specimen

24hr air cylinder #3 specimen. Fracture surface is bottom half of specimen.

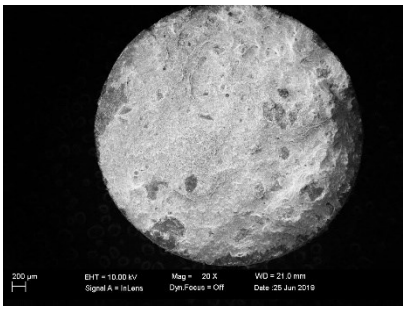

Figure B.58 24hr air cylinder #6 specimen

24hr air cylinder #6 specimen. Fracture surface is bottom half of specimen.

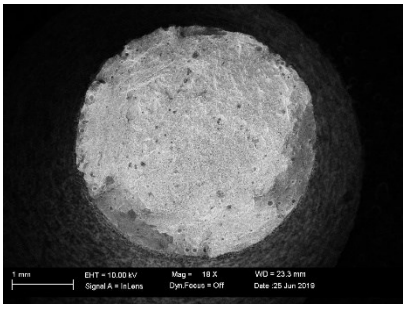

Figure B.59 24hr air dog bone #9 specimen

24hr air dog bone #9 specimen. Fracture surface is bottom half of specimen.

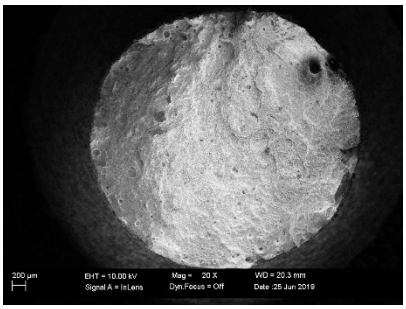

Figure B.60 24hr air dog bone #10 specimen

24hr air dog bone #10 specimen. Fracture surface is bottom half of specimen.